

**Dependence of continental severe convective
instability on climatological environmental
conditions**

by

John Vincent Agard

S.B. Earth, Atmospheric and Planetary Sciences and Physics,
Massachusetts Institute of Technology (2011)

Submitted to the Department of Earth, Atmospheric and Planetary
Sciences

in partial fulfillment of the requirements for the degree of

Doctor of Philosophy in Atmospheric Science

at the

MASSACHUSETTS INSTITUTE OF TECHNOLOGY

September 2017

© Massachusetts Institute of Technology 2017. All rights reserved.

Author **Signature redacted**

Department of Earth, Atmospheric and Planetary Sciences

Certified by... **Signature redacted** August 30, 2017



Kerry A. Emanuel

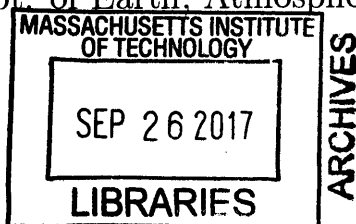
Cecil & Ida Green Professor of Atmospheric Science

Thesis Supervisor

Accepted by... **Signature redacted**

Robert D. van der Hilst

Schlumberger Professor of Earth and Planetary Sciences
Head of Dept. of Earth, Atmospheric and Planetary Sciences



Dependence of continental severe convective instability on climatological environmental conditions

by

John Vincent Agard

Submitted to the Department of Earth, Atmospheric and Planetary Sciences
on August 30, 2017, in partial fulfillment of the
requirements for the degree of
Doctor of Philosophy in Atmospheric Science

Abstract

Most of Earth's strongest atmospheric convection occurs over the continents, where potential energy is stored over time in metastable vertical profiles, only to be released rapidly by severe storms. In contrast to equilibrium-state convection in tropical ocean regions, there is a relative paucity of research exploring the climate dynamics of continental deep convection. This work makes a contribution to rectifying that deficiency by exploring the physical mechanisms by which convective available potential energy (CAPE) is generated, and their dependence on climatological properties of the Earth's environment.

First, a budget of the time tendency of CAPE is used to examine the buildup of CAPE in advance of severe convective storm events in North America via case studies using reanalysis data. Contributions to extreme peak CAPE from relative advection of air masses, diabatic heating of the surface boundary layer, and radiative cooling of the free troposphere are computed. In all 8 cases studied, CAPE buildup is found to be driven primarily by fluxes of heat and moisture from the surface into the boundary layer on sub-diurnal time scales, and not by radiative cooling or the relative advection of air masses at low and upper levels over multiple days.

This result is then further explored using an idealized two-dimensional continental framework using a minimal numerical model. Experiments in both 2-column and 40-column configurations demonstrate a link between discontinuities in surface moisture and high levels of transient CAPE. Surface entropy flux is once again found to be the primary driver of peak CAPE buildup within the model.

Finally, a thermodynamic constraint on CAPE in continental environments is established using an idealized, one-dimensional model. This theoretical model incorporates the physical principle of CAPE generation identified using reanalysis and two-dimensional modeling by considering a dry adiabatic column that comes into contact with a moist land surface. A system of equations is derived to describe the evolution of the ensuing surface boundary layer. From these, the maximum value of transient CAPE in the column can be found for any particular combination of surface temperature and moisture. It is demonstrated that, for a given range of surface

temperatures, the value of peak CAPE scales with the Clausius-Clapeyron relation.

Thesis Supervisor: Kerry A. Emanuel

Title: Cecil & Ida Green Professor of Atmospheric Science

Acknowledgments

It's hard to believe that I've been part of the EAPS community for almost 10 years now, first as an undergraduate and now as a graduate student. It's even harder to believe that I'll be leaving the Green Building soon to begin the next phase of my career. The time I've spent here has been both highly challenging and extremely enjoyable, and this thesis represents the culmination of a long effort that would not have been possible without the guidance, friendship, and support of a number of people.

First, I owe a great thanks to my advisor, Kerry Emanuel, for taking me on as a student (twice!) and providing caring mentorship throughout my time at MIT. Always willing to make time to provide guidance, Kerry's insights have consistently motivated me to strive for a deeper understanding of our science and the subjects of my research. At the same time, Kerry gave me the freedom to do things independently, which has proved to be an invaluable learning experience. Under Kerry, I have also had the opportunities to travel to conferences and workshops, gain unique teaching experience, and even participate in an operational forecasting experiment. These experiences have all been incredibly valuable to my development as a student and as a scientist.

I would also like to thank my thesis committee, Paul O'Gorman, Earle Williams, and Howie Bluestein for their time and valuable input. They have been instrumental in helping shape this thesis into its final form. I owe a particular thanks to Professor Bluestein for traveling to MIT or joining remotely for my committee meetings, and for taking interest in and providing thoughtful insights on my research.

The EAPS department has been a wonderful place to work, and I am thankful for the acceptance and support of its many community members. It's been a great pleasure to work alongside all of the talented members of the Emanuel group over the years. I'd like to extend thanks and congratulations to Andy Miller, who started and finished the PhD program at the same time as me, and has been a wonderful officemate and friend the entire time. We were lucky enough to share 54-1715 with Dan Chavas

and Marty Singh early in our graduate careers, whose guidance and friendship have been quite encouraging. I've also been privileged to make many new friends along the way, including Colin Thackray, Emily Zakem, Daniel Gilford, Michael McClellan, and many more. I'm also thankful to the PAOC faculty and administrative staff for creating an engaging and supportive learning environment. In particular, I'd like to thank Lodovica Illari for the opportunity to participate in DEAPS, WxChallenge, and so many other valuable and memorable experiences.

I certainly couldn't have accomplished any of this without my parents, John and Beth Agard. From the day I was born, they provided a nurturing environment, and always encouraged me to learn more, dream bigger, and achieve great things. I am who I am as a person because of them, and I dedicate this thesis to them. I am also thankful for the friendship and support of my brother, Erik, who is the greatest crossword constructor I've ever met. Finally, thank you Amanda for making me happy, and having my back through thick and thin. There is no challenge too great for us to tackle together.

Financial support for this research was provided in part by the National Science Foundation through grants ATM-0850639, AGS-1032244, and AGS-1418508. Additional funding was provided by the Bermuda Institute of Ocean Sciences Risk Prediction Initiative through grant RPI2.0-2012-02, and by the Office of Naval Research through grant N00014-14-1-0062. As a student, I received fellowship support from the MIT Office of the Dean for Graduate Education and the School of Science. The PAOC Houghton Fund provided outstanding support for travel and equipment.

Contents

1	Introduction	15
1.1	Background	15
1.1.1	Climatology of CAPE	17
1.1.2	Observed trends in CAPE and severe storm activity	19
1.1.3	Past studies with global and regional climate models	20
1.2	Motivation	22
1.2.1	Scientific	22
1.2.2	Societal	23
1.3	Objectives	24
2	Identification of sources of CAPE in North American severe weather environments	25
2.1	Introduction	25
2.2	Methods	27
2.2.1	CAPE tendency budget	27
2.2.2	Data	28
2.2.3	Procedure	29
2.3	Cases	30
2.4	Results	32
2.5	Discussion	39
3	Diagnosis of physical contributors to CAPE buildup in a simplified numerical framework	43

3.1	Introduction	43
3.2	Methods	45
3.2.1	Sensitivity experiments	48
3.2.2	Many-column configuration	49
3.3	Results	52
3.3.1	Sensitivity experiments	52
3.3.2	40-column configuration	59
3.4	Discussion	72
3.4.1	Role of surface properties in supporting CAPE buildup	72
3.4.2	Research limitations and errors	74
3.4.3	Future research	75
4	Clausius-Clapeyron scaling of peak CAPE	77
4.1	Introduction	77
4.2	Idealized model	79
4.3	Results	86
4.4	Scaling of peak CAPE	91
4.5	Discussion	97
5	Conclusions	99
5.1	Key findings	99
5.2	Future work	101
A	Equilibrium mean dynamic state of multi-column model in constant radiation experiment	105
B	Derivation of long-time moist static energy limit in asymptotic regime	109
C	Derivation of regime boundaries	111

List of Figures

2-1	SPC storm reports for the dates of each case study.	31
2-2	CAPE (J kg^{-1}) at the reanalysis time step immediately preceding the onset convection in each case. The hatched areas indicate the locations of the 99.9th percentile of CAPE values. Oceanic grid cells are masked.	33
2-3	Paths of boundary layer parcels of interest (blue) tracked backward in time for the 2 days before the composite time. Red lines indicate the paths of parcels that end up superimposed on the parcels of interest at the 700 hPa level at the composite time. Circles indicate the initial positions of each parcel at 00Z the day prior to the day of the composite.	34
2-4	Properties of the group of boundary layer parcels of interest along their backward trajectories for the April 28, 2012 case.	36
2-5	Time series of mean total CAPE tendency (dashed black line), and the contributions to CAPE tendency from diabatic heating (blue line), relative advection (red line), and radiative cooling (green line) for each case. The error bars represent the standard deviation spread of the individual parcels of interest.	37
2-6	Mean total accumulated CAPE (white), and contributions to CAPE accumulation from diabatic heating (blue), relative advection (red), and radiative cooling (green) in columns of interest for each case. . .	39

3-1	Schematic of the many-column configuration of the idealized numerical model. Each rectangle represents a region 10 columns in width, with a fixed evaporative fraction and oceanic mixed-layer depth. The red lines illustrate the prescribed background wind profile, which applies throughout the domain. Atmospheric advection between columns and regions is permitted, with a periodic reentry between the left and right edges of the domain. The depth of the bottom section of each section corresponds to the depth of its ocean surface, and therefore its effective heat capacity.	50
3-2	Mean equilibrium values of surface temperature (a), precipitation (b), CAPE (c), and vertical velocity at the 850 mb level (d) versus surface evaporative fraction of the low- α column in the ‘dry’ column (green) and the ‘wet’ column (blue) for the case with diurnally averaged radiation.	53
3-3	Mean daily maximum equilibrium values of surface temperature (a), precipitation (b), CAPE (c), and vertical velocity at the 850 mb level (d) versus surface evaporative fraction of the low evaporative fraction column in the ‘dry’ column (green) and the ‘wet’ column (blue) for the case with diurnally varying radiation.	55
3-4	Mean equilibrium values of surface temperature (a), precipitation (b), CAPE (c), and vertical velocity at the 850 mb level (d) versus surface albedo of the varying albedo column in the column in which albedo is being modulated (green) and column in which it is held constant (blue) in the domain for the case with diurnally averaged radiation.	57
3-5	Mean daily maximum equilibrium values of surface temperature (a), precipitation (b), CAPE (c), and vertical velocity at the 850 mb level (d) versus surface albedo of the varying albedo column in the column in which albedo is being modulated (green) and column in which it is held constant (blue) for the case with diurnally varying radiation.	58

3-6	Heat map diagram showing the number of timesteps (shading) in equilibrium at which the CAPE falls into a given range of values (J/kg, vertical axis) in each model column (horizontal axis) for the case of diurnally averaged radiation. The vertical dashed lines indicate the boundaries between the ocean, ‘dry’ land, and ‘wet’ land regions. . . .	60
3-7	Heat map diagram showing the number of timesteps (shading) in equilibrium at which the CIN falls into a given range of values (J/kg, vertical axis) in each model column (horizontal axis) for the case of diurnally averaged radiation. The vertical dashed lines indicate the boundaries between the ocean, ‘dry’ land, and ‘wet’ land regions. . . .	62
3-8	Heat map diagram showing the number of days (shading) in equilibrium at which the maximum value of CAPE falls into a given range of values (J/kg, vertical axis) in each model column (horizontal axis) for the case of diurnally varying radiation. The vertical dashed lines indicate the boundaries between the ocean, ‘dry’ land, and ‘wet’ land regions.	63
3-9	Heat map diagram showing the number of days (shading) in equilibrium at which the maximum value of CIN falls into a given range of values (J/kg, vertical axis) in each model column (horizontal axis) for the case of diurnally varying radiation. The vertical dashed lines indicate the boundaries between the ocean, ‘dry’ land, and ‘wet’ land regions.	65
3-10	Composites of hourly equilibrium means in surface temperature (a), precipitation (b), and zonal wind (c) for the case in which a diurnal cycle of radiation is used. The vertical dashed lines indicate the boundaries between the ocean, ‘dry’ land, and ‘wet’ land regions.	66
3-11	As in 3-10, but for CAPE (a) and CIN (b).	68
3-12	Skew-T diagram for westernmost ‘moist’ column at the time of peak CAPE.	69

3-13	Hourly mean equilibrium contributions to the tendency of CAPE by each term in (3.5). The vertical dashed lines indicate the boundaries between the ocean, ‘dry’ land, and ‘wet’ land regions. The color scales are not the same for each image.	70
3-14	Hourly mean equilibrium values of the LHS (a) and RHS (b) of (3.5). The vertical dashed lines indicate the boundaries between the ocean, ‘dry’ land, and ‘wet’ land regions.	71
4-1	Schematic of the single-column idealized model (a) before introduction of the moist surface and boundary layer, (b) at the initial time, and (c) during its evolution. Indicated on each diagram are the dry static energy (D), moist static energy (M), temperature (T), and specific humidity (q) of each part of the system.	81
4-2	Numerically integrated time series of (a) δ , (b) μ , and (c) η for $T_0 = 305$ K, $\alpha = 0.5$, $h_0 = 100$ m, $v_{\text{sfc}} = 5$ m s ⁻¹ , and $F_{\text{rad}} = 200$ W m ⁻²	87
4-3	Skew-T diagrams depicting the vertical profile of temperature (solid black line) and dew point temperature (dashed black line) for an example model solution in which $T_0 = 305$ K, $\alpha = 0.5$, $h_0 = 500$ m, $v_{\text{sfc}} = 5$ m s ⁻¹ , and $F_{\text{rad}} = 200$ W m ⁻² , at (a) $t < 0$, (b) $t = 0$, (c) the time at which maximum CAPE is achieved, and (d) the same time as (c), but with the temperature of the free troposphere relaxed to that of the U.S. Standard Atmosphere (1976).	88

4-4	<p>Top panel: Time evolution of boundary layer dry static energy (solid blue line) and surface dry static energy (solid red line) for three different values of T_0, with $\alpha = 0.5$, $h_0 = 100$ m, $v_{\text{sfc}} = 5$ m s⁻¹, and $F_{\text{rad}} = 200$ W m⁻². Boundary layer dry static energy is plotted as $1 - \delta$ to provide a nondimensionalized measure of near-surface air temperature. The dashed black line at $\delta = 1$ represents the level at which temperature is equal to T_0. Bottom panel: Time evolution of the moist static energy surplus corresponding to each case. Panels a, b, and c represent the peak, intermediate, and asymptotic regimes, respectively.</p>	89
4-5	<p>Maximum relative humidity achieved at the top of the boundary layer during its evolution as a function of T_0 and α, for $h_0 = 100$ m, $v_{\text{sfc}} = 5$ m s⁻¹, and $F_{\text{rad}} = 200$ W m⁻².</p>	91
4-6	<p>Evolution of CAPE with time for several different values of T_0, given $\alpha = 0.5$. Here, CAPE is nondimensionalized by a factor of $\rho C_T v_{\text{sfc}} F_{\text{rad}}^{-1}$, while time is nondimensionalized according to (4.18). The dashed black line displays the end of a 12-hour diurnal time scale corresponding to the particular parameter choices $h_0 = 100$ m and $v_{\text{sfc}} = 5$ m s⁻¹.</p>	93
4-7	<p>Modeled dimensional peak CAPE as a function of T_0 (solid green line) for $\alpha = 0.5$, $h_0 = 100$ m, $v_{\text{sfc}} = 5$ m s⁻¹, and $F_{\text{rad}} = 200$ W m⁻²; and a theoretical curve (dashed red line) corresponding to the asymptotic limit of CAPE that arises as $t \rightarrow \infty$, or $h_0 \rightarrow 0$. This curve is an exact solution to the Clausius-Clapeyron relation, as described by (4.38). The dotted black lines indicate the boundaries between the three regimes of model solutions.</p>	94
4-8	<p>Modeled maximum CAPE within a diurnal time scale, as a function of T_0 for $\alpha = 0.5$, $h_0 = 100$ m, $v_{\text{sfc}} = 5$ m s⁻¹, and $F_{\text{rad}} = 200$ W m⁻².</p>	95
4-9	<p>Modeled maximum CAPE within a diurnal time scale, as a function of T_0 with varying α, v_{sfc}, and h_0.</p>	96

A-1 Mean equilibrium cross sections of vertical velocity (a), parameterized convective updraft mass flux (b), temperature perturbation from the zonal mean (c), and relative humidity (d) for the case of diurnally averaged radiation. The dotted lines indicate the boundaries between the ocean, ‘dry’ land, and ‘wet’ land regions. 106

Chapter 1

Introduction

Convective rainstorms occur on a daily basis in the Earth's atmosphere, and constitute an important component of the climate system. However, the most severe convective storms— those which can pose a significant danger to life and property— are much less spatially and temporally frequent. In fact, these storms tend to occur most frequently in just a few specific regions of the planet (Zipser et al. 2006), primarily over land. Such severe convective storms often create hazards such as tornadoes, large hail, and strong winds. In certain continental regions, these storms occur with a known climatological frequency of multiple days per year (Brooks et al. 2003a; Doswell III et al. 2005). But what sets this climatology, and how might the distribution of severe local storms be expected to change as the Earth's climate changes? This thesis aims to shed some light on these as-of-yet unanswered questions by determining the ways in which the atmosphere is preconditioned for severe convection over land, and developing a theory to constrain available severe storm energy as a function of climatological properties of the physical environment.

1.1 Background

A certain set of dynamic and thermodynamic conditions must be met for continental severe convection to occur. Among the necessary ingredients are convective available potential energy (CAPE), deep-layer vertical wind shear, low-level moisture, and

dynamical uplift capable of initiating storms (Doswell III et al. 1996; Brooks 2009; Grams et al. 2012; Bluestein 2007, 2013). In particular, CAPE and shear are the variables primarily responsible for determining the climatology of severe local storms over land. This thesis focuses solely on CAPE as a measure of the thermodynamic capacity of a given environment to support deep convection. Of course, this is only one part of the puzzle, and further work on the dynamical side is necessary to make theory-based determinations about the overall distribution of severe storms as a function of climate. Still, the role of CAPE in constraining severe storm climatology is quite significant, and a better understanding of its dependence on environmental factors is pertinently needed.

Herein, CAPE is defined as a measure of the integrated buoyancy of a parcel of air lifted pseudoadiabatically through a given column of the atmosphere. It is calculated according to

$$CAPE_i = \int_{p_{L_i}}^{p_i} (\alpha_p - \alpha_e) dp = R_d \int_{p_{L_i}}^{p_i} (T_{v_p} - T_{v_e}) d \ln p \quad (1.1)$$

for a parcel of air lifted from the level with pressure p_i and whose pressure level of neutral buoyancy is p_{L_i} , where α_p and α_e are the specific volumes of the parcel and the environment, respectively. R_d is the gas constant for dry air, and T_{v_p} and T_{v_e} are the virtual temperatures of the parcel and the environment, respectively. Virtual temperature is defined by

$$T_v = T \left[1 - \frac{e}{p}(1 - \epsilon) \right]^{-1}, \quad (1.2)$$

where e is the partial pressure of water vapor, and $\epsilon = 0.622$ is the ratio of the molecular weight of water vapor to that of dry air.

Assuming an inviscid atmosphere, the maximum updraft speed of convective thunderstorms is proportional to the square root of CAPE (Holton 2004; Bluestein 2007). Of course, the real atmosphere is not inviscid, and entrainment of environmental air into rising plumes tends to act as a sink of potential energy, diluting the buoyancy

of rising parcels and reducing resultant updraft speeds. Still, observations show that particular types of continental severe convection including supercells are typically associated with high CAPE (Rasmussen and Blanchard 1998; Brooks et al. 1994; Grams et al. 2012), and numerical modeling studies such as Weisman and Klemp (1982) still find a positive correlation between environmental CAPE and storm updraft speed. Since high updraft speeds are associated with severe effects such as high winds, strong downdrafts, and large hail, thunderstorms with these damaging components occur primarily in environments with high CAPE. Furthermore, Romps et al. (2014) find that the lightning flash rate in thunderstorms is proportional to the product of CAPE and precipitation rate, meaning increases in CAPE correspond with increases in lightning strikes.

Rasmussen and Blanchard (1998) find that CAPE levels are significantly higher in environments in which supercells form than in those supporting non-supercell thunderstorms. Bluestein (2007) notes that many supercells are associated with CAPE values in excess of 1500 J kg^{-1} , although under certain shear conditions, supercells often occur with minimum CAPE values of $500\text{-}1000 \text{ J kg}^{-1}$ (Bluestein 2013). Furthermore, both López et al. (2001) and Niall and Walsh (2005) find significant correlations between CAPE and hailstorms in observational data in the Iberian Peninsula and southeastern Australia, respectively. It is therefore apparent that CAPE is an important property with respect to the preconditioning of the atmosphere for supercell thunderstorms and those that produce severe hazards.

1.1.1 Climatology of CAPE

Although direct observations of CAPE require full atmospheric soundings and therefore are relatively sparse, more spatially complete CAPE climatologies can be computed using reanalysis data. Brooks et al. (2003b) use NCEP/NCAR Reanalysis data to calculate the frequency of high CAPE occurrences over the United States, with the finding that environmental CAPE levels are in excess of 2000 J/kg on more than 10 days per year in the central Plains and Midwest, as well as in some parts of Mississippi and Louisiana. The regions in which extreme CAPE occurs most frequently

are roughly coincident with those in which severe storm hazards such as tornadoes (Brooks et al. 2003a) and large hail (Doswell III et al. 2005) are most often observed. Brooks et al. (2003b) also includes a global analysis that determines that these regions experience favorable parameters for severe local storms with the greatest frequency of any regions on Earth.

Similarly, Grumm (2005) uses North American Regional Reanalysis (NARR) data to produce maps of mean afternoon CAPE values across North America. Their results also show CAPE maxima in the Southeastern United States and in the central and southern Plains, with the CAPE field exhibiting the highest variability in the Plains and Midwestern states. Furthermore, this variability is found to exhibit a seasonal signal, with maxima moving northward from the southern Plains into the northern Plains and Midwest over the course of the spring and early summer. Solomon et al. (2013) are also able to reproduce the results of Brooks et al. (2003b) using North American Regional Reanalysis (NARR) data to produce a climatology of the number of days per year with severe local storms in the United States. The spatial pattern and annual cycle of severe storm frequency as calculated from these reanalysis data match those of tornado frequency as calculated from observations by Brooks et al. (2003a).

Previous literature has established an explanation for the relative climatological prevalence of anomalously high CAPE in central North America: Hot, dry air from the elevated desert regions of the Southwest is advected eastward by the prevailing wind aloft, creating a low- to mid-level temperature inversion, and thereby inhibiting the initiation of convection of warm, moist air parcels closer to the surface (Carlson and Ludlam 1968; Lanicci and Warner 1991; Banacos and Ekster 2010). Columns of atmosphere in which this occurs become convectively metastable, a state in which CAPE can grow continuously until sufficient thermodynamic or mechanical forcing occurs to overcome the convective inhibition posed by the elevated mixed layer. As such, severe convective storms over the continents rely on a paradigm of cumulative stored potential energy, in which CAPE is progressively generated over time, and reaches transient peak before being consumed. This mechanism stands in contrast to

that of convective environments over the tropical oceans, where radiative-convective equilibrium dictates a quasi-steady background level of CAPE (Rennó and Ingersoll 1996).

The magnitude of the barrier to convection presented by the inversion layer in a given column of atmosphere can be quantified using convective inhibition (CIN), as defined by

$$CIN = \int_{p_{LFC}}^{p_{sfc}} (\alpha_e - \alpha_p) dp = R_d \int_{p_{LFC}}^{p_i} (T_{v_e} - T_{v_p}) d \ln p, \quad (1.3)$$

as in Williams and Rennó (1993) (this quantity is equivalent to the “negative area” (NA) discussed in Emanuel (1994)), where *LFC* denotes the level of free convection of the lifted parcel.

Previous studies have used observational and reanalysis data to analyze CIN in severe local storm environments. Grams et al. (2012) finds CIN values of around 25 to 150 J kg⁻¹ for United States supercells that produced severe hail or wind, with values a bit lower in tornadic supercell environments. Riemann-Campe et al. (2009) use ERA-40 reanalysis data to generate a global climatology of CAPE and CIN, Relatively high mean climatological values of CAPE are found over central North America, northern Chile, and the coast of India, especially in the March-April-May (MAM) season. CIN in these regions is also found to be maximum in MAM. The global spatial maxima of CIN are located elsewhere, but other instances of high CIN are generally not associated with extreme CAPE.

1.1.2 Observed trends in CAPE and severe storm activity

Several studies identify trends in severe storm activity that could be associated with climate change. Observed measures of severe hail are found to be increasing in France (Dessens 1995) and Ontario, Canada (Cao 2008). Reanalysis data are used by Riemann-Campe et al. (2009) to detect trends in CAPE and CIN over the time period of the ERA-40 data set. These data show a generally positive trend in mean CAPE values in middle latitudes. This trend is especially large in continental North

America for the summer months (JJA). CIN is likewise found to be increasing in all seasons other than autumn. Combined increases in CAPE and CIN would suggest an increase in the intensity of convective storms, as stronger forcing is required to release a larger amount of energy. However, the signs of these trends are found to have reversed in the years since 1979. This phenomenon is attributed to low frequency CAPE variability, although the study refrains from speculating on a physical explanation for this variability.

Cook and Schaefer (2008) analyze United States winter tornado reports to find a significant correlation with the phase of the El Niño-Southern Oscillation (ENSO). This connection is found to be due to nonlinear effects of ENSO on the large-scale forcing over North America. This is an example of the modulation of the interannual climatology of continental severe convection by a long-term, planetary-scale atmospheric process.

1.1.3 Past studies with global and regional climate models

While severe local storms occur on horizontal scales too small to be resolved by numerical climate models, several studies have attempted to indirectly predict the evolution of the climatological state of severe storms by calculating quantities such as CAPE from the output of global or regional climate models (GCMs/RCMs). Most notably, Trapp et al. (2007a) use a combination of GCMs and RCMs to predict the spatial distributions of CAPE, vertical wind shear, and surface specific humidity over the United States through the end of the 21st century under a given emissions scenario. These models produce increases in CAPE and surface specific humidity throughout the country in the spring and summer months with respect to baseline climatological values established from reanalysis data. These differences are more pronounced in JJA, especially for the CAPE field, in which increases of over 500 J/kg are predicted for parts of the Southeast region. Although shear is found to decrease in the models, the frequency of severe thunderstorm-supporting conditions is found to increase throughout much of the domain on the order of a few days per season. A similar conclusion is reached by Solomon et al. (2013), who use a GCM to find

an increase of similar order in frequency of conditions favorable to severe convection across the Great Plains and Midwest and April, May, and June (AMJ). Contrastingly, Niall and Walsh (2005) find a decrease in CAPE for the Mount Gambier region of Australia under a doubling of atmospheric CO₂ using an RCM. These studies do not analyze in depth the mechanism by which CAPE would increase, aside from an attribution to the predicted increase in low-level temperatures.

Likewise, Del Genio et al. (2007) use a GCM to diagnose convective updraft speeds (by way of calculating buoyancy) in a scenario in which atmospheric CO₂ is doubled. In this scenario, convective intensity is found to increase by amounts on the order of 1 m/s globally over land. However, in midlatitudes, the overall nature of moist convection is found to be unchanged with the exception that the most severe storms become more frequent. This result is attributed to an increase in the severity of gradients and shear along frontal boundaries, as CAPE is increased through increased latent heating.

Trapp et al. (2007b) propose a nested model approach for modeling severe local storms in the context of climate. By nesting cloud-resolving models inside of GCMs and RCMs, small-scale convective processes are able to be explicitly simulated, while large-scale forcing remains the province of the coarse-resolution climate models. This approach is validated against historical severe convective events as a demonstration of feasibility for future climate studies.

Ye et al. (1998) use a GCM to estimate the climate sensitivity of CAPE in the present climate as well as in future climate scenarios. In this case, it is found that the climate sensitivity of CAPE is predicted to decrease as variations in boundary layer entropy become less important in CAPE production with respect to changes in upper-level warming. This thesis aims to further unpack that hypothesis by directly examining the different mechanisms through which CAPE is controlled in the planetary boundary layer and in the free troposphere.

Other studies have used the Coupled Model Intercomparison, Phase 5 (CMIP5) suite of climate models to simulate future changes in continental severe storm climatology. Diffenbaugh et al. (2013) project an increase in days with high CAPE and low

CIN in conjunction with sufficient shear to support severe convection over the United States. Likewise, Romps et al. (2014) use 11 CMIP5 models to project an increase in lightning flash rate with warming temperatures as a result of increasing CAPE. Seeley and Romps (2015) use a subset of 4 CMIP5 models to project an increase in frequency of favorable conditions for severe storms in the United States over the 21st century. That study identifies divergent projections for CAPE and boundary layer moisture as a source of uncertainty in climate models with regard to atmospheric preconditioning for continental deep convection.

Trapp and Hoogewind (2016) also use CMIP5 models, but in this case they are used to obtain a projected base state in which to conduct high-resolution pseudo-global warming experiments using the Weather Research and Forecasting model. These simulations project increases in both CAPE and CIN, resulting in fewer storms but stronger updrafts in those that do develop.

Finally, Gensini and Mote (2015) use high-resolution dynamical downscaling to directly simulate continental convective storms in environments produced by the Community Climate System Model version 3, finding an increase in hazards including tornadoes, large hail, and high winds in several regions of the United States. In particular, their simulations show an increase in severe convection in the late afternoon hours of the days on which it occurs. The projected changes in severe storm activity are attributed primarily to changes in CAPE and deep-layer shear.

1.2 Motivation

1.2.1 Scientific

Until recently, relatively little work had been done at the intersection of continental deep convection and climate. Now, a growing body of literature has begun to examine the variability of severe local storms as a function of climate. In the context of the rapidly developing observation-based and climate model-based understanding of the climate dynamics surrounding the problem, this thesis aims to establish a theoretical

understanding of the influence of climatological environmental variables on the thermodynamic preconditioning of the atmosphere for deep convection over continents. The research contained herein may serve as the basis for future work that will further elucidate the trends and variability of severe convective storms on interannual to multidecadal time scales.

1.2.2 Societal

Severe convection over land poses a significant threat to life and property, particularly in regions such as the Great Plains of the United States, in which it most frequent and intense. Threats from these storms include high winds, hail, tornadoes, and flooding. For instance, in 2011, there were 1,894 reported tornadoes in the United States, resulting in 553 reported deaths (Storm Prediction Center 2011). Between the years 1950 and 1994, there were \$26.3 billion (1997 USD) in insured losses from tornadoes alone (Changnon 2001). Changnon (2001) also finds that there were \$87.2 billion (1998 USD) in reported losses from all thunderstorm catastrophes between the years 1949 and 1998, with a significant upward trend in loss amounts after 1974. Furthermore, Changnon (2009) finds that major American loss events associated with hailstorms have significantly increased in frequency and magnitude since 1990. Average annual damage to crops and other properties has also trended higher in recent years (Rosenzweig et al. 2002; Botzen et al. 2010). However, although measures of severe hail have been found to be increasing in other regions of the world (Dessens 1995; Cao 2008), it is uncertain whether these increases in insured losses are due to climatological changes in storm frequency or severity, due to increases in exposure and vulnerability of property to severe storms, or due to some combination of both factors (Changnon 2009; Bouwer 2011). By providing theoretical insights on the thermodynamic constraints on the conditions that give rise to dangerous severe convective hazards as a function of climate, this thesis aims to produce a baseline upon which future predictions of these hazards could be improved.

1.3 Objectives

In this thesis, the problem of constraining the scale of CAPE in continental convective environments as a function of climatological environmental variables is attacked in three parts. First, a budget for the time tendency of CAPE is applied to reanalysis data to determine the primary physical mechanism responsible for the buildup of CAPE in advance of severe storm events. This work is detailed in Chapter 2. Next, in Chapter 3, an idealized, two-dimensional numerical model is used to test the results of Chapter 2 and demonstrate the viability of extreme transient peak CAPE under certain simplified environmental conditions. Finally, in Chapter 4 a simple, one-dimensional initial-value model is developed to provide a theoretical scaling for peak continental CAPE as a function of temperature and other properties of the land surface. Chapter 5 aggregates the key findings from each of these individual works, and concludes with an overarching discussion in the context of the goals of the thesis and potential future research opportunities.

Chapter 2

Identification of sources of CAPE in North American severe weather environments

2.1 Introduction

CAPE is a key thermodynamic property of the atmosphere in determining the favorability of a given environment to convection. The intensity of a thunderstorm is theoretically tied to the amount of CAPE present in its environment (Weisman and Klemp 1982; Brooks et al. 1994; Holton 2004). When convection is triggered, the environmental CAPE is depleted by conversion to kinetic energy, in the form of vertically overturning motions. Environments with more CAPE therefore support storms with more vigorous updrafts, which in turn contribute to convective storm severity by supporting larger hydrometeors, more frequent lightning, and stronger winds at the surface (Williams et al. 1992). As such, CAPE is considered one of three necessary ingredients for deep convection over land (Doswell III et al. 1996), along with

The contents of Chapter 2 are submitted for publication in *Monthly Weather Review*. A few minor edits have been made to the submitted work for the purpose of clarity in the context of this thesis.

moisture and dynamical lift.

CAPE can reach particularly high levels over the continents, where energy is stored gradually over time in conditionally unstable profiles, only to be released rapidly by severe convective storms (Emanuel 1994). This is particularly evident in the climatological records of severe local storm hazards, such as tornadoes and severe hail. Regions such as the Great Plains and Midwest of North America, where the aforementioned hazards are most frequently observed, are coincident with the areas in which some of the world's highest levels of CAPE can be found (Brooks et al. 2003b; Zipser et al. 2006).

As discussed in Section 1.1.1, the occasional occurrence of exceptionally high CAPE over land is made possible by the presence of elevated mixed layers— layers of hot, dry air aloft that act as barriers to convection, thereby allowing entropically rich air to be trapped near the surface. This process gives rise to metastable atmospheric profiles with anomalously high CAPE in a way that is unique to particular continental environments.

While high CAPE is far from the only parameter necessary for severe convection over land, studying the origins of high CAPE can yield a better understanding of how, in a dynamical sense, the environment is preconditioned to support severe thunderstorms. In North America, the canonical explanation for particularly high-CAPE situations is a synoptic setup in which the elevated mixed layer is generated in the southwestern high desert, and advected by mid-level westerlies over the Plains or Midwest. Concurrently, warm, moisture-laden air from the Gulf of Mexico is thought to provide the low-level entropy necessary to create significant instability as it is advected northward at low levels (Emanuel 1994; Johnson and Mapes 2001; Brooks et al. 2003a; Schultz et al. 2014). Therefore, the presence and relative locations of the hot, dry desert and warm, moist Gulf are thought to be important for informing the climatological distribution of the occurrences of high CAPE, and thereby of severe convection, in North America.

Although this mechanism is generally accepted as being principally responsible for the buildup of CAPE in advance of severe storm events in central North America, a

quantitative exploration of the physical mechanisms responsible for supplying CAPE to continental convective environments has yet to be undertaken. This study aims to quantify the contributions to CAPE buildup of particular dynamical and thermodynamical processes in advance of North American severe storm events. In doing so, we aim to improve the quantitative theoretical understanding of the climatology of extreme peak CAPE, and thereby of severe convective storms.

2.2 Methods

2.2.1 CAPE tendency budget

Case studies are performed in which reanalysis data are used to construct a budget of the time tendency of CAPE leading up to the onset of severe convection. Following Emanuel (1994), the time tendency of CAPE can be calculated in a Lagrangian sense, wherein the time derivative is taken following the motion of a parcel to be lifted from the surface boundary layer:

$$\frac{d}{dt}CAPE_b \approx (T_b - T_L) \frac{ds_b}{dt} - \int_{p_L}^{p_b} \left[\frac{R_d \dot{Q}}{c_p} \left(\frac{T_v}{T} \right) - \frac{R_d T_v}{\theta} (\mathbf{u}_r \cdot \nabla \theta) \right] d \ln p, \quad (2.1)$$

where

- the subscript b refers to the boundary layer level from which the parcel is to be lifted,
- the subscript L refers to the parcel's level of neutral buoyancy,
- $\mathbf{u}_r = \mathbf{u} - \mathbf{u}_b$ is the three-dimensional velocity vector of air in the free troposphere relative to that of air at the boundary layer lifting level,

and the individual terms on the right-hand side represent the components of CAPE tendency attributable to

- (i) $(T_b - T_L) \frac{ds_b}{dt}$, changes in the entropy of the boundary layer (via diabatic heating),

- (ii) $\int_{p_L}^{p_b} \frac{R_d \dot{Q}}{c_p} \left(\frac{T_v}{T} \right) d \ln p$, radiative heating or cooling of the free troposphere,
- (iii) $\int_{p_L}^{p_b} \frac{R_d T_v}{\theta} (\mathbf{u}_r \cdot \nabla \theta) d \ln p$, relative advection of the free tropospheric and boundary layer air masses.

Terms (i) through (iii) account for the entirety of the Lagrangian tendency of CAPE in a particular column, with the exception of the depletion of CAPE by convection itself, which is not reflected in (2.1). Therefore, the case studies conducted here deal only with the buildup of CAPE in advance of convection, and do not compute the CAPE tendency budget for times after convection has begun.

In the scenario in which the supply of low-level ‘‘Gulf air’’ is responsible for generating CAPE, the CAPE tendency budget should be dominated by term (iii), since parcels traveling in the Gulf air mass near the surface are entering columns with cooler air and steeper lapse rates aloft. In other words, one would expect the advection of the cool, continental air mass aloft relative to the warm, moisture-laden Gulf air mass at the surface to be the primary driver of CAPE buildup.

2.2.2 Data

Data from the North American Regional Reanalysis (NARR) (Mesinger et al. 2006) from the years 2012–2014 are used to compute the individual terms of the CAPE tendency budget in each case. NARR is chosen for its high temporal (3-hourly) and spatial (0.3-degree) resolution, which allow the derivatives in (2.1) to be reasonably approximated by finite differences. Unfortunately, NARR does not contain 4-dimensional radiative heating data, so data from the Modern-Era Retrospective analysis for Research and Applications, Version 2 (MERRA-2) (Gelaro et al. 2017) are used in the computation of term (ii). MERRA-2 data also have 3-hourly temporal resolution, but their spatial resolution is roughly 0.5-degree, so these data are interpolated to the NARR grid for the purpose of the tendency budget calculation. Terms (i) and (iii), as well as the left-hand side of (2.1) are directly computed from NARR.

2.2.3 Procedure

Cases are identified by searching the United States National Oceanic and Atmospheric Administration Storm Prediction Center (SPC) database of daily severe local storm reports for days in which particularly significant storms occurred. Using the storm reports and NARR, the onset time of convective activity is identified as the output time step at which the reanalysis first shows convective precipitation in a region in which storms were reported. The previous time step in NARR output is selected as time $t = 0$ for the initial analysis.

Using the temperature, pressure, and humidity fields in NARR, CAPE is calculated for the entire NARR domain at time $t = 0$, according to

$$CAPE = \int_{p_L}^{p_b} R_d(T_{v_p} - T_{v_e})d\ln p, \quad (2.2)$$

where T_{v_p} and T_{v_e} are the virtual temperatures of the lifted parcel and of the environment, respectively. The level from which parcels are to be lifted is taken as the lowest output level above the surface (determined using the NARR surface pressure field). These parcels are hereafter referred to as boundary layer parcels. Columns in which CAPE is in the 99.9th percentile (for the entire domain at that particular time step) at the composite time $t = 0$ are identified as the columns of interest.

The locations of the boundary layer parcels in each column of interest are then tracked backward in time using the NARR 3-dimensional wind field for the 2 days prior to the composite time. A given parcel will cease to be followed if it intersects terrain, or if it intersects another parcel of interest. At each prior output time step, the CAPE in each remaining column of interest is calculated.

From the calculated values of CAPE, the total Lagrangian CAPE tendency is calculated as a finite difference for each column between each time step. Likewise, the 3-dimensional wind and temperature fields in NARR are used to calculate the right-hand side terms (i) and (iii) of the CAPE tendency budget, and the MERRA radiative heating data are introduced to calculate (ii).

The results of these calculations are individual time series of the total CAPE

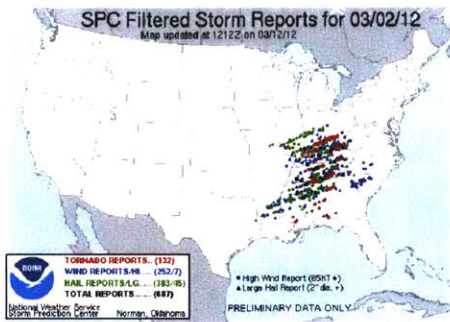
tendency and each of its individual components for each of the columns of interest. By averaging over all columns of interest, a single time series is obtained for each term in (2.1). Comparing these time series reveals the relative importance of each physical mechanism described in the CAPE tendency budget, as a function of time leading up to the onset of severe convection.

Finally, the time series corresponding to each component and the total CAPE tendency are integrated in time to arrive at a metric of the total accumulated CAPE attributable to each process. By comparing the magnitudes of the total accumulated CAPE attributable to each physical process with the total magnitude of overall CAPE buildup, conclusions are formed with respect to the relative importance of each physical process in generating the CAPE necessary for a particular severe storm event.

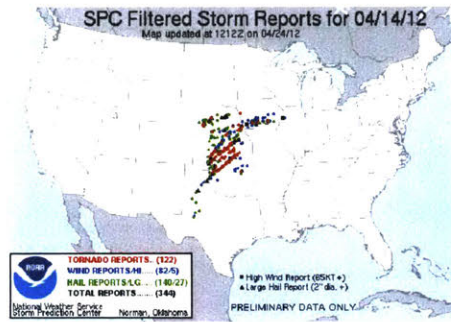
2.3 Cases

Eight instances of severe convective storm activity are identified from the 2012–2014 period. For each instance, a case study is conducted for the buildup of CAPE in advance of the start of convection. Each of the days selected corresponds to a series of severe storms that were observed somewhere in the Great Plains, Midwest or Southeastern United States. Figure 2-1 shows the reports of severe wind, hail, and tornadoes for each selected day from the SPC database.

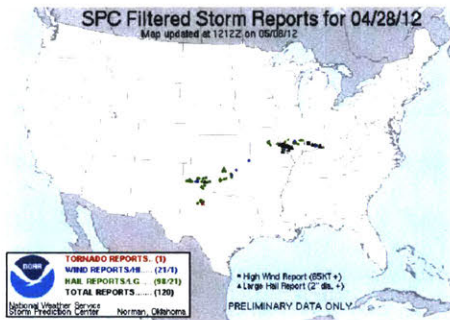
The selected cases encompass a variety of continental severe convective modes. Case (a), from March 2, 2012, is an example of an early-season tornado outbreak in the Southeastern United States, with a number of long-lived discrete cells tracking linearly across several states. Case (b), from April 14, 2012, is a similar tornado outbreak associated with a low-pressure system in the Great Plains. Cases (c) and (d), from April 28, 2012 and May 19, 2012, respectively, feature supercellular convection triggered along a stationary boundary. Cases (e) and (f), from May 20, 2013 and May 31, 2013, respectively, feature supercellular storms forming in especially high-CAPE environments over the Great Plains, and growing upscale into mesoscale convective



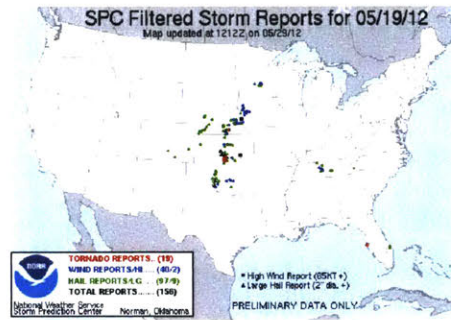
(a) March 2, 2012



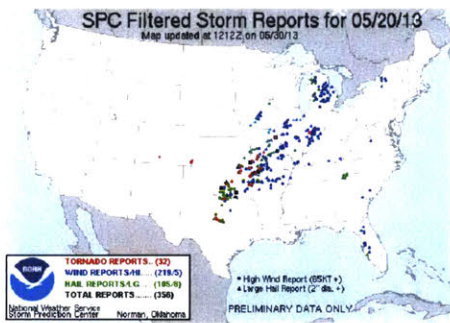
(b) April 14, 2012



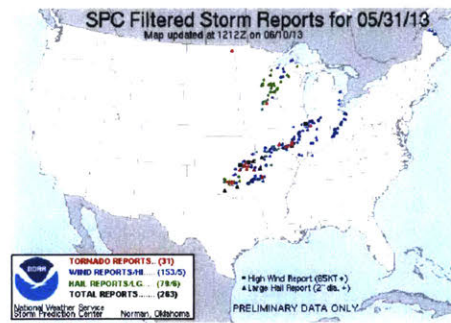
(c) April 28, 2012



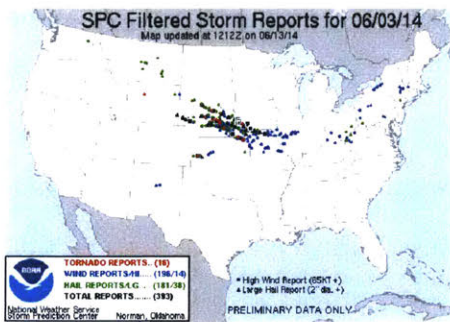
(d) May 19, 2012



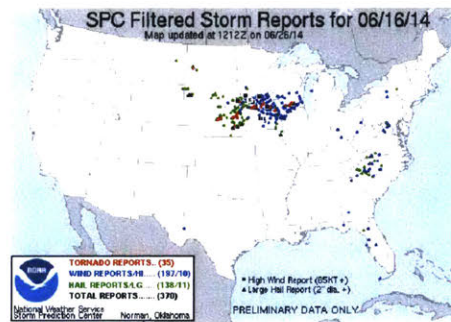
(e) May 20, 2013



(f) May 31, 2013



(g) June 3, 2014



(h) June 16, 2014

Figure 2-1: SPC storm reports for the dates of each case study.

systems as they propagated downstream into the Midwest. Finally, later-season convection in the Upper Plains/Midwest is featured in cases (g) and (h), from June 3, 2014 and June 16, 2014, respectively.

Attempts were made to identify nighttime convective outbreaks in the reanalysis data set and observational record. However, in each potential case in which severe convection occurred nocturnally, convection was found to have been initially triggered during the daytime. Since the CAPE tendency budget (2.1) does not account for the sink of CAPE by convection itself, these cases are untenable for the purposes of this study.

In each of these instances, the observed storms form in areas of anomalously high CAPE. The high CAPE exists in the presence of an inhibitive cap aloft that traps entropically rich air near the surface, thereby allowing a transient, but extreme level of instability in a particular region. The methodology outlined in Section 2 is used to identify the physical mechanisms by which anomalously high CAPE is generated in each case.

2.4 Results

For each case, the NARR output time step immediately preceding the initiation of convection is identified, and CAPE is calculated according to 2.2 for the entire NARR domain. The result of this calculation is shown in Figure 2-2. Figure 2-2 also shows the locations of the points of interest in which CAPE is in the 99.9th percentile at the composite time for each case. These points of interest roughly correspond to the areas in which severe convective storms develop in the hours immediately following the time of the composites. While the correspondence is not entirely 1-to-1 (for instance, many storm reports in case (g) are situated to the west of the region of interest), the CAPE at the algorithmically identified points of interest is taken as a representative sample of the energy responsible for supporting severe storms in each case.

Figure 2-3 shows the calculated backward trajectories of the boundary layer parcels that end up in the columns of interest at the time of composite. Addition-

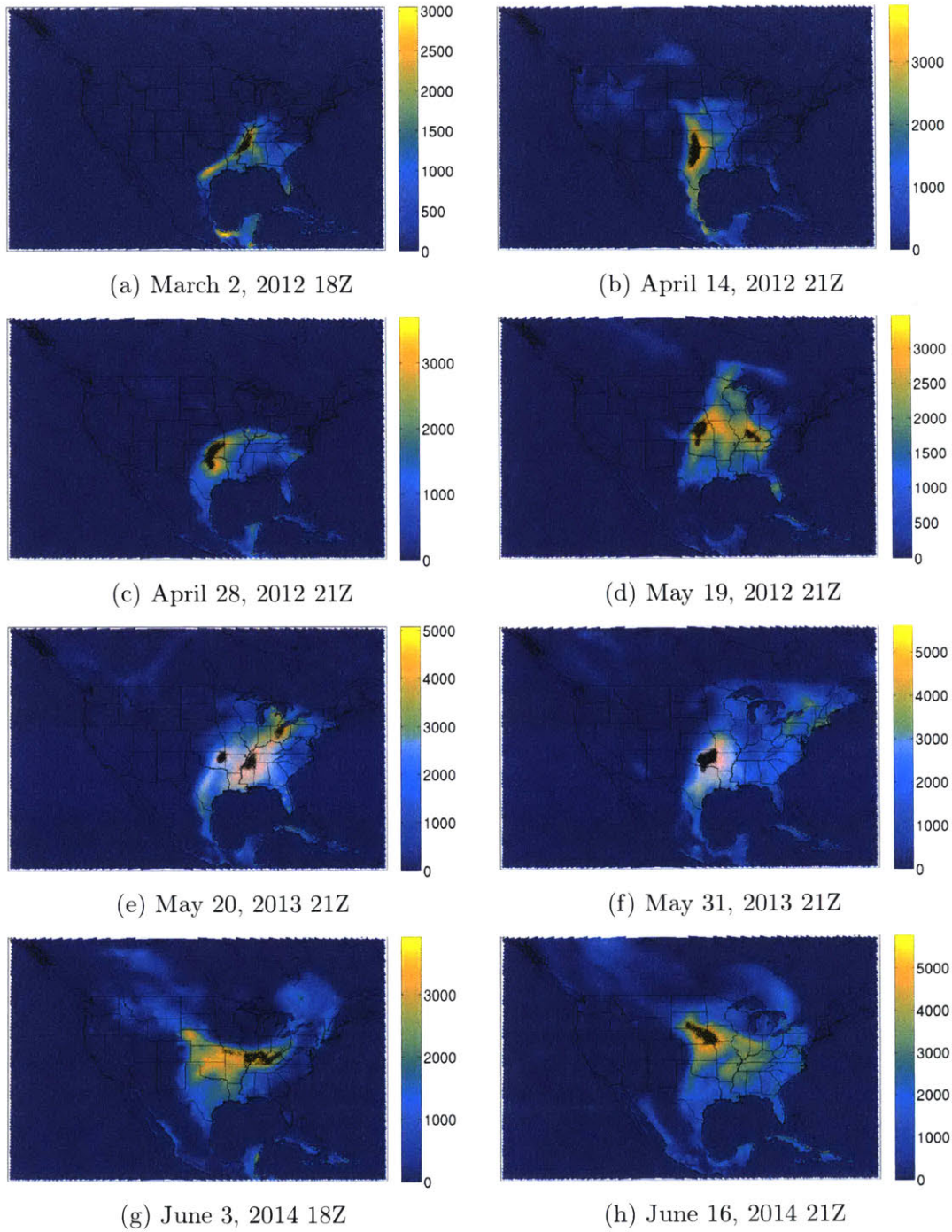
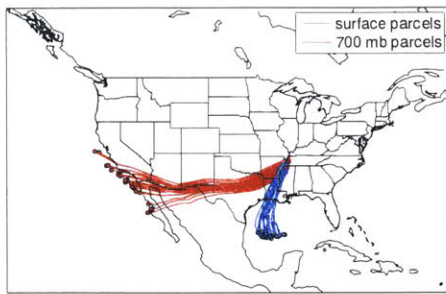
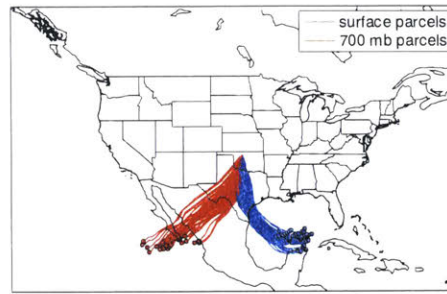


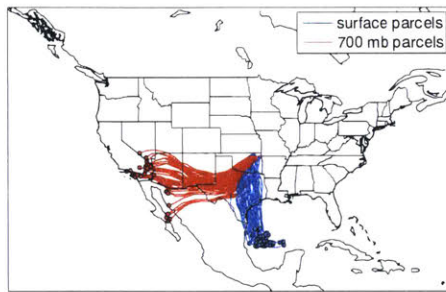
Figure 2-2: CAPE (J kg^{-1}) at the reanalysis time step immediately preceding the onset convection in each case. The hatched areas indicate the locations of the 99.9th percentile of CAPE values. Oceanic grid cells are masked.



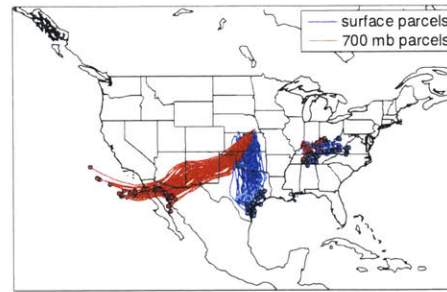
(a) March 2, 2012 18Z



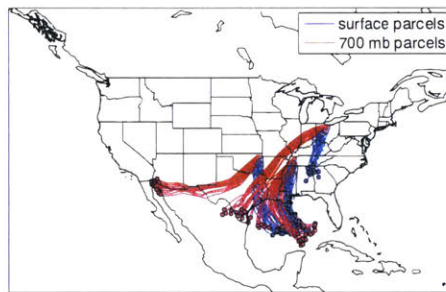
(b) April 14, 2012 21Z



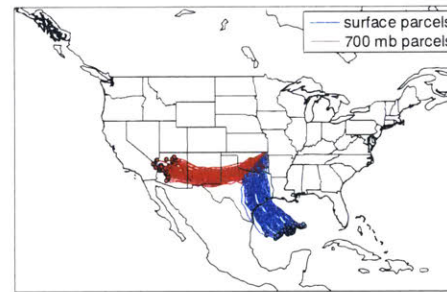
(c) April 28, 2012 21Z



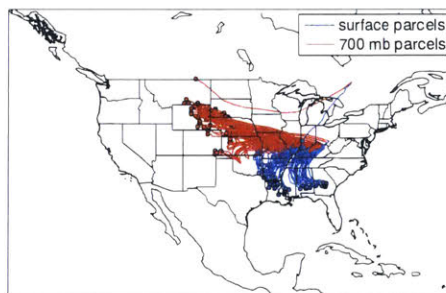
(d) May 19, 2012 21Z



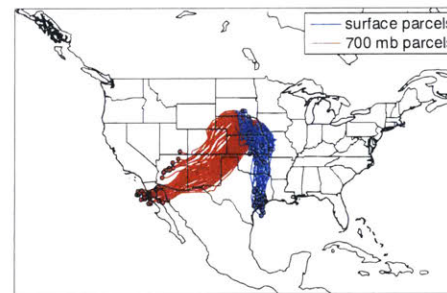
(e) May 20, 2013 21Z



(f) May 31, 2013 21Z



(g) June 3, 2014 18Z



(h) June 16, 2014 21Z

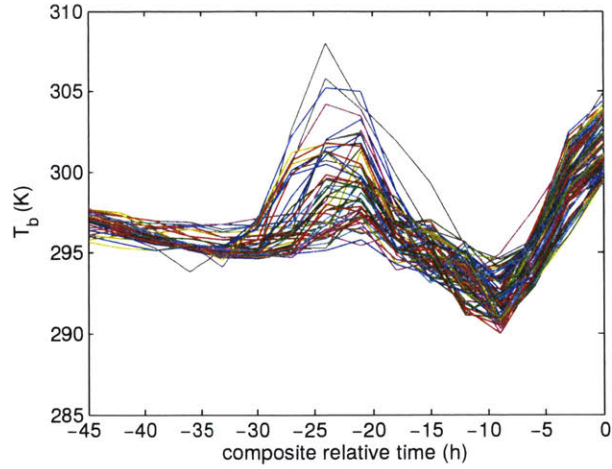
Figure 2-3: Paths of boundary layer parcels of interest (blue) tracked backward in time for the 2 days before the composite time. Red lines indicate the paths of parcels that end up superimposed on the parcels of interest at the 700 hPa level at the composite time. Circles indicate the initial positions of each parcel at 00Z the day prior to the day of the composite.

ally, the backward trajectories for parcels that end at the 700 hPa level at $t = 0$ are shown, as an illustration of the source of the elevated inhibitive capping layer. In all cases, the primary origin of the elevated inhibitive layer is indeed the Southwestern desert or the relatively dry high plains (in case (g)). These elevated dry parcels are advected eastward (and sometimes northward) to the region of interest, where they are superposed over the boundary layer parcels to be lifted. This result demonstrates the importance of the hot, dry elevated inhibitive layer in allowing extreme transient CAPE to be generated.

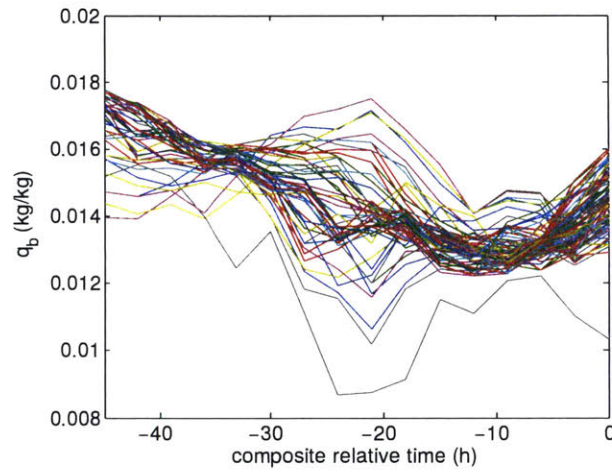
The remainder of this study will focus on the backward trajectories of the near-surface boundary layer parcels (shown in blue in Figure 2-3). In several cases, the boundary layer parcels from the composite-time high-CAPE columns originate over the Gulf of Mexico, as hypothesized. However, cases (d), (e), (g), and (h) each include some fraction of the boundary layer parcels whose origin is over land. The water vapor contained in these parcels at the composite time is therefore not directly from the Gulf of Mexico.

Figure 2-4 shows an example of properties of a group of boundary layer parcels along their backward trajectories. The parcels begin over the Gulf of Mexico (as shown in Figure 2-3c), so their initial temperature and humidity are relatively constant with time. As they move over land, the diurnal cycle becomes more apparent in the time series of these quantities. The time series of CAPE are more variable, but the calculated CAPE following each parcel exhibits a sharp increase in the last few hours leading up to the composite time. In fact, the majority of the CAPE buildup in this example is accomplished after $t = -9$ hours, with a corresponding increase in both T_b and q_b exhibited concurrently. The changes in T_b and q_b over this time frame each result in a total increase in boundary layer entropy of order 1000 J kg^{-1} .

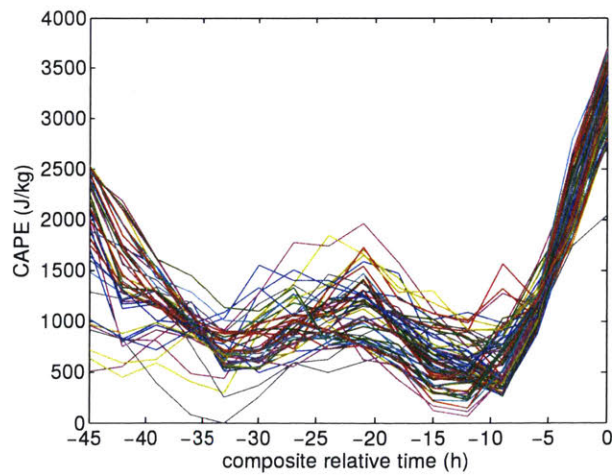
The results of the trajectory-following CAPE tendency budget calculation are shown in Figure 2-5. In this analysis, the individual terms of (2.1) are calculated using finite differences in the Lagrangian frame of the parcels to be lifted (the near-surface boundary layer parcels along whose backwards trajectories the budget is computed). The total CAPE tendency is simply the time rate of change of CAPE computed along



(a) temperature of boundary layer parcels

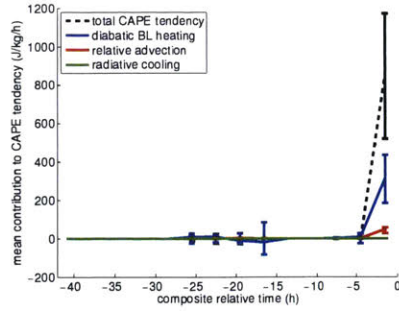


(b) specific humidity of boundary layer parcels

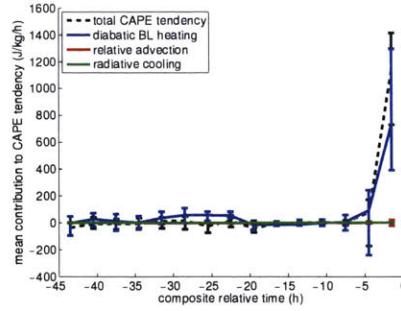


(c) CAPE in columns above boundary layer columns

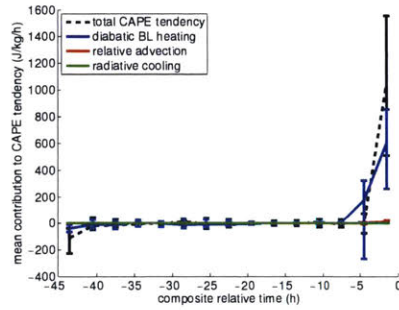
Figure 2-4: Properties of the group of boundary layer parcels of interest along their backward trajectories for the April 28, 2012 case.



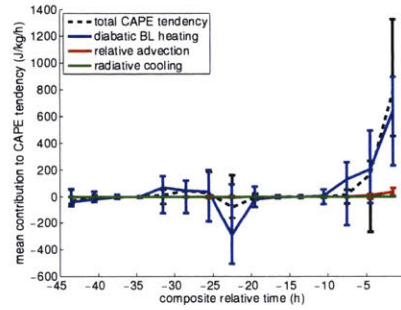
(a) March 2, 2012 18Z



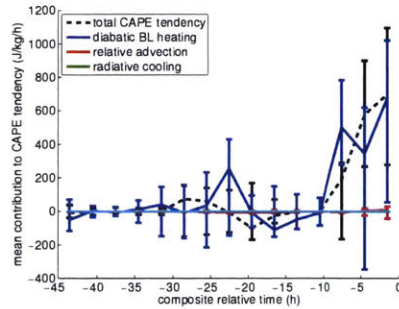
(b) April 14, 2012 21Z



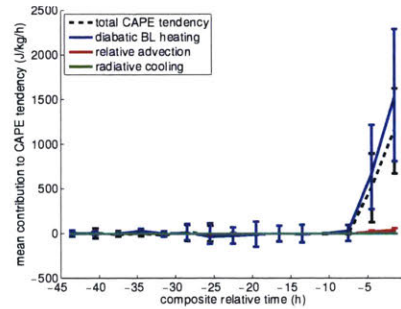
(c) April 28, 2012 21Z



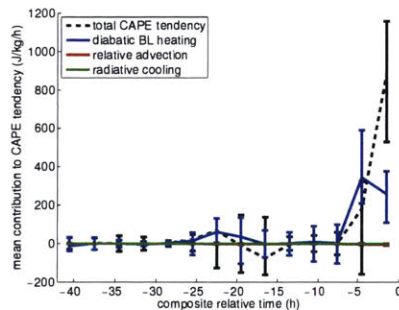
(d) May 19, 2012 21Z



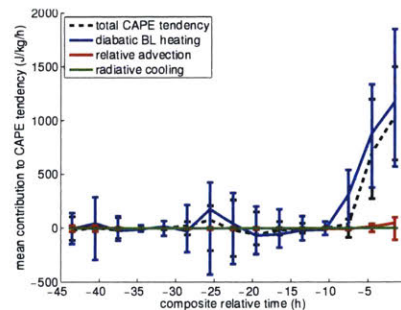
(e) May 20, 2013 21Z



(f) May 31, 2013 21Z



(g) June 3, 2014 18Z



(h) June 16, 2014 21Z

Figure 2-5: Time series of mean total CAPE tendency (dashed black line), and the contributions to CAPE tendency from diabatic heating (blue line), relative advection (red line), and radiative cooling (green line) for each case. The error bars represent the standard deviation spread of the individual parcels of interest.

the trajectory of each boundary layer parcel. The remaining three terms correspond to terms (i), (ii), and (iii) on the right-hand side of (2.1). The error bars on each line show the standard deviation spread of the individual parcels being tracked.

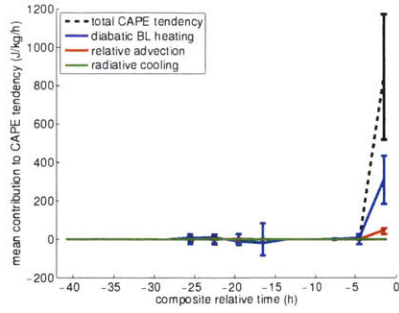
In theory, the diabatic boundary layer heating, relative advection, and radiative cooling terms should sum exactly to the total CAPE tendency at any given time along each trajectory. However, there is some residual error, due to the approximation of the total derivatives in (2.1) by finite differences, and potentially the internally inconsistent nature of reanalysis data.

As in the example shown in Figure 2-4c, the total CAPE tendency in each case exhibits a sharp increase within a few hours of $t = 0$. This indicates that the majority of the CAPE being built up toward its transient peak in the columns of interest is generated on the day of the event, rather than over multiple diurnal cycles.

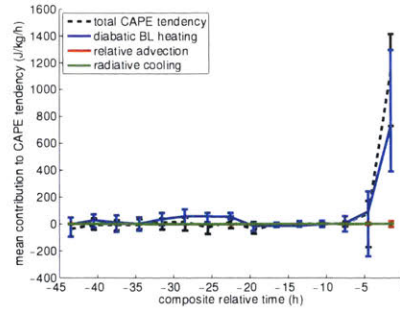
In each case, the increase in CAPE tendency toward the time of the composite is tracked closely by an increase in the component corresponding to the boundary layer entropy tendency. Since in a Lagrangian sense, the entropy of the boundary layer parcels is conserved in adiabatic motions, the contribution from this term is owed to diabatic heating of the surface boundary layer. This diabatic heating must occur primarily through the flux of heat and/or moisture from the land surface into the near-surface air parcels.

The magnitude of the boundary layer diabatic heating term is much greater than those of the terms corresponding to relative advection and radiative cooling in the free troposphere.

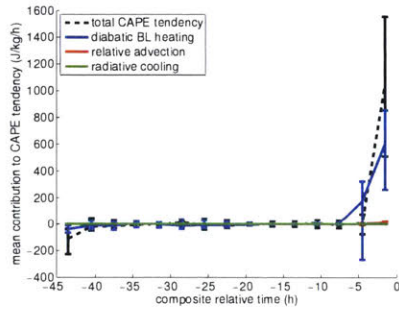
Finally, the contributions from each term and the total CAPE tendency are each integrated over time for each case. The resulting mean cumulative CAPE buildup attributable to each term is plotted in Figure 2-6. For each case, the contribution to mean accumulated CAPE from boundary layer diabatic heating is of the same magnitude as the overall total mean accumulated CAPE, and of a much larger magnitude than the other two contributing terms. Therefore, it can be concluded that the tendency of boundary layer entropy due to diabatic heating is the primary driver of CAPE buildup in each of the cases studied here.



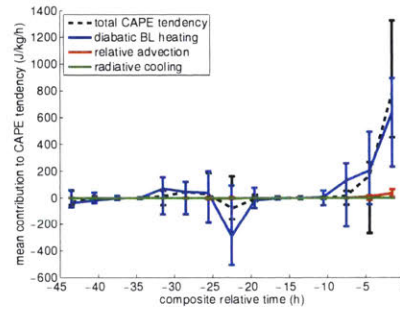
(a) March 2, 2012 18Z



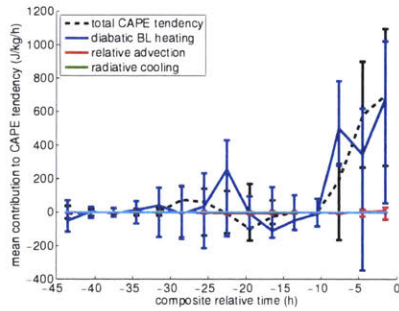
(b) April 14, 2012 21Z



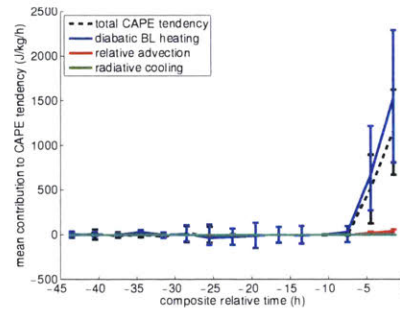
(c) April 28, 2012 21Z



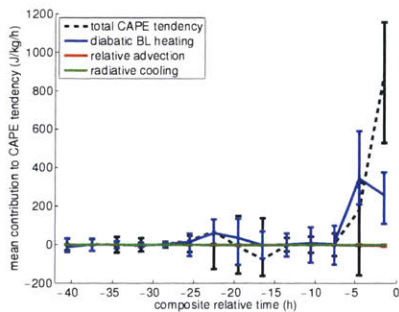
(d) May 19, 2012 21Z



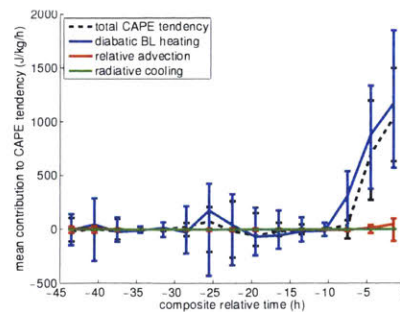
(e) May 20, 2013 21Z



(f) May 31, 2013 21Z



(g) June 3, 2014 18Z



(h) June 16, 2014 21Z

Figure 2-5: Time series of mean total CAPE tendency (dashed black line), and the contributions to CAPE tendency from diabatic heating (blue line), relative advection (red line), and radiative cooling (green line) for each case. The error bars represent the standard deviation spread of the individual parcels of interest.

the surface. Specifically, CAPE should increase after the sun rises and net radiative input to the land surface becomes positive, and is balanced by the flux of heat and moisture from the surface into the boundary layer. With an inhibitive cap in place, this allows CAPE to rise to an extreme transient peak, regardless of the origin of the low-level air mass.

It should be noted that although the relative advection pathway for generating CAPE is found to be relatively unimportant in these case studies, advective processes remain important for generating convective inhibition. In each case, the region of maximum CAPE coincided with an inhibitive cap of hot desert air that had been advected into place aloft. Without the inhibitive cap advected into place, diabatic heating of the boundary layer would cause convection to be triggered thermodynamically before significant CAPE could be achieved.

The importance of surface fluxes in determining the tendency of boundary layer entropy implies a climatological significance for properties of the land surface. For instance, the amount of moisture fluxed into the boundary layer by evapotranspiration in response to daytime heating can be dependent on the amount of available moisture in the soil. In the cases identified here, the contributions to boundary layer entropy tendency by the change in boundary layer humidity as a result of surface latent heat flux and the change in boundary layer temperature as a result of surface sensible heat flux are found to be of comparable magnitude. Therefore, the fluxes of both heat and moisture are important in controlling CAPE buildup. This suggests that a sufficiently moist land surface may be necessary to generate high transient peaks of CAPE in the presence of an inhibitive cap, and that a climatological modification of the Bowen ratio could have an effect on transient peak CAPE. Likewise, since the total entropy flux into the boundary layer from the surface is limited by the amount of net incoming radiation, surface albedo could have a role in modulating peak CAPE. In this sense, the Gulf of Mexico may influence the climatology of North American severe convection indirectly by dictating the climatological properties of the land surface in the central regions of the continent, rather than by directly supplying low-level entropy to convective environments. Future studies could attempt to identify

such relationships in observations and models of continental convective environments.

Chapter 3

Diagnosis of physical contributors to CAPE buildup in a simplified numerical framework

3.1 Introduction

The results of Chapter 2 show that in case studies of United States severe weather outbreaks, the buildup of CAPE prior to convective initiation is primarily accomplished by increases in the entropy of the surface boundary layer due to diabatic surface heating. In this chapter, we aim to demonstrate the same mechanism in a simple, idealized numerical model in which the problem is distilled to two dimensions.

If, as originally hypothesized, differential advection of moist air and steep lapse rates below and above the capping inversion layer (respectively) were the primary driver of CAPE generation over the continents, a three-dimensional framework would be required to reproduce the occurrence of transient extreme peak CAPE events in any model. However, the dominance of the boundary layer entropy tendency term in the CAPE tendency budget computation of reanalysis data implies that transient high CAPE can be achieved in a two-dimensional context, since high low-level entropy can be generated in situ via surface fluxes, rather than advected into place from an

external source. This work aims to demonstrate that in a single horizontal dimension, the land surface can be configured in such a way to create a capping inversion and allow high CAPE to be consistently generated in metastable vertical profiles in a particular location.

Properties of the land surface have been shown in past studies to play a role in modulating CAPE on long-term and short-term time scales. By altering the fluxes of heat and moisture to the planetary boundary layer, these properties affect the distribution of boundary layer entropy and can therefore influence levels of CAPE in the atmosphere (Pielke 2001). Although the boundary layer quasi-equilibrium hypothesis is not valid at short time scales in continental regions (Donner and Phillips 2003), the properties of the boundary layer are found to be the primary control of CAPE both in continental and tropical oceanic contexts (Donner and Phillips 2003; Ye et al. 1998). In particular, the surface soil moisture is found to be an important factor in modulating convection in observations (Taylor and Ellis 2006), climate models (Schär et al. 1999), and initial-value mesoscale simulations (Shaw et al. 1997).

Here, a simple numerical model is employed to examine the effects of spatial changes in surface moisture on the background state of CAPE. In this approach, it is important to construct a minimal model such that the relevant dynamical processes can be isolated in the absence of complicating ‘realistic’ (but extraneous) features. Therefore, a hydrostatic model is used to integrate the primitive equations on a two-dimensional grid with parameterized convection, clouds, and radiation. To preserve simplicity, the model is set up on a non-rotating x - z plane, with cloud-radiative interactions turned off. The land surface is represented by a very shallow ocean layer. This model is initially run in a two-column configuration before being expanded to a reentrant many-column channel. In each configuration, the model is allowed to run into a statistical (not necessarily steady) equilibrium, in which the state of CAPE is observed.

Another possible approach could have been to start with a realistic regional model of the Plains region, and establish a baseline of environmental CAPE that reproduces observations. One could then experiment by toggling environmental features such

as the surface soil moisture gradient, surface albedo gradient, surface topography, presence of the Gulf of Mexico or Rocky Mountains, or the strength or shear of the imposed background flow. By monitoring the response of the equilibrium CAPE in the system to these changes, one could hypothetically identify the environmental factors that are most important in supporting high values of CAPE in the Great Plains and contiguous regions. However, as it is not well understood how CAPE is produced in such models to begin with, the simplified framework approach is selected in order to get a better understanding of the dynamics at work. The minimal modeling approach creates a baseline dynamical framework onto which additional features such as rotation and three-dimensional physics could be added in future studies.

3.2 Methods

A multiple-column version of the single-column hydrostatic model of Emanuel and Živković-Rothman (1999) is used. This model includes the parameterized convection scheme detailed in that study, as well as the fractional cloud scheme of Bony and Emanuel (2001), and the radiative transfer scheme of Morcrette (1991). The surface is represented by an ocean with a mixed layer of fixed depth. Land surfaces are simply represented by an ocean with a very shallow (20 cm) mixed layer, representing the relatively low heat capacity of land. This ‘ocean’ has no circulation, and heat is not allowed to be diffused or advected between columns via subsurface processes. The model numerically integrates the hydrostatic equations for streamfunction and vorticity over the two-dimensional domain, with lateral advection allowed between model columns.

The model is set up with a region of low surface moisture on the western half of the domain, and a region of high surface moisture on the eastern half. This configuration is analogous to that of North America, where there is a zonal gradient in surface moisture between the dry desert southwest and the moister Plains and Midwest regions to the east.

The system is simplified as much as possible in order to eliminate extraneous

physical mechanisms and feedbacks that might obfuscate the dynamics of interest. To that end, the model is set up zonally at a latitude of 0, with the effect of removing rotation from the system. This is fully equivalent to running the two-dimensional model in a non-rotating system. Additionally, the radiative transfer scheme is utilized such that shortwave and longwave radiation do not interact with clouds in the model (clouds are allowed to form where air is saturated, but they are transparent to all radiation). This is done to eliminate cloud-radiative feedback mechanisms that would otherwise complicate the equilibrium state of the system. Furthermore, the longitude of each column is set to a constant value of 0, in order to eliminate differential timing of the diurnal cycle (columns in the east receiving incoming shortwave prior to those in the west). This does not remove the zonal dimensionality or relative locations of the model columns; it simply ensures that incoming shortwave radiation varies uniformly with time over the domain.

Radiation, surface temperature, and water vapor content are all calculated interactively, rather than specified in the model. The model is run with a reduced solar constant to compensate for the lack of poleward heat transport by the ocean in the two-dimensional model. The value of the reduced solar constant is calculated in proportion to the surface albedo, with a baseline value of 1161.0 W m^{-2} for a surface albedo of 0.20.

The model is run with 46 vertical levels, and random noise is added to the initial soundings to introduce slight variations between the columns. The model is initially run in a two-column configuration for the purpose of conducting sensitivity experiments. Later, this is expanded to a 40-column configuration, for which a more detailed analysis of the production of CAPE is conducted. In each case, the model is run in one experiment with a diurnal cycle of radiation, as well as an experiment in which incoming solar radiation is set to a diurnally-averaged constant.

In the model, changes in surface moisture are imposed by modulating a parameter called evaporative fraction (α). α is defined as a nondimensional coefficient whose value is between 0 and 1, and acts as a multiplicative factor to the latent heat exchange between the surface and the planetary boundary layer. It is therefore defined such

that the total surface entropy flux is given by

$$F_s = C_D |\mathbf{V}| [L_v(\alpha)(q_0^* - q_b) + c_p(\theta_0 - \theta_b)], \quad (3.1)$$

where C_D is a nondimensional drag coefficient, L_v is the latent heat of vaporization of water, c_p is the heat capacity of dry air, $|\mathbf{V}|$ is the magnitude of the surface wind, q and q^* are specific humidity and saturation specific humidity, respectively, θ is potential temperature, and the subscripts $_o$ and $_b$ correspond to the surface and boundary layer, respectively. Physically, the evaporative fraction corresponds to a measure of the moisture of the land surface. In the notation of the boundary layer equilibrium model of Betts (2000), the quantity defined here as evaporative fraction can be written as

$$\alpha = \frac{g_v}{g_v + g_a}, \quad (3.2)$$

where g_a is an aerodynamic conductance dependent on the surface wind speed, and g_v is a vegetative conductance whose value is the reciprocal of the “vegetative resistance” (R_v) that modifies the availability of water for evaporation at the surface. Although the system being studied here is not necessarily considered to be in boundary layer quasi-equilibrium, this parameterization is still relevant, as the value of R_v is observed to be low for wet soils and high for dry soils (Betts 2000). Therefore, specifying α can be considered a way of specifying the moisture content of the modeled soil, since $\alpha = 0$ in the limit in which $R_v \rightarrow \infty$, and $\alpha = 1$ in the limit in which $R_v \rightarrow 0$.

In the many-column configuration, contributions to the equilibrium CAPE state are analyzed using (3.5). By diagnosing the four terms on the right-hand side of this equation in a parcel-following sense, the relative contributions to equilibrium CAPE from surface entropy, radiative cooling, and vertical and horizontal advection are determined.

3.2.1 Sensitivity experiments

To investigate the effects of surface properties on the production of CAPE in the model, sensitivity experiments are first performed in a two-column framework. In this setup, two adjacent land columns of 500 km width each are specified identically with the exception of their surface properties in a domain with rigid lateral boundaries. First, while fixing the evaporative fraction of the easternmost column surface at 1.0, the α of the western column surface is varied from 1.0 to 0.10 in increments of 0.1. For each value of α in the western column, the model is run forward in time from its initial state until its time-dependent fields reach a statistical equilibrium. The model is considered to be in statistical equilibrium once the trends of its time-dependent fields go to zero over a sufficiently long time (100 days). This procedure is repeated for the cases of diurnally averaged and diurnally varying radiation.

From the model output fields, equilibrium mean values of surface temperature, streamfunction, precipitation, and CAPE are calculated for each column using data from the last 100 days of each simulation. Here, CAPE is calculated considering a parcel lifted from the surface boundary layer in each column, according to (1.1), with parcels lifted from the level of the surface boundary layer. For the purposes of this calculation, the boundary layer lifting level is simply taken to be the lowest level of the model. For the diurnal run, the mean daily maximum of these quantities is calculated for each column.

Next, resetting the evaporative fraction to 1.0 in both columns, a sensitivity experiment is performed using surface albedo. The surface albedo is fixed at its default value of 0.20 in the easternmost column, while the surface albedo of the western column is altered in increments of 0.10 over the range of values from 0.10 to 0.90. To compensate for the loss of energy by the system due to increased surface albedo (or the decrease in energy due to decreased albedo), the solar constant for each run is adjusted over the entire domain according to

$$S = S_0 \frac{1 - a_0}{1 - \frac{1}{2}(a_0 + a)}, \quad (3.3)$$

where $S_0 = 1161.0 \text{ W m}^{-2}$, $a_0 = 0.20$, and a is the surface albedo of the column for which that quantity is being adjusted. For each value of surface albedo, the model is run to statistical equilibrium as in the evaporative fraction experiment. Once again, these runs are conducted both with and without the diurnal cycle of radiation. Upon conclusion of each model run, mean values of surface temperature, streamfunction, precipitation and CAPE are calculated for each column in the equilibrium state.

3.2.2 Many-column configuration

For a more detailed examination of the dynamical processes supporting CAPE in these statistical equilibrium states, the experiment is extended to a framework in which there are 40 columns in a laterally periodic domain. These columns compose four regions, as shown in Fig. 3-1: Counting from the left (west) of the domain, columns 1-10 and 31-40 are ocean columns, with surface evaporative fraction of 1.0, and mixed layer depth of 50 m. Columns 11-20 are land columns with $\alpha = 0.1$, and columns 21-30 are land columns with $\alpha = 1.0$. The columns have otherwise identical parameters, with widths of 500 km each. Therefore, the domain contains 10 columns of ‘dry’ land immediately adjacent to 10 columns of ‘wet’ land, surrounded on either side by 10 columns of ocean in a nonrotating reentrant channel.

This simplified minimal model domain may be considered analogous to the continental United States, in which the dry land of the desert Southwest is adjacent to the relatively moist land of the Midwest and Southeast, with oceans on either side, and a climatological mean westerly background wind. The Great Plains, in which severe local storms are climatologically most prevalent, are situated on the boundary of the dry land and wet land regions.

A background zonal flow is imposed throughout the domain. This flow is westerly (from left to right in the domain; all columns still have constant latitude), with

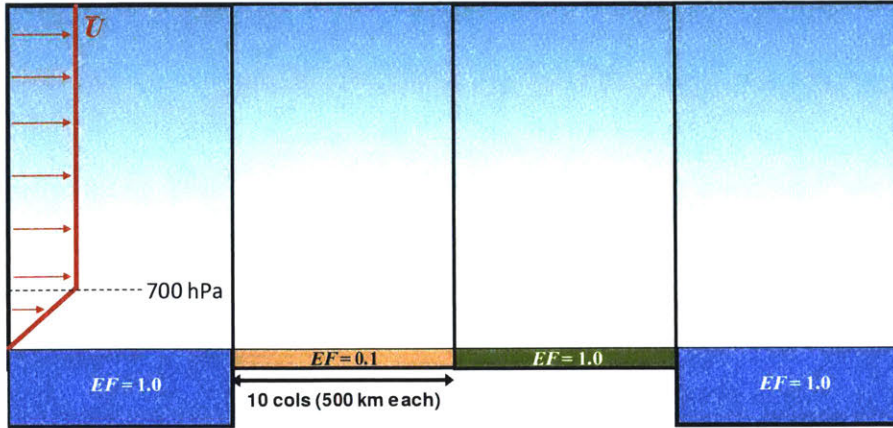


Figure 3-1: Schematic of the many-column configuration of the idealized numerical model. Each rectangle represents a region 10 columns in width, with a fixed evaporative fraction and oceanic mixed-layer depth. The red lines illustrate the prescribed background wind profile, which applies throughout the domain. Atmospheric advection between columns and regions is permitted, with a periodic reentry between the left and right edges of the domain. The depth of the bottom section of each section corresponds to the depth of its ocean surface, and therefore its effective heat capacity.

vertical shear at low levels, according to

$$U(z) = \begin{cases} U_0 & p \leq 700 \text{ hPa} \\ U_0 \left[\frac{p_{sfc} - p}{p_{sfc} - (700 \text{ hPa})} \right] & p > 700 \text{ hPa} \end{cases}, \quad (3.4)$$

where $U_0 = 20 \text{ m s}^{-1}$, and $p_{sfc} = 1012.5 \text{ hPa}$. The purpose of the low-level shear is to allow air from the dry land portion of the domain to be advected above boundary layer air from the moist land. This superposition of relatively warm air above relatively cool air may create a temperature inversion that would contribute to metastability of the column to moist convection. Given the background zonal flow, the purpose of the deep ocean columns on either side of the land is to provide a large region of high-heat capacity surface with relatively constant temperature that will damp perturbations being advected away from the moist land, and prevent them from feeding back onto the dry land in the reentrant flow (which is now required in order to conserve energy, due to the imposition of the background flow).

In this configuration, the model is run forward in time until a statistical equilib-

rium is reached. Separate runs are conducted with diurnally averaged and diurnally varying radiation. From the model output, 100-day equilibrium means of surface temperature, streamfunction, precipitation, CAPE, and CIN are calculated. Since the model is run to a state of statistical equilibrium, each of these quantities can be calculated for each hour of the day to create a composite of their mean daily evolution for the experiments with diurnally varying radiation. CAPE is again calculated as in (1.1), while CIN is calculated according to (1.3). Since the equilibrium state is a statistical equilibrium, and not a steady state, each of the output variables fluctuates in time. Therefore, for CAPE and CIN, cumulative frequency diagrams are produced tallying the number of output time steps in which the quantities fall into given ranges in each column during 1000 days of statistical equilibrium in the model.

For the cases in which a diurnal cycle has been implemented in the model, composite plots are created in which the values of output quantities including surface temperature, zonal surface wind, precipitation, CAPE, and CIN at each hour in the solar day are averaged over 100 days of statistical equilibrium in the model. The resulting composites show the mean daily evolution of each quantity in each column with the diurnal cycle.

Finally, for the diurnally varying model runs for which time-dependent composites have been created, tendency budgets of CAPE are constructed following (2.1). In the context of this model, the CAPE tendency budget equation becomes

$$\frac{d}{dt}CAPE \approx (T_b - T_L) \frac{ds_b}{dt} - \int_{p_L}^{p_b} \left[\frac{R_d \dot{Q}}{c_p} \left(\frac{T_v}{T} \right) - \frac{R_d T_v}{\theta} \left(u_r \frac{\partial \theta}{\partial x} + \omega \frac{\partial \theta}{\partial p} \right) \right] d \ln p, \quad (3.5)$$

where $u_r = u - u_b$ is the zonal velocity relative to that of a parcel in the planetary boundary layer, total derivatives are decomposed according to

$$\frac{d}{dt} = \frac{\partial}{\partial t} + u \frac{\partial}{\partial x}, \quad (3.6)$$

and the partial derivatives are approximated by finite differences. For the purposes

of this calculation, the boundary layer is taken to be first model level above the surface. Each individual component of the right-hand side of (3.5) is calculated for each column in the model output, including

- (i) $(T_b - T_L) \frac{\partial s_b}{\partial \tau}$, the component due to changes in the entropy of the subcloud layer,
- (ii) $\int_{p_L}^{p_b} \frac{R_d \dot{Q}}{c_p} \left(\frac{T_v}{T} \right) dp$, the component due to radiative cooling of the environment,
- (iii) $\int_{p_L}^{p_b} \frac{R_d T_v}{p\theta} u_r \left(\frac{\partial \theta}{\partial x} \right) dp$, the component due to environmental lateral advection,
and
- (iv) $\int_{p_L}^{p_b} \frac{R_d T_v}{p\theta} \omega \left(\frac{\partial \theta}{\partial p} \right) dp$, the component due to environmental vertical advection.

Their sums are compared to the calculated CAPE tendencies in those respective columns. For the case of diurnally varying radiation, CAPE budgets can be calculated for the mean equilibrium quantities for each hour of the day, thereby creating a daily mean equilibrium composite for each term in the budget.

3.3 Results

3.3.1 Sensitivity experiments

Evaporative fraction

The results of the first sensitivity experiment in which surface evaporative fraction is varied for one of two columns are shown in Fig. 3-2. In this experiment, incoming solar radiation is set to a diurnally-averaged constant. Fig. 3-2a shows the mean equilibrium surface temperature of each column, while Fig. 3-2b shows the mean equilibrium precipitation rate in each column, Fig. 3-2c shows the mean equilibrium level of CAPE, and Fig. 3-2d shows the mean vertical velocity at the 850 mb level. In this case, the ‘dry’ column is that in which the value of surface evaporative fraction is being modulated, since the evaporative fraction of the ‘wet’ column surface is set to the constant value of 1.0. With increasing α in the ‘dry’ column, each output variable approaches its value from the control case, in which $\alpha = 1.0$ in both columns.

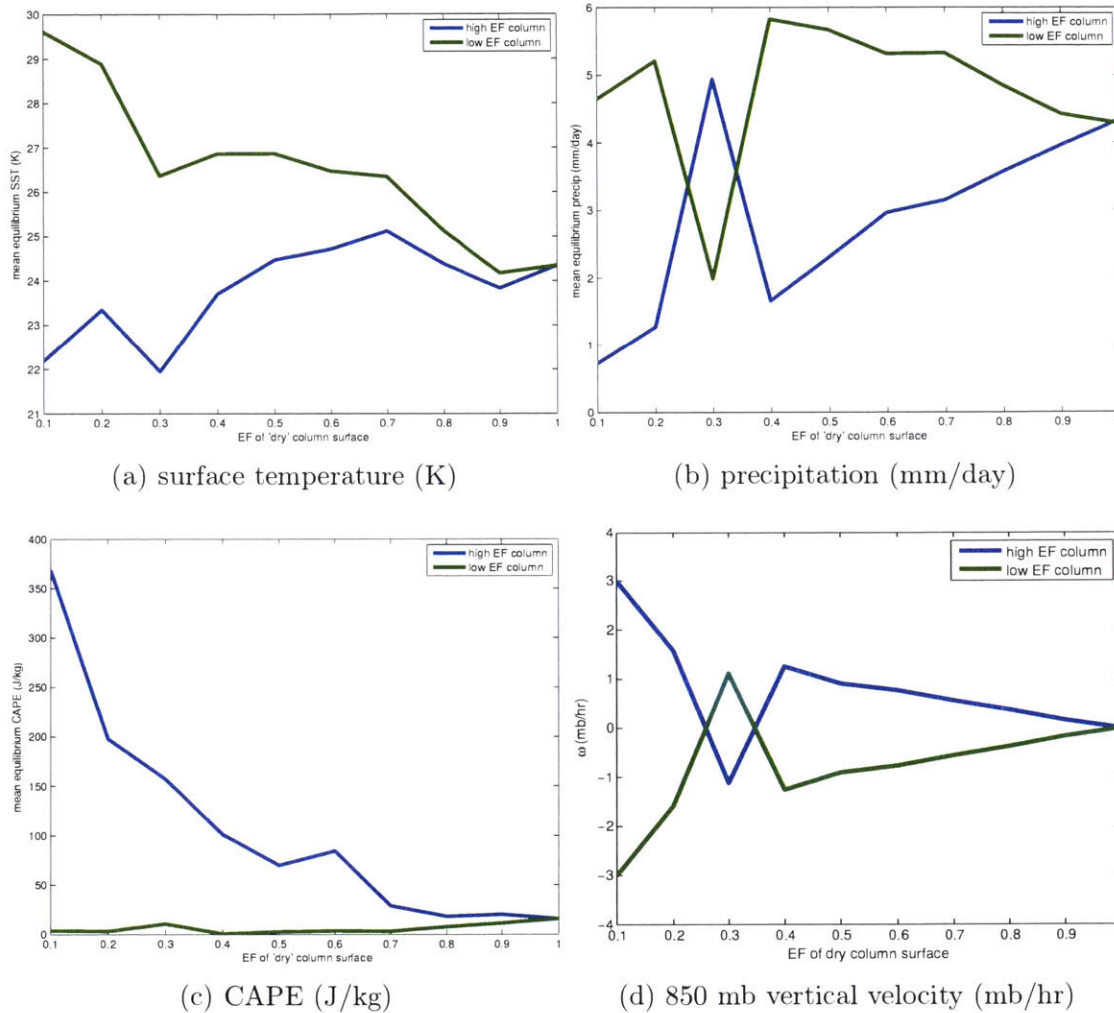


Figure 3-2: Mean equilibrium values of surface temperature (a), precipitation (b), CAPE (c), and vertical velocity at the 850 mb level (d) versus surface evaporative fraction of the low- α column in the ‘dry’ column (green) and the ‘wet’ column (blue) for the case with diurnally averaged radiation.

The differential in surface α has the effect of creating a circulation in the 2-column model, as can be inferred from the vertical velocities shown in Fig. 3-2d. For all cases except for $\alpha = 0.3$, this circulation exists such that there is subsidence over the cooler ‘wet’ column and rising motion over the warmer ‘dry’ column. This circulation is associated with increased precipitation over the ‘dry’ column.

As shown in Fig. 3-2a, decreasing α has the effect of warming the surface in the ‘dry’ column, and therefore an increased difference in surface evaporative fraction creates an increased difference in surface temperature.

Finally, the total CAPE in the system appears to be a monotonically increasing function of the difference in surface evaporative fraction, with maximum mean equilibrium CAPE values of around 350 J kg^{-1} in the ‘wet’ column for $\alpha = 0.1$ in the ‘dry’ column. In all cases, there is no appreciable buildup of CAPE observed in the ‘dry’ column.

This experiment indicates that in a mean statistical equilibrium sense, large gradients in surface evaporative fraction correspond to larger background levels of CAPE.

Fig. 3-3 shows the results of the two-column evaporative fraction sensitivity experiment in which radiation is allowed to vary with the diurnal cycle. As in Fig. 3-2, the four panels show the surface temperature, precipitation rate, CAPE, and 850 mb vertical velocity, respectively, for each column. However, Fig. 3-3 shows the mean equilibrium daily maximum for each quantity.

A similar circulation to that of the constant insolation case is shown the develop when radiation is allowed to vary diurnally. Over the low- evaporative fraction surface, less surface energy flux is partitioned to evaporation, allowing for anomalous warming. This warming creates a warmer surface temperature, which is then associated with rising motion over the ‘dry’ column and subsidence over the ‘wet’ column. More precipitation is thereby observed in the ‘dry’ column than in the ‘wet’ column for all values of α .

Finally, the CAPE in this experiment is not a monotonic function of α difference. As shown in Fig. 3-3c, the maximum daily CAPE value occurs in the ‘wet’ column for the lowest values of α in the ‘dry’ column, while above some a value of $\alpha \approx 0.4$

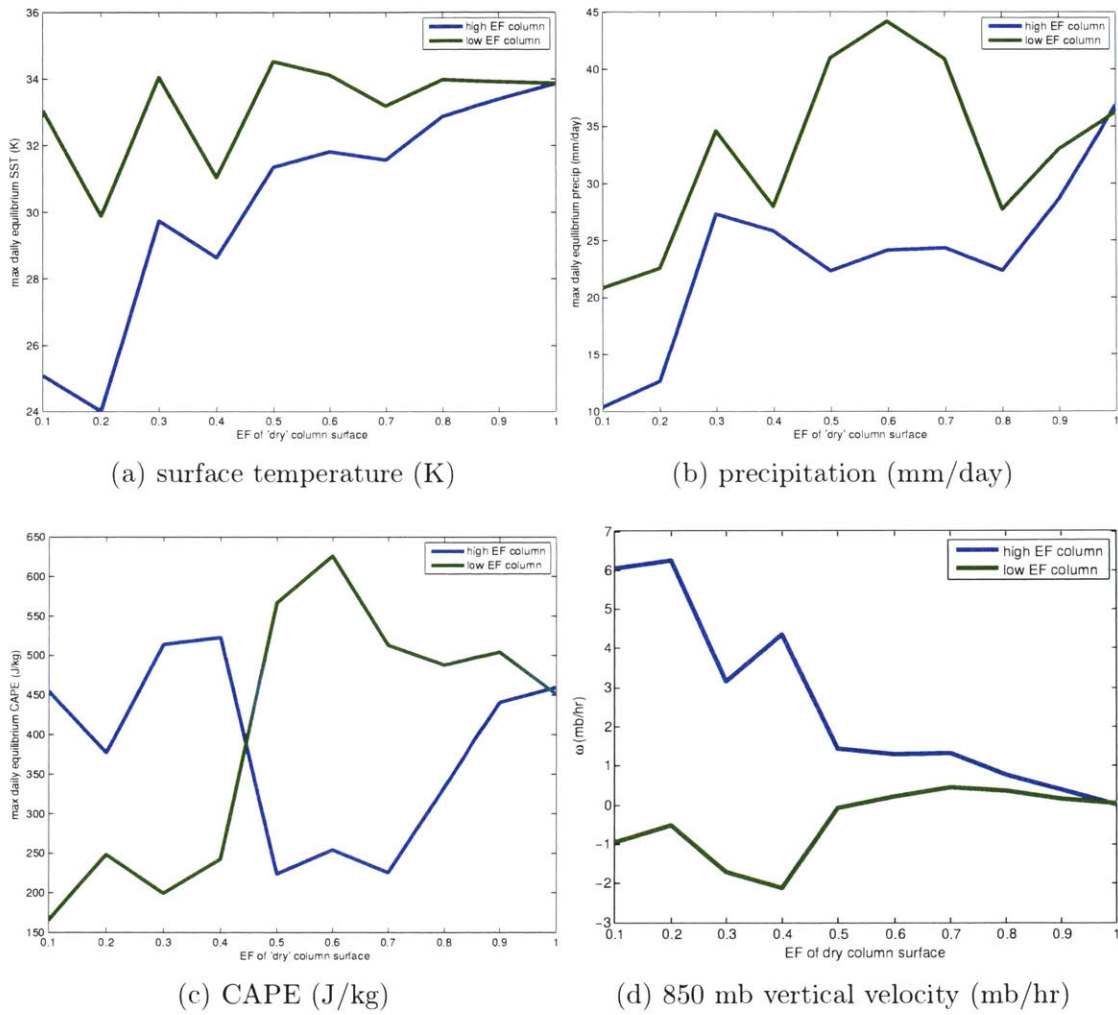


Figure 3-3: Mean daily maximum equilibrium values of surface temperature (a), precipitation (b), CAPE (c), and vertical velocity at the 850 mb level (d) versus surface evaporative fraction of the low evaporative fraction column in the 'dry' column (green) and the 'wet' column (blue) for the case with diurnally varying radiation.

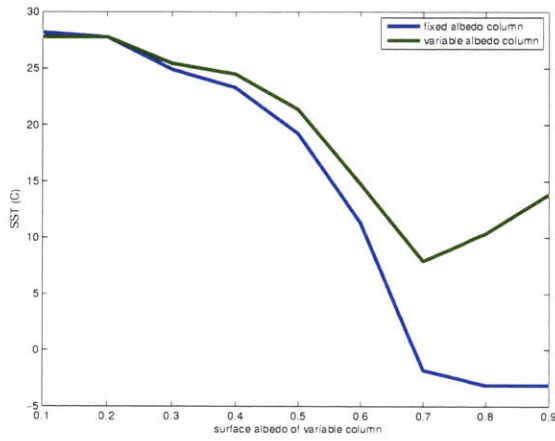
to 0.5, the maximum daily CAPE value occurs in the ‘dry’ column. In this regime, the maximum mean daily CAPE in the ‘dry’ column is maximized for $\alpha = 0.6$. In all cases (including the control case), the mean equilibrium daily maximum of CAPE is significantly higher than the mean equilibrium CAPE levels observed in the nondiurnal experiment (Fig. 3-2c). This is an indication of the relative importance of the transient nature of CAPE, since the higher values calculated from diurnal cycle maxima are not reflected in the mean overall background state.

Surface albedo

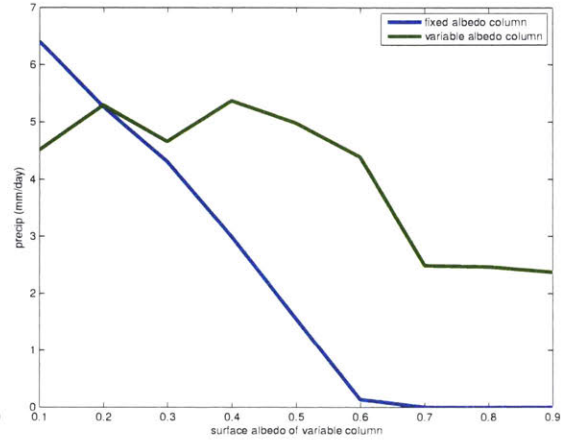
Fig. 3-4 shows the results of the sensitivity experiment with diurnally averaged radiation in which the surface albedo of one of the two columns is modified while that of the other column is fixed at $a_0 = 0.20$, with a constant evaporative fraction of $\alpha = 1.0$ in both columns. Fig. 3-4a shows the mean equilibrium surface temperature of each column against the surface albedo of the column in which surface albedo is being modulated. Likewise, Fig. 3-4b shows the mean equilibrium precipitation rate in each column for each run, Fig. 3-4c shows the mean CAPE level in each column, and Fig. 3-4d shows the mean vertical velocity at the 850 mb level in each column. In this case, the control run is that for which $a = 0.2$ in the variable albedo column.

The results of the albedo sensitivity experiment in which incoming solar radiation is specified as a function of the diurnal cycle are shown in Fig. 3-5. Here, Fig. 3-5a shows the mean daily high surface temperature over 100 days of the equilibrium period of the model runs plotted against the albedo of the column for which albedo is being modulated. Fig. 3-5b shows the equilibrium mean daily maximum precipitation rate, Fig. 3-5c shows the same thing for CAPE, and Fig. 3-5d shows the same for 850 mb vertical velocity.

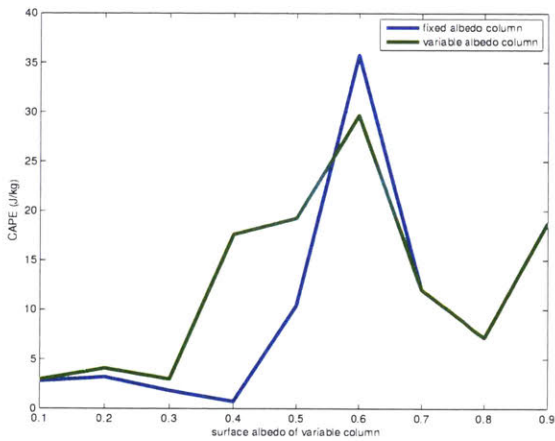
In both of these experiments, the circulation is reversed from those seen when varying surface evaporative fraction. As shown in Figs. 3-4d and 3-5d, air subsides over the variable albedo column (where a is higher), and rises over the column in which albedo is fixed over $a = 0.2$. This is a rather curious result, as the higher albedo column is counterintuitively found to have a warmer surface temperature.



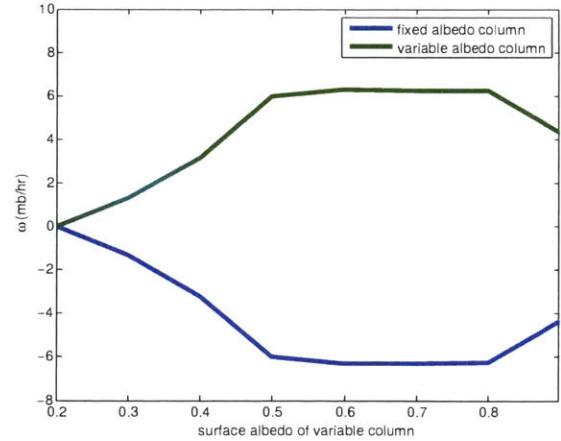
(a) surface temperature (K)



(b) precipitation (mm/day)



(c) CAPE (J/kg)



(d) 850 mb vertical velocity (mb/hr)

Figure 3-4: Mean equilibrium values of surface temperature (a), precipitation (b), CAPE (c), and vertical velocity at the 850 mb level (d) versus surface albedo of the varying albedo column in the column in which albedo is being modulated (green) and column in which it is held constant (blue) in the domain for the case with diurnally averaged radiation.

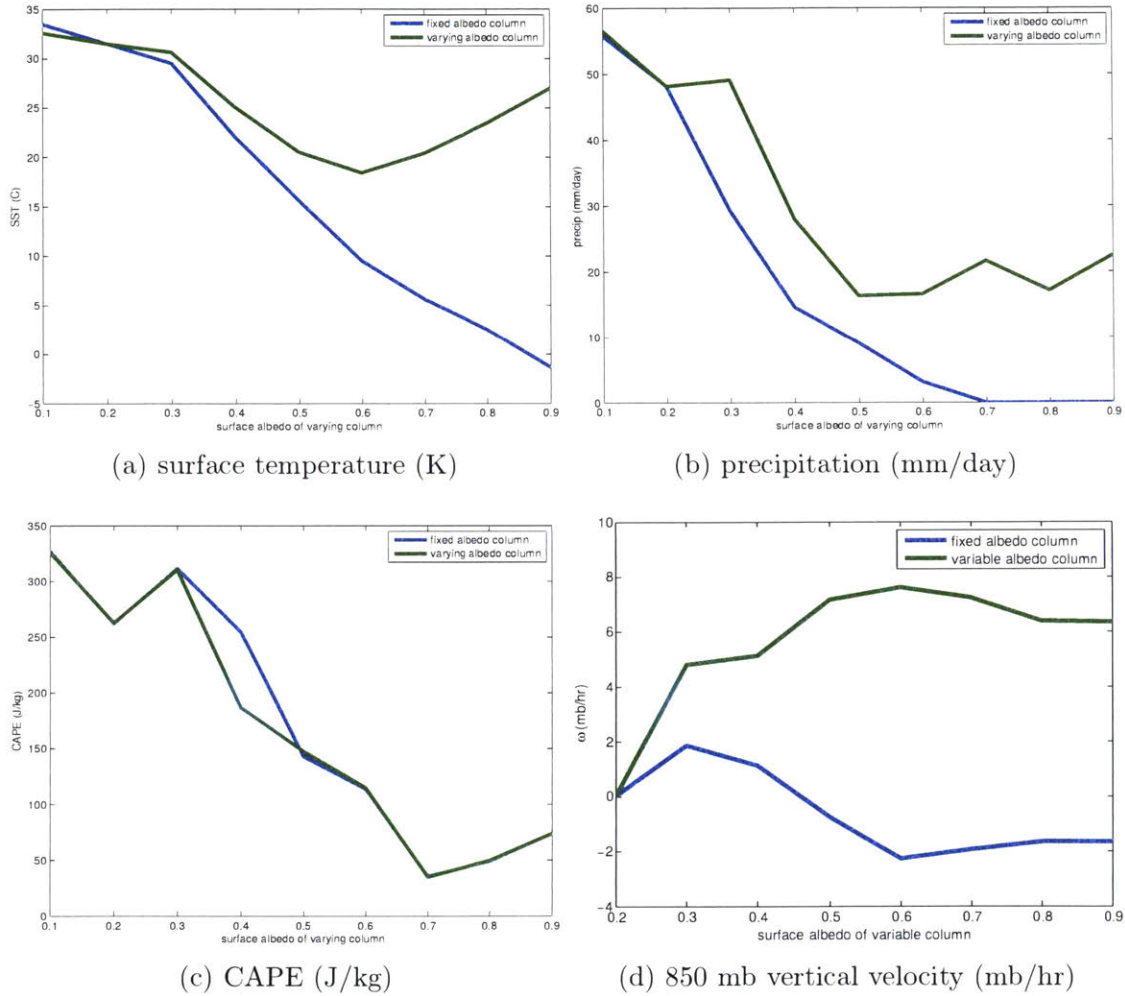


Figure 3-5: Mean daily maximum equilibrium values of surface temperature (a), precipitation (b), CAPE (c), and vertical velocity at the 850 mb level (d) versus surface albedo of the varying albedo column in the column in which albedo is being modulated (green) and column in which it is held constant (blue) for the case with diurnally varying radiation.

Fig.s 3-4a and 3-5a show the surface temperature decreasing across the domain with increasing albedo in both the diurnal and nondiurnal experiments. This effect is observed even though the solar constant is increased to compensate for increased albedo according to (3.3). Therefore, the surface albedo parameter may be involved in a feedback on surface temperature and the overall system. Precipitation rate is also found to decrease with increasing albedo, with precipitation rates generally lower in the column with lower albedo, as shown in Fig.s 3-4b and 3-5b. These results are consistent with the aforementioned ‘reverse’ circulation, whose origin remains unknown.

For the case of diurnally varying radiation, the maximum value of CAPE in each column generally decreases with increasing albedo in the column for which albedo is being modulated. This correlation is not observed in the experiment in which incoming solar radiation does not vary diurnally. However, in this case, the observed mean equilibrium CAPE levels are very low ($< 50 \text{ J kg}^{-1}$) due to the lack of capping inversion, and are therefore not very meaningful in this model. Therefore, in this configuration, it can be concluded that varying the surface albedo of one of the two columns does not significantly favorably contribute to the mean background state of CAPE.

3.3.2 40-column configuration

Diurnally averaged radiation

In Fig. 3-6, the number of model output time steps in 1000 days of statistical equilibrium in which CAPE falls into given ranges of values are tallied in each column. The resulting diagram is a heat map showing the relative frequency (as a nondimensional fraction; the sum of the frequencies in each column is 1) of each CAPE level in each column in the non-steady statistical equilibrium state for the 40-column configuration with diurnally averaged radiation. In this diagram, the 11 westernmost columns and 11 easternmost columns (including 1 boundary column on either side of the domain) constitute the deep ocean part of the domain. The 10 columns in the left center of

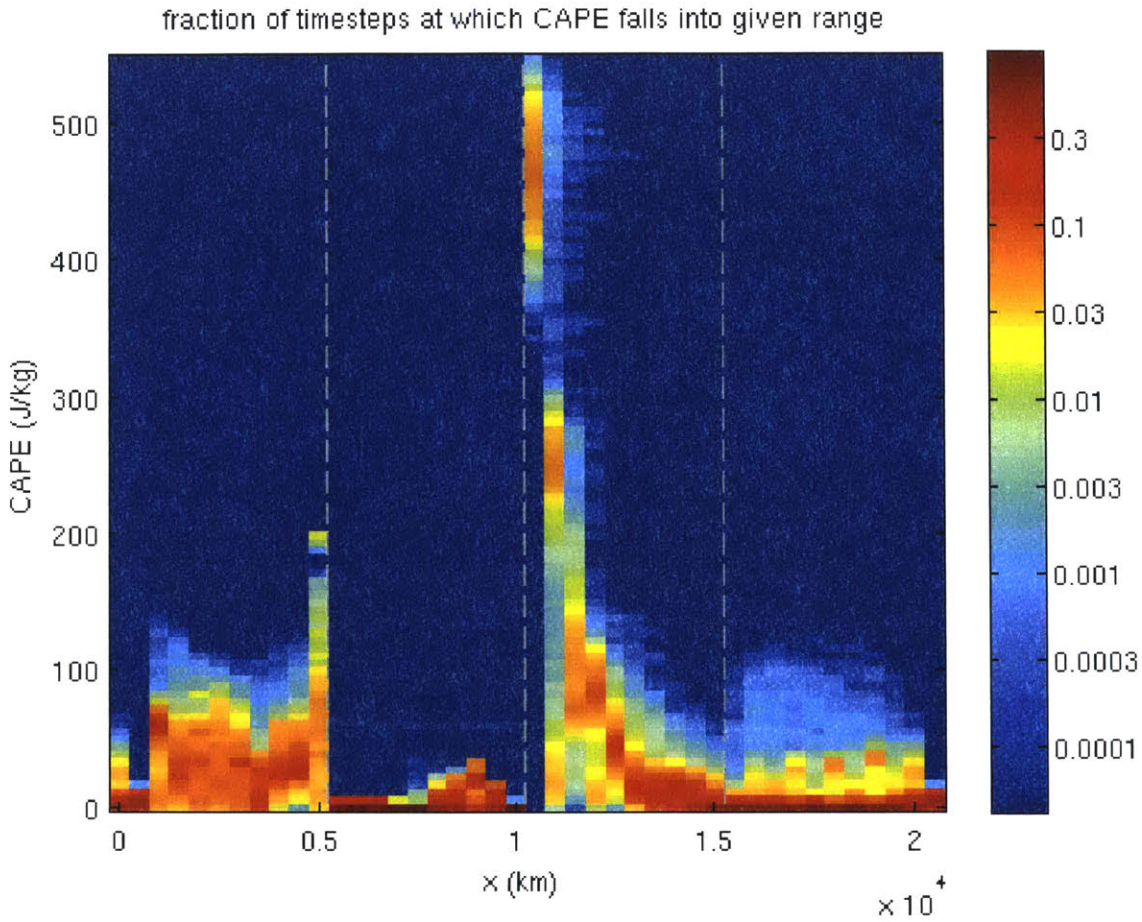


Figure 3-6: Heat map diagram showing the number of timesteps (shading) in equilibrium at which the CAPE falls into a given range of values (J/kg, vertical axis) in each model column (horizontal axis) for the case of diurnally averaged radiation. The vertical dashed lines indicate the boundaries between the ocean, ‘dry’ land, and ‘wet’ land regions.

the domain constitute the ‘dry’ land, for which $\alpha = 0.1$. The remaining 10 columns (in the right center of the domain) are the ‘wet’ land, for which $\alpha = 1.0$.

From Fig. 3-6, it is clear that the highest values of CAPE occur in the westernmost column of the wet land region. This is the column that is contiguous with the dry land region. In this column, modeled CAPE levels are most often above 350 J kg^{-1} . CAPE in the adjoining columns in the wet region is highly variable, but generally appears to decrease with distance from the dry land region. Conversely, in the dry land region, CAPE values are very low, only rarely exceeding 50 J kg^{-1} . Over the ocean columns, CAPE is more highly variable, but is most frequently observed at the

lowest levels.

Although levels of CAPE in this simulation are not consistent with those that would climatologically be associated with severe convection on Earth (Rasmussen and Blanchard 1998; Grams et al. 2012), the pattern of CAPE distribution in this result indicates a significant influence of surface properties on the background state of CAPE in this configuration. This is likely due to the use of a time-invariant constant solar input at the surface, rather than a diurnal cycle in which the peak surface heating would be much higher. However, since CAPE in the westernmost column in the wet land region is categorically higher than that of the other columns, it can be concluded that a discontinuous jump in surface evaporative fraction is sufficient to produce an elevated level of CAPE in the presence of a given background flow in this model configuration.

Fig. 3-7 is the same plot as Fig. 3-6, with the exception that occurrences of CIN are tallied instead of those of CAPE. The CIN heat map shows that values of CIN in the leftmost column of the wet land region are frequently around 100 J kg^{-1} , although lower values are also observed with lesser frequency in this column. In the columns immediately to the east of this column, CIN levels are much lower, with values most frequently around 25 J kg^{-1} . However, with increasing proximity to the eastern ocean region, the equilibrium CIN distribution becomes increasingly variable, with CIN values in the rightmost column of the wet land region occasionally exceeding the maximum values in the leftmost column of that region. This high variability is continued into the ocean region, while in the dry land region, variability is much lower.

The relatively high levels of CIN in the leftmost column of the wet land region, in association with the relatively high CAPE values in the same column indicate the possibility of climatological conditional instability in this column. As shown in Appendix A, the mean states of dynamic quantities in the model output demonstrate that this conditional instability is the result of an anomalous warm layer that is created above the dry land section and advected downstream by the background shear flow, providing a capping layer in at least one of the westernmost wet land

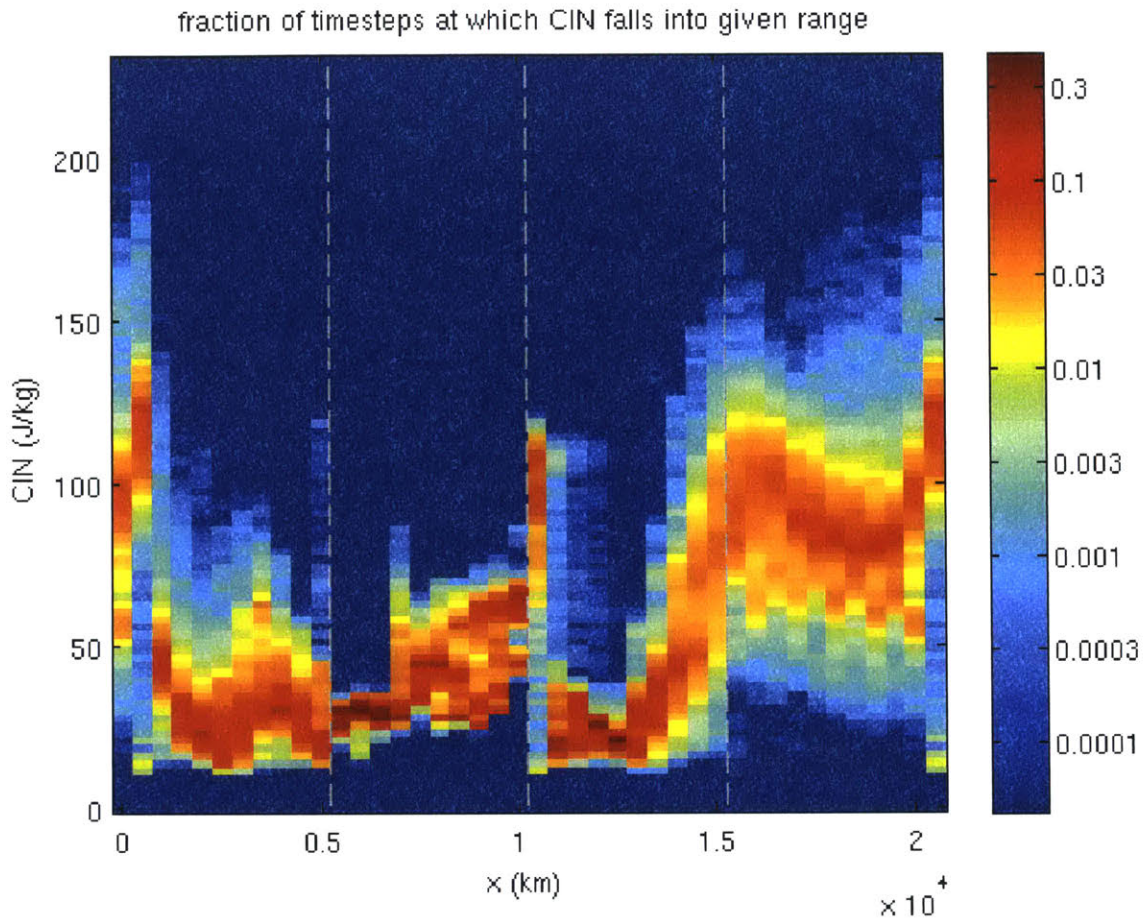


Figure 3-7: Heat map diagram showing the number of timesteps (shading) in equilibrium at which the CIN falls into a given range of values (J/kg, vertical axis) in each model column (horizontal axis) for the case of diurnally averaged radiation. The vertical dashed lines indicate the boundaries between the ocean, ‘dry’ land, and ‘wet’ land regions.

columns.

Diurnally varying radiation

Fig. 3-8 shows a statistical equilibrium heat map of CAPE as in Fig. 3-6, but for the case of diurnally varying radiation. However, for this figure, instead of tallying the occurrences of CAPE at all time steps, the maximum values of CAPE in each 24-hour period are found. The resulting figure tallies the number of days in which the maximum value of CAPE falls into a given range for each column. In this figure, the variability of maximum daily equilibrium CAPE is much lower than that of equi-

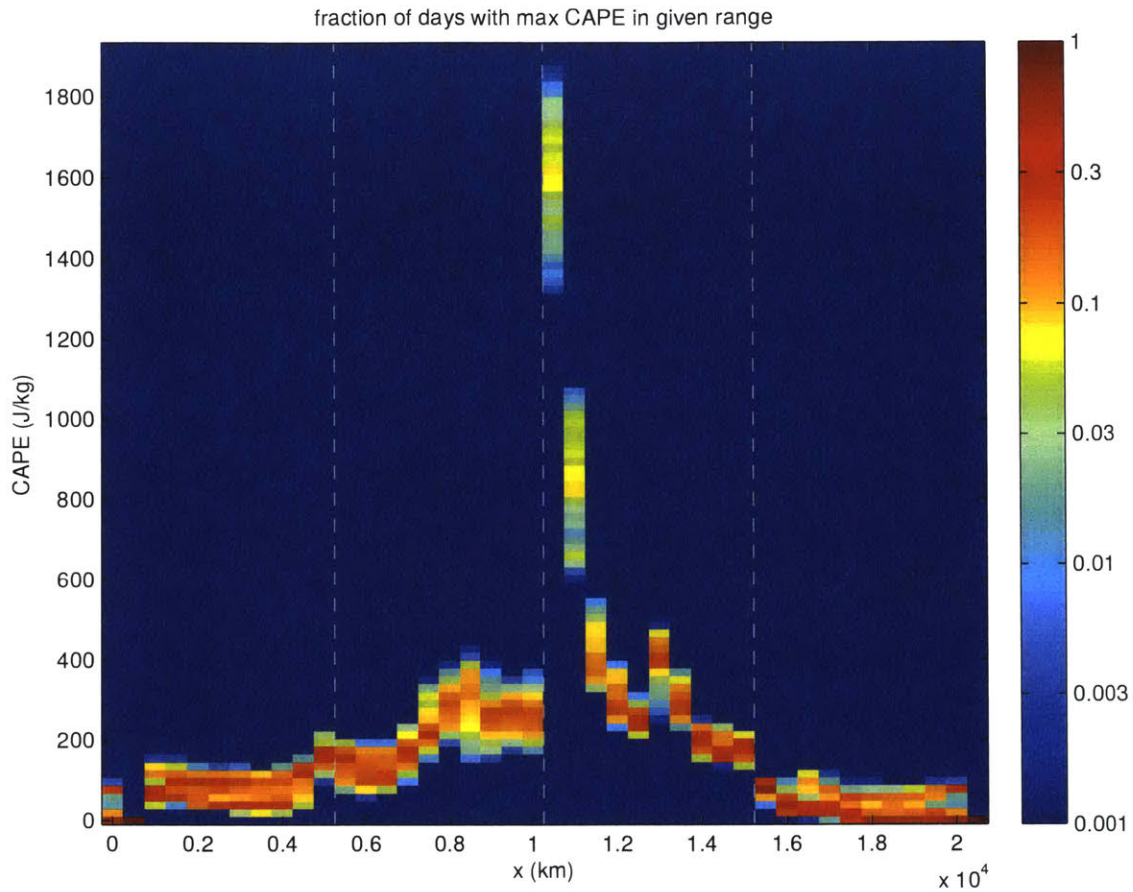


Figure 3-8: Heat map diagram showing the number of days (shading) in equilibrium at which the maximum value of CAPE falls into a given range of values (J/kg , vertical axis) in each model column (horizontal axis) for the case of diurnally varying radiation. The vertical dashed lines indicate the boundaries between the ocean, ‘dry’ land, and ‘wet’ land regions.

librium CAPE in the nondiurnal experiment (while the values themselves are much higher). While some variability remains, the maximum daily CAPE for each column falls into a discrete range of values. The highest of these ranges is again found on the western edge of the wet land region, where maximum daily CAPE values are most frequently between 1400 and 1800 J kg^{-1} . The second highest range of CAPE is found in the adjoining wet land column, where CAPE is most frequently between 600 and 1000 J kg^{-1} . CAPE values continue to decay to the east approaching the ocean columns, in which CAPE is always below 200 J kg^{-1} . CAPE values in the dry land columns are slightly higher than those over the ocean, but they by and large remain

below 400 J kg^{-1} .

This result reinforces that of the nondiurnal 40-column experiment, showing that a gradient in surface evaporative fraction can lead to climatologically large values of CAPE. The highest values of CAPE in this run are found in the same column as those in the nondiurnal run. Furthermore, the relatively small variation in this result indicates that the diurnal cycle is the leading timescale for modulating the transience of CAPE in this configuration, as CAPE reaches roughly the same maximum levels each day. Furthermore, the maximum values of CAPE are consistent with those that might be sufficient to produce severe storms in the real atmosphere.

Fig. 3-9 is the same as Fig. 3-8, with the exception that maximum daily occurrences of CIN are tallied instead of those of CAPE. The equilibrium distribution of maximum daily CIN values is slightly more variable than that of those of CAPE. However, daily CIN maxima still fall into discrete ranges for each column. The highest of these ranges is found on the western edge of the wet land region, where maximum daily CIN values are most frequently between 140 and 230 J kg^{-1} . The adjacent wet land column has maximum daily CIN values between 90 and 150 J kg^{-1} , while CIN maxima in the rest of the wet land region are always between 40 and 75 J kg^{-1} . Daily CIN maxima in the dry land region are of comparable magnitude, while those over the ocean are more highly variable.

Once again, the highest values of CIN fall in the same column as those of CAPE, indicating that the configuration of surface evaporative fraction and background shear flow creates the possibility of conditional instability in this column.

Fig. 3-10 contains hourly composites of surface variables, showing their mean evolutions with the diurnal cycle in the equilibrium state. Fig. 3-10a shows a diurnal composite of surface temperature across the domain, while Fig. 3-10b shows a composite of precipitation, and Fig. 3-10c shows the same thing for surface zonal wind. In these plots, the horizontal axis is x in the domain, while the vertical axis is time in the diurnal cycle, and the mean values of each quantity are indicated by shading. Therefore, these plots are akin to mean diurnal Hovmöller diagrams for each quantity.

Fig. 3-10a shows that the dry land surface is consistently warmer than that of the

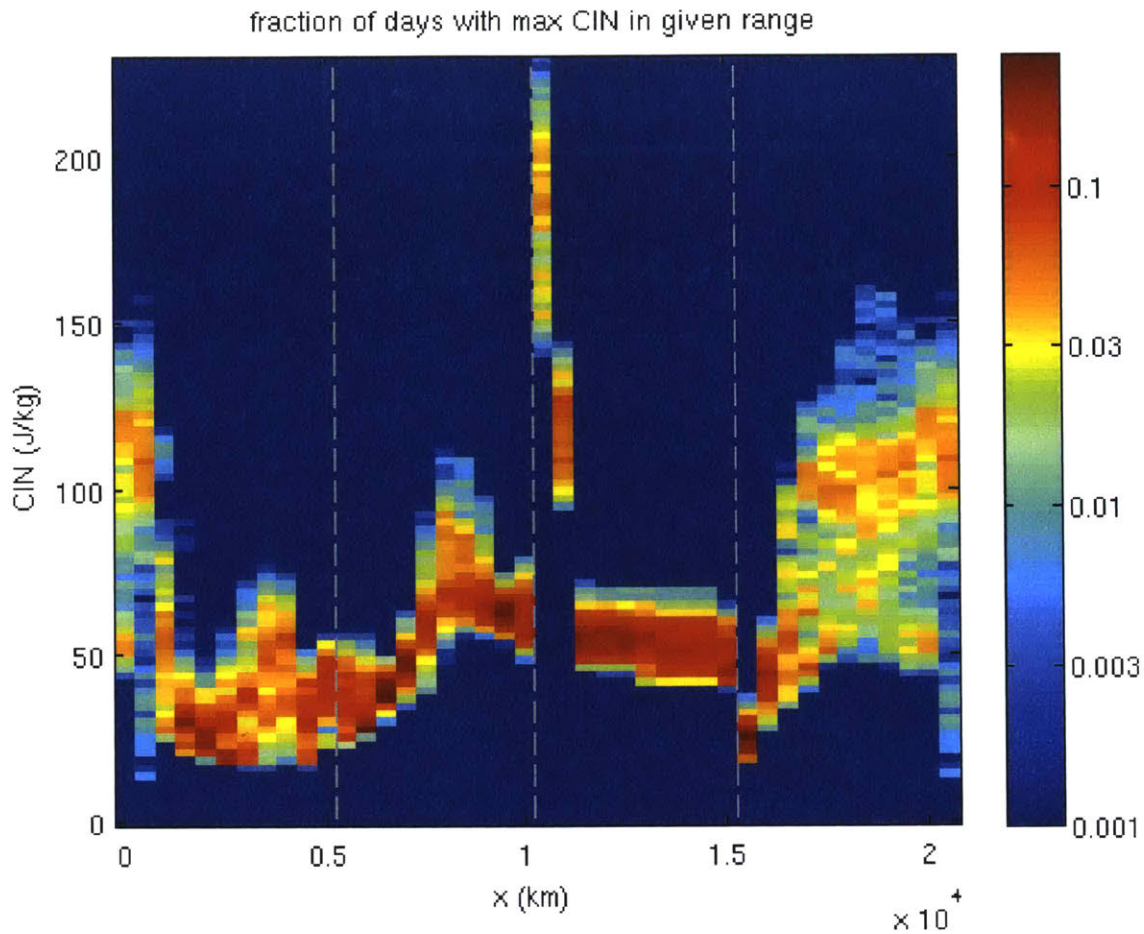
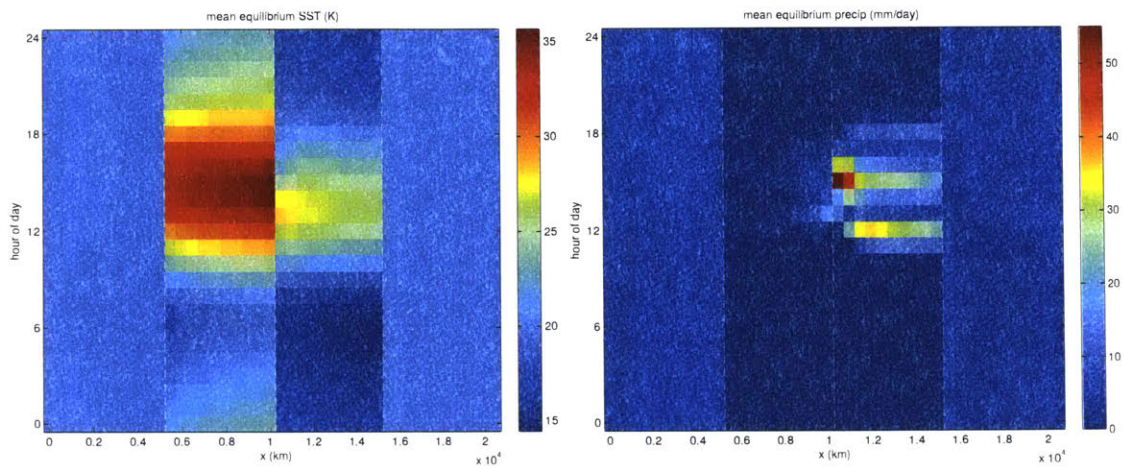


Figure 3-9: Heat map diagram showing the number of days (shading) in equilibrium at which the maximum value of CIN falls into a given range of values (J/kg, vertical axis) in each model column (horizontal axis) for the case of diurnally varying radiation. The vertical dashed lines indicate the boundaries between the ocean, ‘dry’ land, and ‘wet’ land regions.

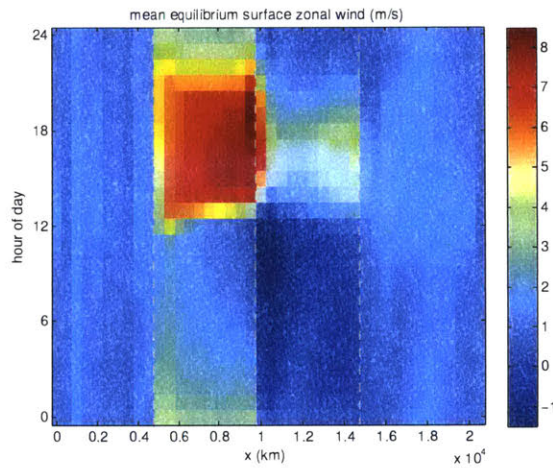
wet land, while the magnitude of the diurnal cycle of ocean surface temperature is negligible. Furthermore, the maximum of wet land surface temperature occurs earlier in the day than that of dry land surface temperature. This is likely due to cooling associated with the precipitation that occurs in the wet land columns around 15 hours local time, as shown in Fig. 3-10b. This maximum of precipitation corresponds to a convective release of the CAPE built up around 13 hours local time, as shown in Fig. 3-11.

Fig. 3-10c shows a maximum of westerly surface wind in the dry land columns in the afternoon. Flow in the wet land columns also becomes westerly at this time after



(a) surface temperature (K)

(b) precipitation (mm/day)



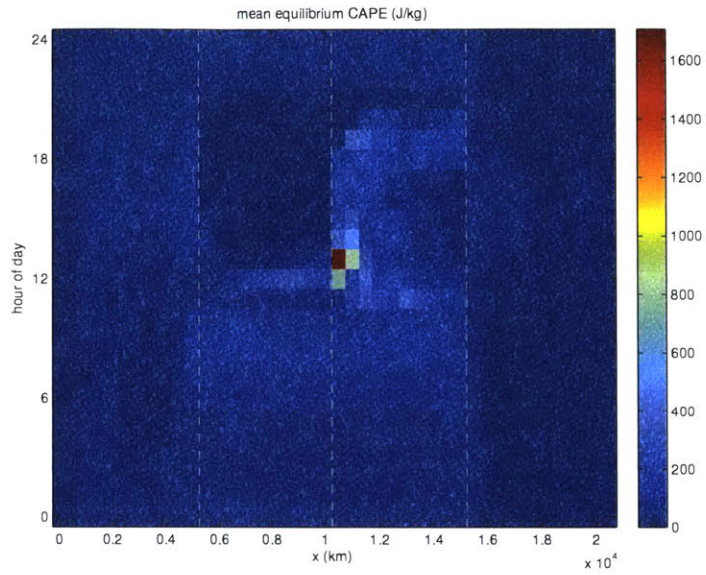
(c) surface zonal wind (m s^{-1})

Figure 3-10: Composites of hourly equilibrium means in surface temperature (a), precipitation (b), and zonal wind (c) for the case in which a diurnal cycle of radiation is used. The vertical dashed lines indicate the boundaries between the ocean, 'dry' land, and 'wet' land regions.

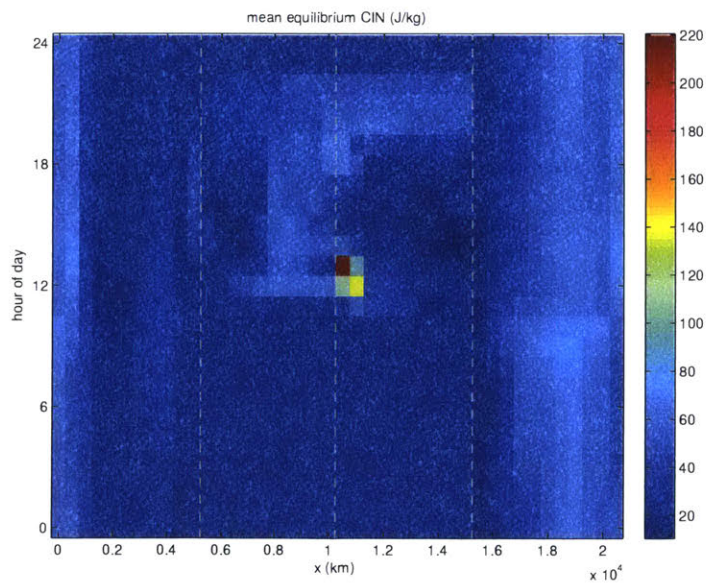
having been easterly in the morning near the boundary with the dry land. The cause of this sudden reversal of surface flow is not immediately clear, although its onset is contemporaneous with the daily precipitation event in the wet land columns. The flow reversal also corresponds to strong convergence at the dry/wet land boundary during the afternoon; this acts to support further precipitation after the initial triggering of convection.

Fig. 3-11 shows similar diurnal composites for CAPE and CIN. Both CAPE and CIN show pronounced maxima in the wet land column closest to the dry land at 13 hours local time. At this time, the mean CAPE in this column is 1700 J kg^{-1} , while the mean CIN is 220 J kg^{-1} . A model-generated sounding of the mean atmosphere in this column at this time is shown in Fig. 3-12. This sounding indicates a low-level temperature inversion, with warm, dry air in place just above the surface layer, which itself is nearly saturated. This inversion persists up to roughly the 850 hPa level, above which a parcel lifted from the boundary layer would be positively buoyant up to about the tropopause. This low-level temperature inversion is a consequence of advection of warm, dry air from the dry land region by the background shear flow across the boundary to the wet land region above the surface layer. While advection of warm, dry air is also responsible for creating capping inversions in real continental atmospheres, the lack of terrain height differences in this model causes the inversion to occur much closer to the surface, increasing the transience of the modeled CAPE extreme.

CAPE tendency budget analysis Fig. 3-13 shows the mean hourly values of each of the four terms on the right-hand side of (3.5). These plots use the same composite Hovmöller format as those in Figs 3-10 and 3-11. Fig. 3-13a shows the contribution to the tendency of CAPE following a boundary layer fluid parcel due to changes in boundary layer entropy, Fig. 3-13b shows the contribution to CAPE tendency due to radiational cooling, Fig. 3-13c shows the contribution due to horizontal advection, and Fig. 3-13d shows the contribution due to vertical advection. Note that the color scales are not the same for each image, as data in Fig. 3-13a are of order $10^{-1} \text{ J kg}^{-1}$



(a) CAPE (J/kg)



(b) CIN (J/kg)

Figure 3-11: As in 3-10, but for CAPE (a) and CIN (b).

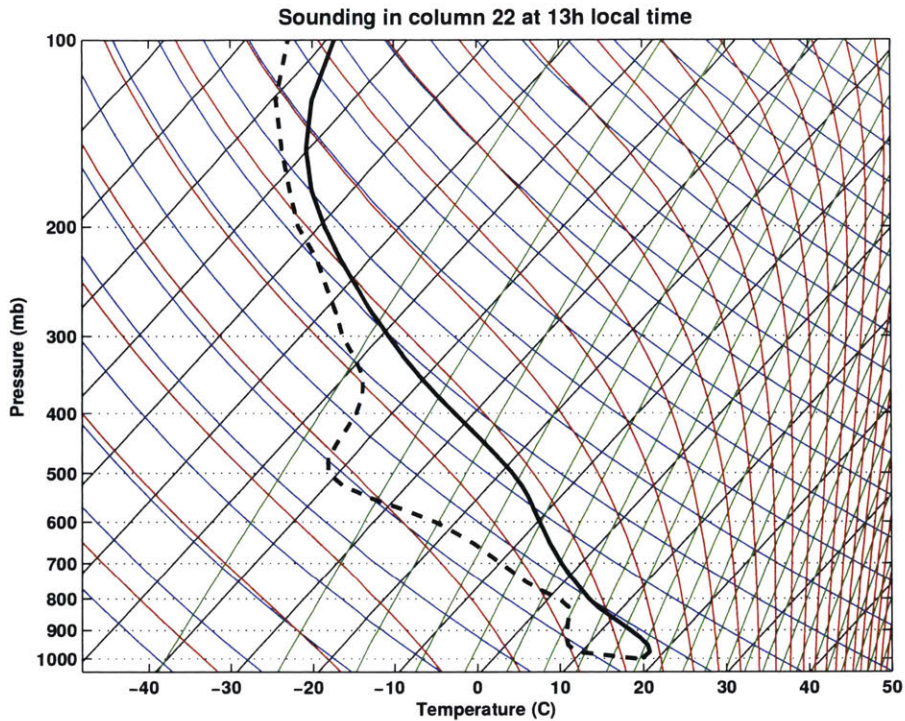


Figure 3-12: Skew-T diagram for westernmost ‘moist’ column at the time of peak CAPE.

s^{-1} , while data in Figs. 3-13b and 3-13c are of order $10^{-3} \text{ J kg}^{-1} \text{ s}^{-1}$, and data in Fig. 3-13d are of order $10^{-2} \text{ J kg}^{-1} \text{ s}^{-1}$.

Fig. 3-13a demonstrates that term (i) is maximized in the midday and afternoon, and in the wet land column closer to the dry land. This term is minimized overnight, and on the western boundaries of both land regions. The contribution due to radiational cooling (term ii) is maximized over the land columns during the overnight hours, and minimized at midday, as would be expected for a diurnal cycle of radiation. Term (iii) is positive in the overnight hours over the wet land, and negative over the overnight and morning hours over the dry land. This advective term is also minimized in the wet land column closest to the dry land in the late afternoon (hour 17). Finally, term (iv) is maximum in the morning hours over the dry land, while mainly negative over the wet land in the overnight hours and at around hour 10.

Fig. 3-14 compares the mean diurnal composite of CAPE tendency calculated

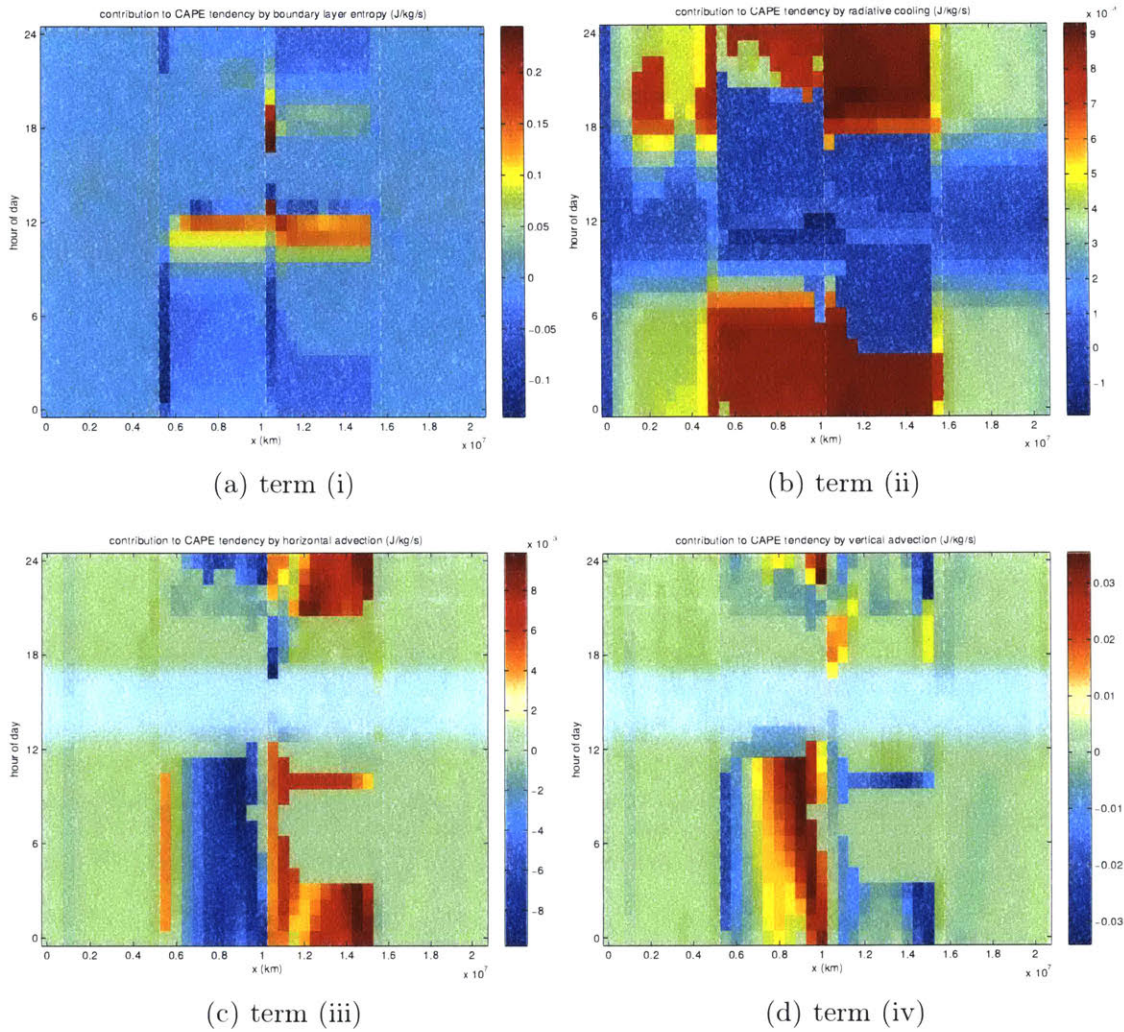


Figure 3-13: Hourly mean equilibrium contributions to the tendency of CAPE by each term in (3.5). The vertical dashed lines indicate the boundaries between the ocean, ‘dry’ land, and ‘wet’ land regions. The color scales are not the same for each image.

directly from CAPE output to the sum of terms (i) - (iv) in (3.5). From this figure, it can be concluded that the CAPE tendency budget in (3.5) is able to successfully reproduce the sign and magnitude of the CAPE tendency maximum at midday in the westernmost column of the wet land region, although the terms on the RHS of this equation appear to overestimate the CAPE tendency in the surrounding columns in the late morning, as well as the tendency in that column in the late afternoon. The late afternoon discrepancy is attributable to changes in CAPE due to convection at the wet/dry land boundary. Such convective activity would tend to act as a sink of CAPE that is unaccounted for by (3.5).

Comparing the magnitudes of terms (i)-(iv) in Fig. 3-13, the term containing the tendency of boundary layer entropy following a fluid parcel is dominant, as its values are on the order of $10^{-1} \text{ J kg}^{-1} \text{ s}^{-1}$, while the magnitudes of the vertical advection term, horizontal advection term, and radiative cooling term are 10^{-2} , 10^{-3} , and $10^{-3} \text{ J kg}^{-1} \text{ s}^{-1}$, respectively. Therefore, the boundary layer entropy tendency term comprises the majority of the RHS of (3-13), and so it can be concluded that to leading order, the daily maximum of CAPE in the column on the boundary of the wet land and dry land regions is caused by a gradient in the entropy of the boundary

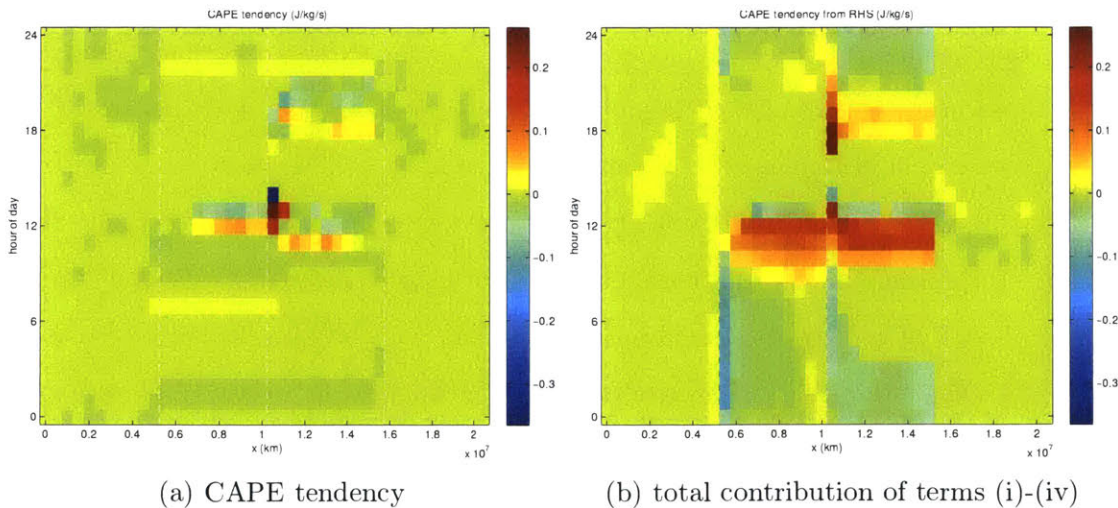


Figure 3-14: Hourly mean equilibrium values of the LHS (a) and RHS (b) of (3.5). The vertical dashed lines indicate the boundaries between the ocean, ‘dry’ land, and ‘wet’ land regions.

layer.

3.4 Discussion

The results of this work demonstrate that high levels of transient CAPE can be generated in a climatological sense by a two-dimensional idealized numerical model. In such a configuration, properties of the land surface are shown to have a significant effect on the preconditioning on the atmosphere for potentially severe convective storms.

3.4.1 Role of surface properties in supporting CAPE buildup

The presence of gradients in properties of the land surface is found to modulate atmospheric CAPE in statistical equilibria of the simplified minimal model. Specifically, discontinuities in surface evaporative fraction are found to give rise to relatively high levels of background CAPE in a two-dimensional, hydrostatic, nonrotating framework. In a two-column model, a sensitivity experiment determines mean equilibrium CAPE to be a monotonically increasing function of the difference in surface evaporative fraction between the two columns. This result is expanded to a 40-column framework including a background zonal flow. Under these conditions, relatively large equilibrium values of CAPE and CIN are supported just downstream of the discontinuity in surface evaporative fraction.

Upon introducing a diurnal cycle of solar radiation to the model, this configuration is found to produce large, but transient values of CAPE and CIN coincident on the ‘wet land’ side of the evaporative fraction boundary each day in the early afternoon. A budget calculation of the Lagrangian CAPE tendency shows that the tendency of boundary layer entropy is primarily responsible for the daily rapid generation of CAPE. This is consistent with the findings of Williams and Rennó (1993) and Donner and Phillips (2003) that boundary layer temperature and humidity are the main modulators of CAPE even in continental midlatitudes where the quasi-equilibrium assumption does not apply.

In this case, the entropy tendency following a parcel of air in the boundary layer is controlled by the surface evaporative fraction. Since a higher evaporative fraction yields a higher flux of entropy from the surface into the boundary layer (3.1), boundary layer parcels in columns in which the land surface has a high evaporative fraction experience a large entropy tendency when the surface is exposed to radiative heating by sunlight. In those columns with a low evaporative fraction, the low-level entropy is lower, but a hot, dry air layer is created and advected downstream by the background shear flow. Therefore, in those high- α columns nearest to the low- α columns, the hot air layer aloft allows the surface boundary layer entropy tendency to contribute to a rapid buildup of CAPE before convection is triggered. This is the same mechanism of CAPE production identified in North American reanalysis data in Chapter 2.

In addition to a sharp spatial gradient in CAPE, this model configuration also supports a sharp temporal gradient. Specifically, in the diurnally varying case (in which the magnitude of peak radiative heating allows a greater tendency of the boundary layer entropy), CAPE in the westernmost wet land column increases at over $500 \text{ J kg}^{-1} \text{ hr}^{-1}$ at midday to allow a mean daily maximum of 1700 J kg^{-1} . Furthermore, while this CAPE maximum is transient in nature, its rapid development in concurrence with a maximum in CIN is a combination that might support severe storms in the real atmosphere. Thus, the presence of a discrete gradient in surface evaporative fraction in this configuration allows the atmosphere to be thermodynamically preconditioned to support severe local storms in its equilibrium state.

While this simplified minimal model omits many important dynamics of the mid-latitude atmosphere (such as rotation), it is able to produce an atmosphere that is preconditioned for severe storms using a configuration that is analogous to that of continental North America. It is thereby demonstrated that a gradient of land surface moisture in a single dimension, under a particular wind pattern, is sufficient to produce high transient peak CAPE in a climatological sense.

3.4.2 Research limitations and errors

A possible source of error in these experiments is insufficient resolution of the modeled subcloud layer. Although the two-dimensional model is run with 46 vertical levels, in some cases there are only two levels below the level of free convection. This level of discretization makes robust use of finite-difference methods difficult. Furthermore, the model contains no parameterization of stable boundary layers, which is problematic when considering the flow of hot air over a relatively cool surface. Therefore, moving forward, it may be valuable to use increased vertical resolution at low levels, or to use a more complex model with more advanced boundary layer parameterizations, in order to more accurately calculate the contributions of radiative cooling and advection in the subcloud layer.

Additionally, the CAPE tendency budget equation (3.5) does not account for changes to the entropy of a given column of atmosphere due to convection itself. Therefore, the budget should not be expected to close at any time step during which the model's parameterized convection scheme is triggered. This is particularly relevant for the afternoon portions of the diurnal multicolumn experiment. However, since we are interested only in the buildup of CAPE prior to convection, and not the convection itself, this limitation does not detract from the main results.

Another limitation of this model configuration is its uniform height of terrain. It is hypothesized that in the real atmosphere, inhibitive hot layers such as those found in central North America are effective at allowing CAPE growth because the temperature inversion occurs at slightly elevated altitudes. The elevation of these layers is thought to be a consequence of the elevated nature of the desert terrain in which they are generated (Carlson and Ludlam 1968; Lanicci and Warner 1991; Banacos and Ekster 2010). This effect could not be fully captured in the idealized model used here, since elevated terrain is not a possible feature of the model. The background shear flow used in the multiple-column experiments compensates somewhat for this effect by advecting hot, dry air only above the surface boundary layer, but a model with variable terrain height could conceivably capture the elevated inhibitive layer in

a more directly analogous sense to the real atmosphere.

3.4.3 Future research

While this work confirms the importance of diabatic surface heating in the thermodynamic preconditioning of the atmosphere for continental convection, there is a multitude of ways in which this research could be extended to gain a better understanding of the climatological dependence of continental peak CAPE on environmental variables.

First, the same model, or a similar framework could be used to explore the sensitivity of these results to variations of other parameters. For example, the surface albedo of the upstream columns could be altered in conjunction with their evaporative fraction. Other parameters that could be altered include the magnitude of the background flow, magnitude and vertical extent of the background vertical wind shear, assumed background surface wind speed for surface heat fluxes, or relative populations of dry and wet land columns. Furthermore, the effects of replacing the discontinuous evaporative fraction distribution used in this study by a more continuous gradient could be examined.

This framework could also be extended to a model in which terrain height is allowed to vary. Using an elevated terrain height for the dry land region would allow more robust examination of the inversion layer generated there. As a parallel to (2.1), a budget for the tendency of CIN could be derived. A budget of CIN tendency could be used to test the hypothesis that differential advection is the process primarily responsible for supporting diurnally transient high values of CIN in the continental configuration examined here.

Finally, the approach used in this research could be applied to more complex models. Three-dimensional large-scale or cloud-permitting models could be used to repeat this experiment for a configuration that is not meridionally symmetric, or one for which rotation of the system is allowed. Incrementally adding more complex dynamics to the system would allow use of the CAPE tendency budget equation to determine which dynamics are relevant to climatological preconditioning for severe

convection.

Chapter 4

Clausius-Clapeyron scaling of peak CAPE

©2017 American Meteorological Society.¹

4.1 Introduction

Constraining the intensity of severe local storms in continental environments presents a major problem at the intersection of convective meteorology and climate. While continental convective storms can be among the most severe on Earth (Zipser et al. 2006), the problem of how such storms may vary as a function of climate has only recently begun to be addressed substantially (Brooks 2013; Tippett et al. 2015).

Convective storms present a unique challenge in that their spatial extent is too small for them to be resolved by general circulation models. This difficulty is exacerbated in continental convective environments, where, unlike for oceanic convection, the atmosphere cannot be considered to be in radiative-convective equilibrium. Therefore, climate research on these severe local storms often focuses on the environments in which severe local storms are formed. CAPE and deep-layer vertical wind shear

¹The contents of Chapter 4 are published as part of Agard and Emanuel (2017), in *Journal of the Atmospheric Sciences*. Permission to use figures and brief excerpts from this work in scientific and educational contexts is hereby granted provided that the source is acknowledged. A few minor edits have been made to the published work for the purpose of clarity in the context of this thesis.

are two important parameters that, when considered in tandem, provide a metric for the propensity of a given environment to support severe convection (Brooks 2009; Grams et al. 2012). Both CAPE and shear are necessary (although not sufficient) ingredients for severe convection over land, and their respective climatologies are important for determining the climatology of severe local storms. Here, we focus solely on constraining peak values of CAPE over land. We do not make any determinations about vertical wind shear as a function of climate, and therefore this study does not explicitly forecast changes in severe local storm climatology.

However, CAPE by itself still offers a significant environmental constraint on severe storms. Higher values of CAPE theoretically correspond to more intense storms (Weisman and Klemp 1982; Holton 2004), as CAPE provides an upper bound for the theoretical maximum updraft speed. Higher updraft speeds can in turn support larger hydrometeors or ground-level winds associated with a given storm. High CAPE is often associated with especially severe types of continental convection such as supercells (Emanuel 1994; Rasmussen and Blanchard 1998; Bluestein 2007). Recently, several authors have studied the behavior of continental CAPE in projected future climates using general circulation models. Trapp et al. (2007a) and Del Genio et al. (2007) predict increases in CAPE in the eastern half of the United States, and over land in general, respectively, under increased greenhouse radiative forcing. Diffenbaugh et al. (2013) and Seeley and Romps (2015) find evidence of CAPE driving an increase in favorable conditions for U.S. severe convection in data from CMIP5. Other studies achieve similar conclusions using dynamical downscaling of climate models (Gensini and Mote 2015) and numerical pseudo global warming experiments (Trapp and Hoogewind 2016).

Yet, despite a growing consensus from modeling studies that continental CAPE should increase with increased greenhouse gas forcing, a quantitative theory underpinning this change remains elusive. In general, one would expect warming scenarios in which temperature and moisture increase close to the surface to produce increased atmospheric instability. But can we say something more specific about the particular paradigm of instability generation that supports severe convection over land?

Currently, a theoretical constraint on even the order of magnitude of CAPE in such environments does not exist. For instance, why should CAPE be $2,000 \text{ J kg}^{-1}$, and not 200 J kg^{-1} , or $20,000 \text{ J kg}^{-1}$?

While other studies (Parodi and Emanuel 2009; Sobel and Camargo 2011; Romps 2011; Singh and O’Gorman 2013; Romps 2016) have derived scalings to constrain equilibrium energy scales for convection in the tropics, the highly transient nature of CAPE in continental environments precludes the use of a quasi-equilibrium framework for its study. Rather than quasi-equilibrium, the continental convection paradigm involves the time-dependent buildup and storage of potential energy in conditionally unstable profiles. It is the peak values of transient CAPE, rather than the time-averaged background levels, that are therefore relevant to the severe storm environments in which we are interested. Therefore, we develop a simple, idealized initial value problem encompassing a typical condition in which severe local storms might form in continental environments.

4.2 Idealized model

The scenario being modeled is one that is canonically associated with favorable severe weather environments over North America: The southwestern high desert gives rise to a hot, dry air mass that is advected eastward by the mean flow aloft. Under certain synoptic conditions, upon moving east of the Rocky Mountains, this air mass is superimposed above cooler, moister air near the surface in the Great Plains and Midwest (Emanuel 1994; Schultz et al. 2014). These regions are home to the continent’s most frequent occurrences of extreme peak CAPE (Brooks et al. 2003b), as the dry air mass acts as an inhibitive cap, allowing CAPE to rise as energy builds at the surface. It should be noted that the relative motion of the ‘dry’ and ‘moist’ air masses aloft and near the surface, respectively, often also provides the requisite shear for supporting severe local storms.

With an inhibitive cap in place aloft, CAPE can be generated by one of three mechanisms (Emanuel 1994): First, air in the free troposphere can be radiatively

cooled, thereby increasing instability for parcels lifted from near the surface. A second possible mechanism for CAPE buildup in this scenario is the low-level advection of high-entropy air from outside the column, causing an increase in instability by supplying increased heat and moisture to the boundary layer from which parcels might be lifted. Finally, CAPE can be generated by the diabatic heating of near-surface air from below, as heat and moisture (to the extent to which moisture is available) are fluxed from the land surface into the boundary layer in response to diurnal solar forcing. In general, the differential advection pathway and the diabatic heating pathway are thought to be the most important in generating CAPE in severe storm environments such as those in the Great Plains, with the former being more important earlier in the spring season when synoptic forcing is greater (Brooks et al. 2003a).

This model examines the diabatic heating pathway in which low-level moisture in the boundary layer below the elevated inhibitive cap is generated in situ through the flux of latent heat from the land surface. In the sense that the model generates transient peaks of CAPE in the absence of external low-level advection, we thereby demonstrate that the placement of dry air over a moist land surface in the presence of diabatic heating is sufficient for providing instability to continental severe storm environments.

The synoptic-scale circumstances outlined above can be simply and ideally modeled by considering a one-dimensional problem in which a dry adiabatic column is placed in contact with a moist surface. As in the real-world case of dry desert air placed above a moister, vegetated surface, surface latent heat flux gives rise to a moist surface boundary layer that expands with time, given some radiative input to the surface.

The model consists of a single column of atmosphere placed atop a zero-heat capacity land surface. In order to study the simplest possible case, we begin with an atmosphere that has zero water vapor everywhere. The column is assumed to follow a dry adiabatic temperature profile throughout its entire depth, with a near-surface air temperature of T_0 . This pre-initial condition is shown schematically in Fig. 4-1a,

and an example of the temperature profile created is shown in Fig. 4-3a.

Then, at time $t = 0$, a cooler, moister surface is instantaneously introduced. To accommodate the new lower boundary condition, a surface boundary layer with some initial height h_0 is created, as shown in Fig. 4-1b. The boundary layer is assumed to have a nonzero specific humidity that is constant with height, and a temperature profile that follows a dry adiabat (but at a cooler temperature than the that of the pre-initial dry column). It is assumed (for a perfectly moist surface) that the air at $z = h_0$ has cooled to its wet bulb temperature, such that saturation is achieved exactly at the top of the boundary layer. For less moist surfaces, we assume that the air at $z = h_0$ achieves a relative humidity equal to the evaporative fraction of the surface. The column above $z = h_0$ (henceforth the “free troposphere”) remains unperturbed, and retains its initial dry adiabatic temperature profile. An example of this is shown in Fig. 4-3b.

At time $t > 0$, the system is forced with a constant net radiative flux F_{rad} into the surface. Since the land surface has zero heat capacity, we require the radiative input to be exactly balanced by a sensible heat flux F_S , and a latent heat flux F_L from the surface into the boundary layer. As time evolves, the boundary layer expands upward,

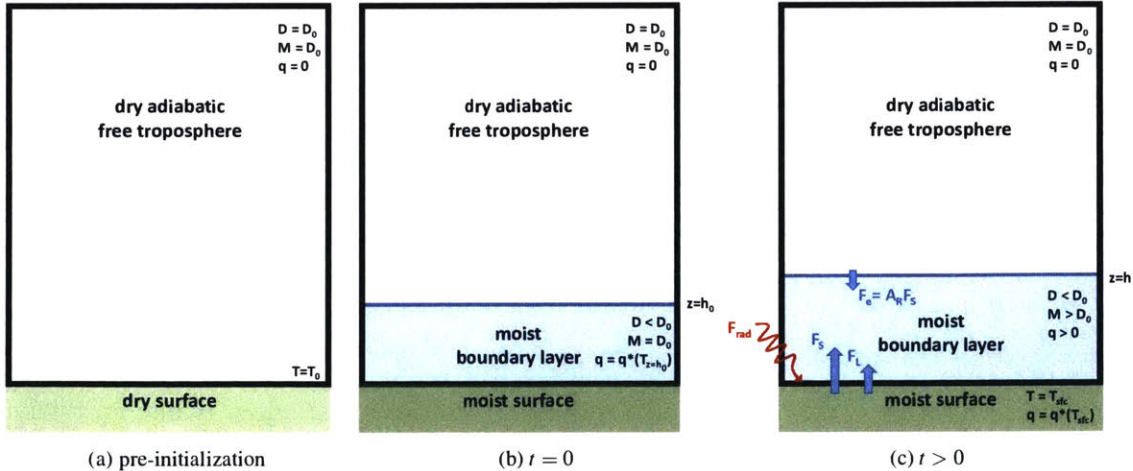


Figure 4-1: Schematic of the single-column idealized model (a) before introduction of the moist surface and boundary layer, (b) at the initial time, and (c) during its evolution. Indicated on each diagram are the dry static energy (D), moist static energy (M), temperature (T), and specific humidity (q) of each part of the system.

entraining dry air from above as it does so. There is an associated entrainment heat flux, represented by F_e , owing to the discontinuous jump in temperature between the boundary layer and free troposphere. This configuration is illustrated in Fig. 4-1c.

It is assumed that the depth of the surface boundary layer is greater than the Monin-Obukhov (1954) length, so that the growth of the boundary layer is thermodynamically, rather than mechanically driven. We therefore assume the entrainment flux at the top of the boundary layer to be proportional by a constant (A_R) to the surface sensible heat flux, as in Lilly (1968):

$$F_e = \rho(D_0 - D)w_e = A_R F_S, \quad (4.1)$$

where w_e is the entrainment velocity, a measure of the turbulent entrainment into the boundary layer of quiescent air from above, and ρ is a reference density of air. A typical value of A_R is 0.2.

The evolution of the system is modeled in terms of the dry and moist static energies of the boundary layer and free troposphere. Since the free troposphere contains no moisture and retains the dry adiabatic temperature profile of the pre-initial column for all time, its dry and moist static energy are both equal to the constant

$$D_0 = c_p T_0, \quad (4.2)$$

where c_p is the specific heat capacity of dry air. Meanwhile, since the boundary layer has a constant vertical profile of water vapor and a dry adiabatic temperature profile, its dry static energy D and moist static energy M are both constant in height (but not in time). We assume that the initial moistening of the boundary layer is done in a way that conserves moist static energy, so at $t = 0$, $M = D_0$. However, since the boundary layer is therefore cooled during the initial moistening, it has an initial dry static energy $D < D_0$ at $t = 0$, with a discontinuity in dry static energy across the interface between the boundary layer and the free troposphere. Therefore, at the beginning of the initial value problem, there is a deficit of dry static energy in the boundary layer with respect to the free troposphere. This deficit in dry static energy

can be thought of as a measure of the inhibitive cap arising from the temperature inversion at the interface with the free troposphere.

As time evolves, heating of the boundary layer by F_S and F_e causes D to increase, thereby decreasing the deficit in dry static energy. The decreasing dry static energy deficit represents the erosion of convective inhibition by diabatic heating. Consequently, when the dry static energy deficit goes to zero, the cap is eliminated and convection can be thermodynamically triggered— this represents the end of the problem we address here.

Concurrently, the fluxes of heat and moisture from the land surface into the boundary layer cause M to initially increase, thereby creating a surplus in moist static energy in the boundary layer with respect to the free troposphere. This moist static energy surplus will serve as a proxy for the thermodynamic instability of the column.

The evolutions of D , M , and the boundary layer height h with time t are described by a set of ordinary differential equations:

$$\rho h \frac{dD}{dt} = F_S + \rho w_e (D_0 - D) \quad (4.3)$$

$$\rho h \frac{dM}{dt} = F_{\text{rad}} + \rho w_e (D_0 - M) \quad (4.4)$$

$$\frac{dh}{dt} = w_e \quad (4.5)$$

$$F_S = \rho C_T v_{\text{sfc}} (c_p T_{\text{sfc}} - D) \quad (4.6)$$

$$F_L = \alpha \rho C_T v_{\text{sfc}} [L_v q^*(T_{\text{sfc}}) - M + D] \quad (4.7)$$

$$F_S + F_L = F_{\text{rad}}. \quad (4.8)$$

Here, the rate of change of the boundary layer height h is set equal to the entrainment velocity w_e , as defined by (4.1). This velocity scale therefore governs both the growth of the boundary layer and the dilution of its dry and moist static energies. We have also introduced the nondimensional coefficient α to modify the availability of surface moisture for evaporation. This evaporative fraction parameter holds a fractional value between 0 and 1, with those limits effectively representing a totally dry surface, and a (zero- heat capacity) ocean surface, respectively. The bulk aerodynamic flux formulas

also include the parameter v_{sfc} , an assumed background wind speed for surface fluxes, and the time-dependent temperature of the land surface, T_{sfc} . Finally, L_v is the latent heat of vaporization of water, and C_T is the nondimensional aerodynamic flux coefficient.

At $t = 0$, the initial conditions of the system are given by

$$D = D_0 - \Delta D_{\text{init}} \quad (4.9)$$

$$M = D_0 \quad (4.10)$$

$$h = h_0, \quad (4.11)$$

where ΔD_{init} is calculated from the assumption of fractional saturation at the top of the initial boundary layer, according to

$$\Delta D_{\text{init}} = c_p(T_0 - T_{b_{\text{init}}}) \quad (4.12)$$

$$T_{b_{\text{init}}} = T_w + gh_0 \quad (4.13)$$

$$c_p T_w + \alpha L_v q^*(T_w) = c_p(T_0 - gh_0), \quad (4.14)$$

where $T_{b_{\text{init}}}$ is the near-surface air temperature in the initial boundary layer, and T_w is the temperature at the top of the initial boundary layer. T_w is the temperature achieved by cooling the pre-initial air at $z = h_0$ to the point at which its relative humidity is equal to α , while conserving moist static energy.

The time-dependent variables are nondimensionalized according to

$$\delta \equiv \frac{D_0 - D}{D_0} \quad (4.15)$$

$$\mu \equiv \frac{M - D_0}{D_0} \quad (4.16)$$

$$\eta \equiv \frac{h}{h_0} \quad (4.17)$$

$$\tau \equiv \frac{C_T v_{\text{sfc}} t}{h_0} \quad (4.18)$$

$$\delta_s \equiv \frac{c_p T_{\text{sfc}}}{D_0} \quad (4.19)$$

$$\mu_s \equiv \frac{c_p T_{\text{sfc}} + L_v q^*(T_{\text{sfc}})}{D_0}, \quad (4.20)$$

where δ , μ , η , and τ represent the dry static energy deficit, moist static energy surplus, boundary layer height, and time, respectively. The dry and moist static energies of the land surface are represented by δ_s and μ_s . All variables are defined to be positive-definite.

Additionally, we define the nondimensional constant

$$\Phi \equiv \frac{F_{\text{rad}}}{\rho C_T v_{\text{sfc}} D_0} \quad (4.21)$$

to represent the net radiative surface input.

Applying the normalizations in (4.15) through (4.21) to (4.3) through (4.8) yields the following nondimensional system of equations:

$$\frac{d\delta}{d\tau} = -\frac{1 + A_R}{\eta}(\delta_s + \delta - 1) \quad (4.22)$$

$$\frac{d\mu}{d\tau} = \frac{\Phi}{\eta} - \frac{\mu A_R}{\eta \delta}(\delta_s + \delta - 1) \quad (4.23)$$

$$\frac{d\eta}{d\tau} = \frac{A_R}{\delta}(\delta_s + \delta - 1) \quad (4.24)$$

$$(1 - \alpha)(\delta + \delta_s) + \alpha(\mu_s - \mu) - 1 = \Phi. \quad (4.25)$$

This system is partially analytically integrated to arrive at a system of three diagnostic

equations and one time-dependent ODE:

$$\delta = \delta_{\text{init}} \eta^{-\frac{1+A_R}{A_R}} \quad (4.26)$$

$$\mu = \frac{\Phi}{\eta} \quad (4.27)$$

$$\frac{d\eta}{d\tau} = \frac{A_R}{\delta} (\delta_s + \delta - 1) \quad (4.28)$$

$$(1-\alpha)(\delta + \delta_s) + \alpha(\mu_s - \mu) - 1 = \Phi. \quad (4.29)$$

Note that while these four equations contain five unknown variables, both δ_s and μ_s are functions of the surface temperature T_{sfc} , as described by (4.19) and (4.20).

At time $\tau = 0$, the nondimensional initial conditions are given by

$$\delta = \delta_{\text{init}} \quad (4.30)$$

$$\mu = 0 \quad (4.31)$$

$$\eta = 1. \quad (4.32)$$

The system is integrated numerically to achieve time series of δ , μ , and η . The integration ends when $\delta = 0$, since at that time the temperature inversion has been erased, and convection is therefore thermodynamically permitted.

4.3 Results

Solutions to (4.26) through (4.29) fall into three distinct categories, depending on the choice of parameters T_0 , α , v_{sfc} , and F_{rad} . Fig. 4-2 shows an example solution belonging to the intermediate category. However, this solution exhibits characteristics common to each category of solutions:

After $\tau = 0$, δ decreases monotonically with time as heat is fluxed into the boundary layer from the surface and entrained from above, causing the temperature of the boundary layer to approach that of the free troposphere. Likewise, the height of the boundary layer increases monotonically with time, as the entrainment flux from the

free troposphere remains positive. While the boundary layer initially grows relatively slowly, the growth rate increases substantially toward the end of the problem as the dry static energy deficit is eroded and the temperature jump across the interface with the free troposphere becomes small.

The rapid expansion of the boundary layer at later times results in non-monotonic behavior of μ . While μ initially increases due to the flux of moist static energy from the moist surface into the boundary layer, the rapid entrainment of dry air from the free troposphere at later times causes the moist static energy of the boundary layer to decrease. Consequently, the moist static energy surplus reaches a maximum some time before the end of the problem. This transient peak in μ corresponds to a transient peak in CAPE.

After its peak is reached, the behavior of the μ time series depends on the problem's location in parameter space, as shown in Fig. 4-4. Keeping other parameters constant, the time evolution of the moist static energy surplus falls into one of three regimes, depending on the temperature of the initial dry profile.

At low temperature, the moist static energy of the boundary layer subsides to that of the free troposphere ($\mu \rightarrow 0$) as the temperature of the boundary layer approaches that of the free troposphere ($\delta \rightarrow 0$). In this regime, the convective instability of the column is completely eliminated at the same time that its convective inhibition goes to zero. Thermodynamically-triggered convection is therefore impossible. However, the thermodynamic instability of the column does reach a transient peak shortly

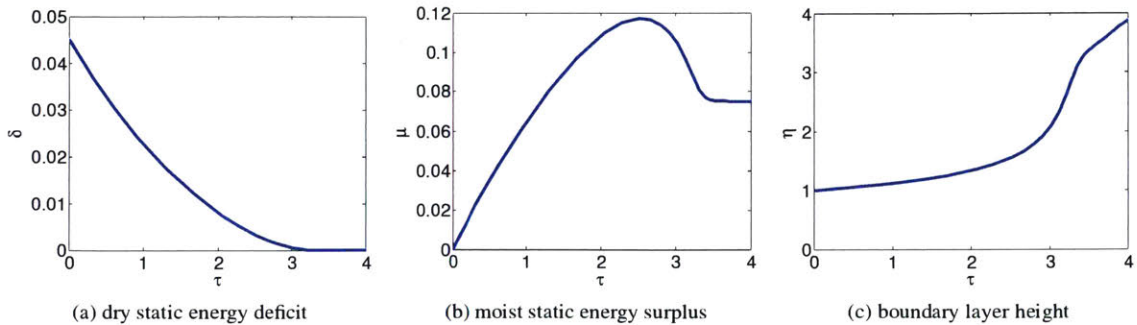


Figure 4-2: Numerically integrated time series of (a) δ , (b) μ , and (c) η for $T_0 = 305$ K, $\alpha = 0.5$, $h_0 = 100$ m, $v_{\text{sfc}} = 5$ m s⁻¹, and $F_{\text{rad}} = 200$ W m⁻².

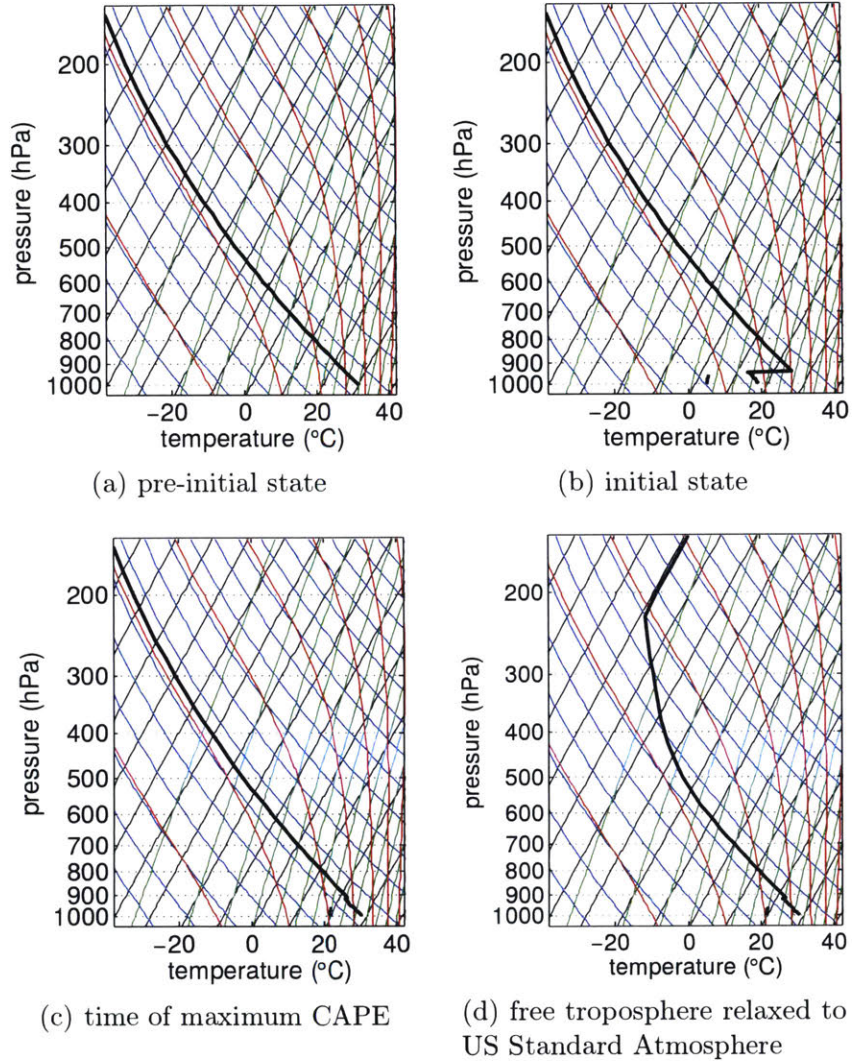


Figure 4-3: Skew-T diagrams depicting the vertical profile of temperature (solid black line) and dew point temperature (dashed black line) for an example model solution in which $T_0 = 305$ K, $\alpha = 0.5$, $h_0 = 500$ m, $v_{sfc} = 5$ m s⁻¹, and $F_{rad} = 200$ W m⁻², at (a) $t < 0$, (b) $t = 0$, (c) the time at which maximum CAPE is achieved, and (d) the same time as (c), but with the temperature of the free troposphere relaxed to that of the U.S. Standard Atmosphere (1976).

before the inhibitive cap is exhausted, at which time convection could be triggered by modest dynamic uplift.

At warmer temperatures, the system enters an intermediate regime, in which μ reaches a transient peak before relaxing to a finite positive value. The value that μ attains in its long-time limit is dictated by the initial temperature of the dry adiabatic profile, T_0 . In this regime, thermodynamically-triggered convection is possible, since a finite amount of instability remains after the dry static energy deficit is removed. Still, a transient peak in μ is reached while δ is nonzero in this regime.

Finally, at the warmest temperatures, the moist static energy surplus has no transient maximum at all. Instead, the maximum value of μ is approached asymptotically as δ goes to zero as time goes to infinity. In this regime, the maximum value of the moist static energy surplus is identical to its long-time limit.

In all three regimes, two of the three requirements for preconditioning the en-

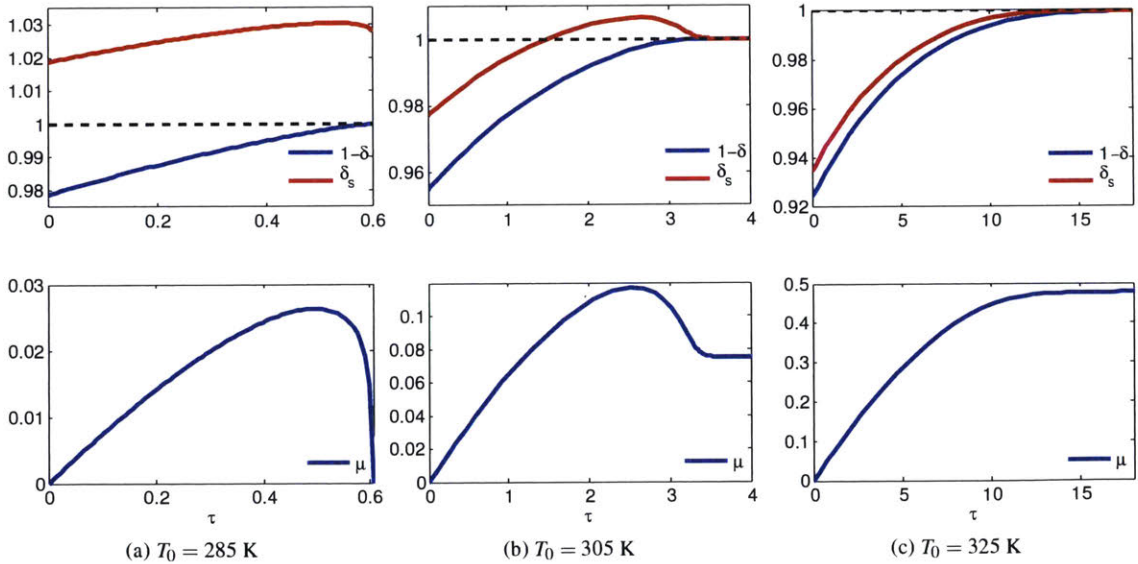


Figure 4-4: Top panel: Time evolution of boundary layer dry static energy (solid blue line) and surface dry static energy (solid red line) for three different values of T_0 , with $\alpha = 0.5$, $h_0 = 100$ m, $v_{\text{sfc}} = 5$ m s $^{-1}$, and $F_{\text{rad}} = 200$ W m $^{-2}$. Boundary layer dry static energy is plotted as $1 - \delta$ to provide a nondimensionalized measure of near-surface air temperature. The dashed black line at $\delta = 1$ represents the level at which temperature is equal to T_0 . Bottom panel: Time evolution of the moist static energy surplus corresponding to each case. Panels a, b, and c represent the peak, intermediate, and asymptotic regimes, respectively.

environment for deep convection (as outlined in Doswell et al. 1996) are met: The environmental temperature profile is conditionally unstable, and the boundary layer contains sufficient moisture such that lifted parcels will become saturated and positively buoyant if they enter the free troposphere. The final requirement, which applies in all three regimes when μ is maximized before δ goes to zero, is that some process provides dynamical lift for parcels to reach their level of free convection. The question of how and when this trigger is provided is outside the scope of this study, but we can still attain information about the magnitude of the transient peak in conditional instability.

In both the intermediate regime and the fully-asymptotic regime, the long-time limit of the dimensional moist static energy surplus is given by

$$\lim_{t \rightarrow \infty} M - D_0 = L_v q^*(T_0) - \frac{F_{\text{rad}}}{\alpha \rho C_T v_{\text{sfc}}}, \quad (4.33)$$

as derived in Appendix B. In the warmest regime, this limit provides an expression for the maximum value of M , whereas in the intermediate regime, M exhibits a transient peak at a value greater than its long-time limit.

It is also notable that the expression in (4.33) is independent of the initial boundary layer height parameter h_0 . We therefore consider the limit in which the initial boundary layer depth goes to zero. In this case, the nondimensional time τ goes to infinity for any positive t , according to (4.18). The long-time limit of the system is thereby reached immediately. Therefore, in the limit of an initially shallow boundary layer, the solution for M is given explicitly by the expression in (4.33).

The boundaries between each of the three regimes are given by

$$\text{peak:} \quad q^*(T_0) < \frac{F_{\text{rad}}}{\alpha \rho C_T v_{\text{sfc}} L_v} \quad (4.34)$$

$$\text{intermediate:} \quad \frac{F_{\text{rad}}}{\alpha \rho C_T v_{\text{sfc}} L_v} < q^*(T_0) < \left(\frac{1}{A_R} + \frac{1}{\alpha} \right) \frac{F_{\text{rad}}}{\rho C_T v_{\text{sfc}} L_v} \quad (4.35)$$

$$\text{asymptotic:} \quad q^*(T_0) > \left(\frac{1}{A_R} + \frac{1}{\alpha} \right) \frac{F_{\text{rad}}}{\rho C_T v_{\text{sfc}} L_v}, \quad (4.36)$$

as derived in Appendix C. Increasing the initial atmospheric temperature T_0 , the

evaporative fraction α , or the surface wind speed v_{sfc} ; or decreasing the net surface radiative input F_{rad} each has the effect of moving toward the asymptotic regime.

For most reasonable parameter choices, the boundary layer does not achieve saturation during its evolution, as shown in Fig. 4-5. Supersaturations (in which the relative humidity at the top of the boundary layer exceeds 1) occur only at particularly high values of surface moisture and pre-initial temperature. Since this model does not account for cloud formation in the boundary layer, it is ill-equipped to handle supersaturations. However, for the majority of relevant parameter space, they do not occur.

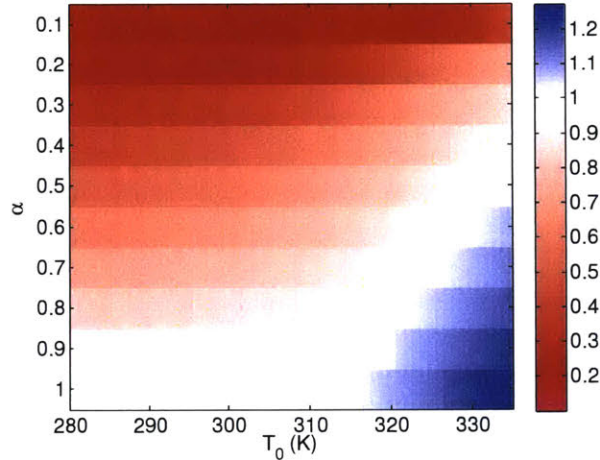


Figure 4-5: Maximum relative humidity achieved at the top of the boundary layer during its evolution as a function of T_0 and α , for $h_0 = 100$ m, $v_{\text{sfc}} = 5$ m s $^{-1}$, and $F_{\text{rad}} = 200$ W m $^{-2}$.

4.4 Scaling of peak CAPE

By considering a parcel lifted from the boundary layer with moist static energy M into the free troposphere, whose environmental moist static energy is a constant D_0 in height and time, we calculate from (1.1) an approximate dimensional CAPE as a function of the boundary layer moist static energy surplus:

$$CAPE \approx \int_h^{z_{\text{LNB}}} \frac{g}{c_p} \left(\frac{M_p - M_e}{T_e} \right) dz = (M - D_0) \ln \left(\frac{T_h}{T_{\text{LNB}}} \right), \quad (4.37)$$

where M_p is the moist static energy of the lifted parcel (equal to M), M_e and T_e are the moist static energy and temperature, respectively, of the environment, T_h is the temperature at the top of the boundary layer, and T_{LNB} is the temperature at the parcel's level of neutral buoyancy. It is assumed that the deep convection resulting from the stored CAPE will reach the tropopause, and therefore that the temperature at the level of neutral buoyancy is coincident with the temperature at the tropopause in a typical column. Taking a rough average of data from Hoinka (1999), Holton et al. (1995), and the U.S. Standard Atmosphere (1976), we assume a value of $T_{\text{LNB}} \approx 220$ K for a midlatitude column.

Fig. 4-6 shows the time evolution of CAPE for several values of the pre-initial near-surface air temperature T_0 , for a given choice of the surface moisture parameter. The functional forms of the time evolution of CAPE closely resemble those of the time evolution of μ , since CAPE in this model has a linear dependence on boundary layer moist static energy. However, CAPE also depends on the height of the boundary layer: As η increases with time, the top of the boundary layer becomes progressively colder. Most notably, in the asymptotic regime, η continues to grow linearly after δ goes to zero. In those cases, since the long-time limit of D is D_0 , the entire column reverts to its pre-initial dry adiabatic temperature profile. Therefore, as h increases linearly with time, T_h must decrease along a dry adiabat. Consequentially, while M remains at its asymptotic value for infinite time, CAPE actually decreases with time after the dry static energy surplus is sufficiently small.

Therefore, CAPE has a transient peak in every regime. This transience is due to the competing effects of two different mechanisms: Surface fluxes heat and moisten the boundary layer, thereby increasing the thermodynamic instability of the column. Meanwhile, the upward growth of the boundary layer engenders entrainment of dry air from the free troposphere above, acting to decrease instability. CAPE is further diminished as the increasing altitude of the boundary layer top lessens the area of positive buoyancy for lifted parcels. Near the beginning of this initial value problem, the surface fluxes dominate as the boundary layer grows slowly, but they are eventually overwhelmed by the boundary layer growth process— this is the time at which

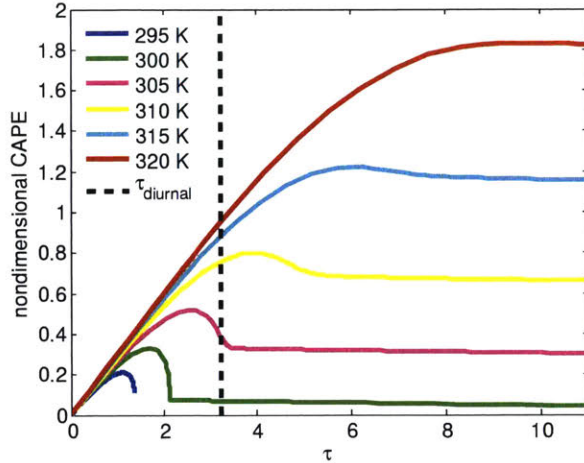


Figure 4-6: Evolution of CAPE with time for several different values of T_0 , given $\alpha = 0.5$. Here, CAPE is nondimensionalized by a factor of $\rho C_T v_{\text{sfc}} F_{\text{rad}}^{-1}$, while time is nondimensionalized according to (4.18). The dashed black line displays the end of a 12-hour diurnal time scale corresponding to the particular parameter choices $h_0 = 100$ m and $v_{\text{sfc}} = 5$ m s $^{-1}$.

peak CAPE is reached.

The value of peak CAPE increases monotonically with increasing temperature when other parameters are held fixed.

The functional relationship between peak CAPE and initial near-surface air temperature is shown by the solid green line in Fig. 4-7. For any given fixed set of parameters (F_{rad} , α , h_0 , v_{sfc}), peak CAPE is found to increase approximately exponentially with increasing temperature T_0 . Note that dimensional CAPE in this model is considerably higher than that which is observed in nature; this is due to the idealizations made in constructing the model, in particular the assumption that the boundary layer is topped by a perfectly dry adiabatic layer with unlimited depth. The effect of this assumption is explored in Fig. 4-3, which shows the time evolution of the vertical temperature profile for an example solution at $T_0 = 305$ K. Fig. 4-3c shows the most unstable temperature profile in the evolution of the column, under the assumption that the free troposphere follows the dry adiabatic lapse rate to an infinite height. In this case, CAPE is estimated by (4.37) to be 10,600 J kg $^{-1}$. In Fig. 4-3d, however, the free troposphere is given a lapse rate more typical of the real atmosphere by relaxing in height that same most unstable profile to the U.S. Standard

Atmosphere (1976) above the boundary layer using an exponential function. With this modification, an explicit level of neutral buoyancy exists, and CAPE is directly calculated to be $4,500 \text{ J kg}^{-1}$, a value that more closely reflects levels of extreme CAPE that might be observed in a continental severe weather environment. While the magnitude of the peak of CAPE is significantly reduced by the implementation of a more realistic free troposphere, one would expect that the overall scaling of CAPE with T_0 would retain its functional form if this artificial correction were applied across the board.

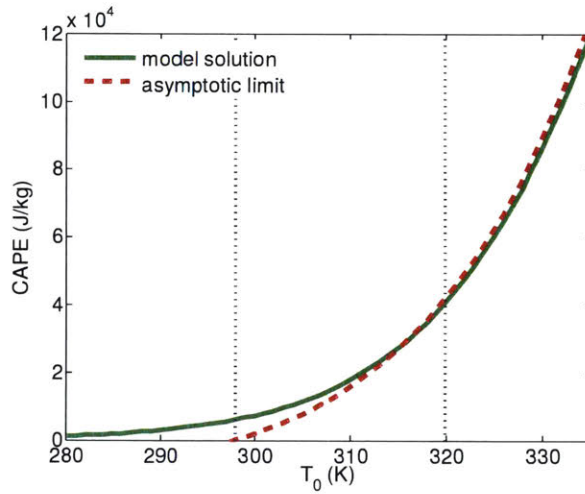


Figure 4-7: Modeled dimensional peak CAPE as a function of T_0 (solid green line) for $\alpha = 0.5$, $h_0 = 100 \text{ m}$, $v_{\text{sfc}} = 5 \text{ m s}^{-1}$, and $F_{\text{rad}} = 200 \text{ W m}^{-2}$; and a theoretical curve (dashed red line) corresponding to the asymptotic limit of CAPE that arises as $t \rightarrow \infty$, or $h_0 \rightarrow 0$. This curve is an exact solution to the Clausius-Clapeyron relation, as described by (4.38). The dotted black lines indicate the boundaries between the three regimes of model solutions.

Combining (4.33) and (4.37) provides an expression for CAPE as a function of the solution to the Clausius-Clapeyron equation relating saturation specific humidity to temperature:

$$\lim_{t \rightarrow \infty} \text{CAPE} = \left[L_v q^*(T_0) - \frac{F_{\text{rad}}}{\alpha \rho C_T v_{\text{sfc}}} \right] \ln \left(\frac{T_h}{T_{\text{LNB}}} \right). \quad (4.38)$$

This solution, shown by the dashed red line in Fig. 4-7, defines the response of the long-time limit of CAPE to changes in temperature. It therefore corresponds ex-

actly to peak CAPE in the asymptotic (warmest) regime for any initial boundary layer depth, and in all regimes for the limit in which $h_0 \rightarrow 0$. The solution is linearly dependent on $q^*(T_0)$, and peak CAPE therefore scales exactly according to the Clausius-Clapeyron relation in the temperature space for which it applies.

As peak CAPE increases with increasing temperature, so too does the time required for peak CAPE to be achieved. This presents an issue, since in nature the boundary layer does not grow continuously for infinite time. Instead, energetic input to the system stops as the sun sets and the net radiative input to the surface goes to zero. This issue could be addressed by imposing a diurnal cycle on the surface radiative input; for simplicity, we merely introduce a limiting dimensional time scale after which the constant radiation is to be cut off. We assume a cut off time scale of 12 hours (or nondimensionally, $\tau_{\text{diurnal}} = C_T v_{\text{sfc}} h_0^{-1} \cdot 12 \text{ hours}$) to be a duration representative of diurnal radiative input. The maximum dimensional CAPE achieved within time τ_{diurnal} is shown in Fig. 4-8 as a function of T_0 for a particular choice of h_0 , v_{sfc} , α , and F_{rad} .

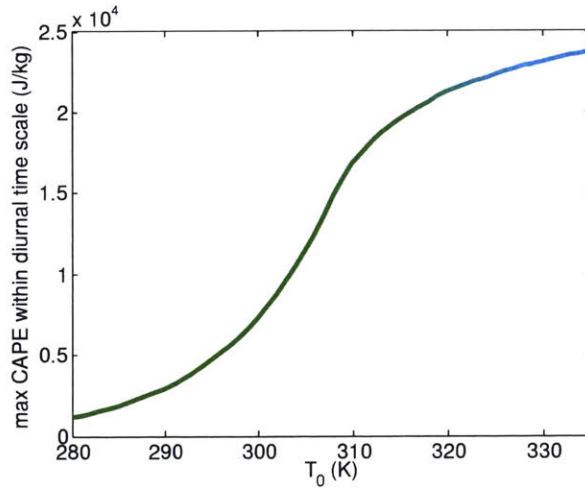


Figure 4-8: Modeled maximum CAPE within a diurnal time scale, as a function of T_0 for $\alpha = 0.5$, $h_0 = 100 \text{ m}$, $v_{\text{sfc}} = 5 \text{ m s}^{-1}$, and $F_{\text{rad}} = 200 \text{ W m}^{-2}$.

The imposition of the diurnal time limit introduces a new behavior for peak CAPE values at high temperature. This model predicts that, for a given choice of constant parameters, increasing T_0 will cause the peak in CAPE to occur later in the day. At

low temperatures (in this case, $T_0 \lesssim 305$ K), the CAPE peak occurs prior to the end of the diurnal time scale, so the curve of peak CAPE with T_0 retains its exponential nature. At higher temperatures, CAPE is still increasing when $\tau = \tau_{\text{diurnal}}$, so the maximum in CAPE occurs at the diurnal time limit. In this regime, the maximum in CAPE still increases with increasing T_0 , but its rate of increase is lessened. A consequence of this is the existence of a maximum in the sensitivity of peak CAPE with respect to temperature. In Fig. 4-8, this sensitivity maximum occurs at $T_0 \approx 305$ K.

Finally, we vary the surface moisture (α), wind speed (v_{sfc}), and initial boundary layer height (h_0) parameters to determine their effects on peak CAPE. These results are shown in Fig. 4-9. The flux of moist static energy from the surface to the boundary layer that fuels CAPE buildup is a function of both surface moisture and wind speed. Increasing either the surface moisture parameter or the surface wind speed parameter has the effect of modifying the Bowen ratio such that a greater portion of the surface moist static energy flux is partitioned to latent heat flux. Both peak CAPE and the time taken to achieve it are thereby increased. As a consequence, CAPE increases more quickly with increasing temperature, but the regime of maximum sensitivity is shifted to lower temperatures. Nevertheless, for a fixed T_0 , increasing either α or v_{sfc} has the monotonic effect of increasing peak CAPE.

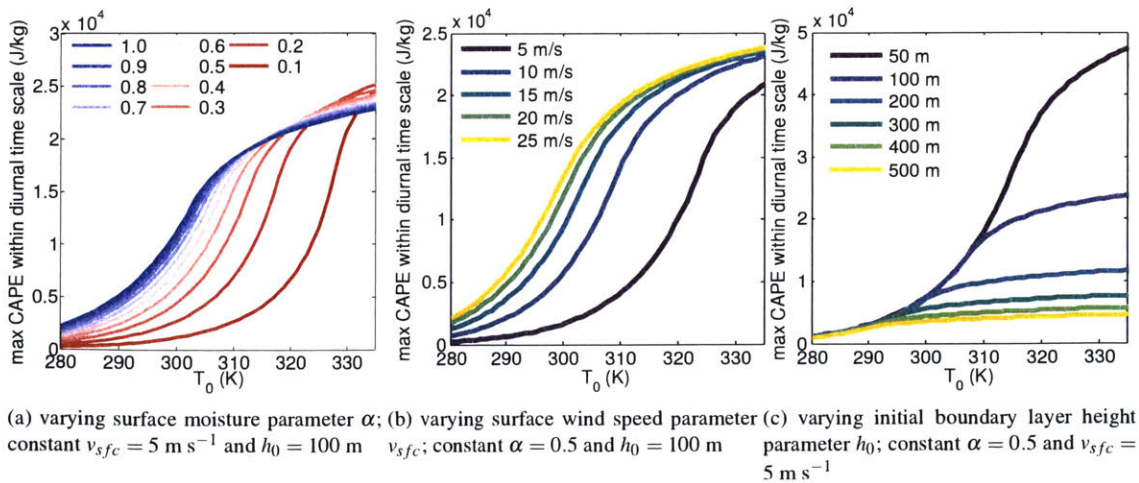


Figure 4-9: Modeled maximum CAPE within a diurnal time scale, as a function of T_0 with varying α , v_{sfc} , and h_0 .

The exception is that for sufficiently high temperatures (in this example, $T_0 \gtrsim 320$ K), increasing α slightly decreases the maximum CAPE that can be achieved within the diurnal time scale. This is due to the assumption that a moister surface is associated with a moister, and therefore cooler initial boundary layer. This effect acts to decrease the initial Bowen ratio, thereby increasing the time taken for peak CAPE to be reached. Imposing the diurnal time cutoff translates this slower CAPE buildup into a smaller value of maximum CAPE achieved within that time.

At low T_0 , changing h_0 has little effect on peak CAPE. However, a deeper boundary layer requires a larger total flux to achieve an equivalent buildup of moist static energy. Raising the initial boundary layer height thereby has the effect of prolonging the time needed for peak CAPE to be achieved. The temperature at which the diurnal cutoff time scale becomes the limiting factor for peak CAPE is therefore lower for solutions with deeper boundary layers. Thus, while the diurnal cutoff time is unimportant at sufficiently cool temperatures, increasing h_0 monotonically decreases the maximum CAPE within the diurnal time scale at warmer temperatures.

4.5 Discussion

The idealized column model developed here introduces a theoretical constraint on transient peak CAPE for a particular mechanism of instability generation unique to continental severe weather environments. Both in the presence and in the absence of a limiting time scale, the model predicts increasing peak CAPE with the increasing temperature of the pre-initial dry column that provides the capping inversion.

In the case of no limiting time scale, peak CAPE scales exponentially with the temperature of the elevated dry layer and follows an exact solution to the Clausius-Clapeyron equation. For a given range of temperatures, the magnitude of peak CAPE is a direct function of the pre-initial saturation specific humidity of the dry column. This is consistent with past studies linking the growth rate of CAPE with temperature to the increase in the water vapor capacity of air with increasing temperature (as found by Romps (2011) and Romps (2016) for tropical climate). The idealized col-

umn model derived here extends this theoretical thermodynamic constraint on severe convection to continental environments.

In the case in which radiative input to the surface is limited by the time scale of the diurnal cycle, peak CAPE also increases monotonically with dry layer temperature, but as temperature increases, the peak occurs at a later time. This result is consistent with Gensini and Mote (2015), which found a delay in the diurnal distribution of severe convection in dynamically downscaled future climate simulations. At sufficiently high temperatures, the time of peak CAPE coincides with the end of the diurnal time scale, at which point the relationship between temperature and peak CAPE diverges from the exponential Clausius-Clapeyron scaling.

Finally, we conclude that high temperature, high available moisture in the land surface, and high surface winds are each conducive to increased peak CAPE. This suggests that for the particular means of CAPE buildup studied by this model, increasingly severe continental convection would be permitted in warmer climates, should other environmental parameters be unchanged. This result could also be extended to seasonal variability of severe convection, with wetter winter or spring seasons possibly yielding moister soils that would be conducive to higher peak CAPE conditions. Future studies could seek to identify such correlations in the observational record.

Care should be taken not to overgeneralize these results. No determinations are made about changes in deep layer shear or convective initiation, both of which are important for supporting severe convection over land. However, this model does provide a theoretically based constraint on the magnitude of CAPE that can arise through diabatic heating in typical continental severe storm environments.

Chapter 5

Conclusions

The overarching goal of this thesis is to contribute to the theoretical scientific understanding of the climatology of severe convection over land. Its components accomplish this task by providing key results on the thermodynamic preconditioning of the atmosphere in continental convective environments. A new paradigm for the buildup of CAPE in advance of severe weather events is identified, and an idealized model is used to demonstrate its viability in a generalized framework. This information is used as the basis of a new theory for the scaling of transient extreme peak CAPE in continental severe environments as a function of known climatological properties of the Earth. The results of these works represent a contribution to the scientific knowledge base in severe weather and climate, but there remains a vast amount of further progress that can be made with related future research.

5.1 Key findings

First, in Chapter 2, a budget of the parcel-following time tendency of CAPE is computed for 8 case studies of severe weather outbreaks in the United States using re-analysis data. In this analysis, it is determined that the primary physical process by which CAPE is generated in advance of such events is the flux of entropy from the land surface into the adjacent boundary layer, in response to diurnal heating. This result is contrary to the established hypothesis that CAPE is built up by way of

differential advection of separate air masses that are already preconditioned: Instead of an existing inhibitive cap layer and low-entropy continental air mass aloft being undercut by high-entropy air advected northward at low levels from the Gulf of Mexico, we find that low-level entropy is actually generated in situ by surface fluxes of heat and moisture. Furthermore, the time scale of CAPE buildup is such that the relevant physical processes tend to occur while the parcels in which high CAPE is achieved are already over land, on the same day that the peak is achieved. In addition to challenging the established paradigm for thermodynamic preconditioning of the atmosphere for severe local storms over North America, this result also implies that properties of the land surface may play an important role in determining where and when transient instances of extreme CAPE are climatologically supported.

Next, in Chapter 3, the result of Chapter 2 is tested in an idealized numerical framework. The numerical model demonstrates that transient extreme peak values can be achieved in a two-dimensional setting in which differential advection is negligible. Instead, a zonal discontinuity in the amount of moisture in the land surface available for evaporation is sufficient to create a capping inversion and allow in-situ generation of low level entropy when a background shear flow is imposed, and the dry land region is upstream of the moist land region. The configuration tested is analogous to a simplified version of the North American continent, where the hot, dry desert region is zonally upstream of the moister soils of the Plains, Midwest, and Southeastern United States. However, since no actual geographic features are included in the idealized model, the results are generalizable to any continent on Earth in which a gradient in surface moisture lends itself to the climatological placement of a capping layer above a moist land surface. The CAPE tendency budget is again used to determine that increases in boundary layer entropy, as driven by diabatic surface heating, are the primary contributor to transient CAPE buildup in such situations.

Finally, a theoretical model of CAPE buildup via boundary layer diabatic heating is developed in Chapter 4. It is determined that for this mechanism, the time-transient peak in CAPE theoretically scales according to the Clausius-Clapeyron relation that determines the saturation limit of water vapor in air as a function of temperature.

Specifically, peak CAPE has a roughly exponential relationship with the temperature of the free tropospheric inversion in this idealized single-column model. However, this model also predicts that CAPE peaks of greater magnitude take more time to be achieved. Therefore, warmer environments should cause CAPE peaks to occur later in the afternoon. Eventually, the peak of CAPE is restricted by the end of the diurnal heating cycle, and the relationship between peak CAPE and temperature deviates from Clausius-Clapeyron scaling. Crucially, this model also predicts that for a given choice of background temperature, the magnitude of peak CAPE increases with increased evaporation due to an increase in available moisture in the land surface, or due to increased surface wind speeds.

5.2 Future work

As the work that comprises this thesis takes place in a newly burgeoning subfield at the intersection of severe storms and climate, its results open doors to a plethora of possible future research paths.

First, the CAPE tendency budget case study methodology established in Chapter 2 using the North American Regional Reanalysis could be extended to other regions of the globe. While North America is home to some of Earth's most severe convection, similarly intense storms are also observed in other parts of the world, including central Argentina, west central Africa, and the coast of the Indian subcontinent (Zipser et al. 2006). While the results of Chapter 3 demonstrate that the boundary layer diabatic heating mechanisms is sufficient to sustain climatologically frequent occurrences of high CAPE over continents, it would be instructive to determine definitively if this is indeed the principal mechanism at play in Earth's other severe storm environments, especially those closer to the Equator. This could be accomplished using global reanalyses (although this may prove challenging for those reanalyses whose resolution is coarser than that of NARR), operational forecasting models, or even field campaigns.

Another direction in which the research could be taken is the study of convective

inhibition. While this thesis provides important insights about the climatology of CAPE in metastable atmospheric profiles, little determination has been made with regard to CIN. A logical extension of the CAPE tendency budget work in Chapters 2 and 3 would be to derive a budget for the time tendency of CIN, and apply it to reanalysis or to an idealized model to test the hypothesis that the CIN in continental deep convective environments is derived from differential advection of a capping inversion layer. It will also be important to characterize the theoretical dependence of continental CIN on climatological environmental factors, in order to make any determination about changes to the overall climatology of severe local storms. For instance, if CIN increases concurrently with CAPE, one might expect to see fewer, but more intense storms; if CIN remains constant, there could be an increase in both frequency and severity of continental deep convection.

One interesting possible research path with respect to frequency and severity of storms would be to attempt to calculate a metric for the integrated amount of CAPE converted to kinetic energy by continental deep convection on an annual basis, and look for trends in that metric over time in data, models, or theory.

The theoretical scaling for CAPE as a function of temperature, surface moisture, and surface wind speed derived in Chapter 4 could be tested by looking for correlations between those quantities and continental peak CAPE levels in observations, reanalysis or models. One challenge that would be presented when attempting to examine past data for such correlations is that observations of soil moisture are not particularly plentiful in the historical record. However, tools such as the Oklahoma Mesonet (McPherson et al. 2007) and the NASA Soil Moisture Active Passive (Entekhabi et al. 2010) satellite instrument could provide a partial record of soil moisture conditions for certain subsets of the geographical-temporal parameter space. Otherwise, records of seasonal precipitation could be used as a proxy to get a rough estimate of the amount of moisture contained in the soil of a certain region for a given season.

Furthermore, the peak CAPE scaling could be applied to climate projections of the aforementioned environmental variables to make predictions about potential changes in continental peak CAPE in different climate change scenarios. In that

sense, the results of this research could be used in conjunction with global or regional climate models as a sort of post-processing tool to make inferences about convective environments or convective storms on scales that are too fine to be resolved by such models. The scaling could also be applied in an operational context to underpin seasonal severe storm forecasts on an interannual basis. •

Appendix A

Equilibrium mean dynamic state of multi-column model in constant radiation experiment

Figure A-1 shows cross sections of mean equilibrium quantities from the nondiurnal run. Figure A-1a shows the time-averaged vertical velocity field across the domain, while Figure A-1b shows the convective updraft mass flux as calculated by the model's parameterized convection scheme. Figure A-1c shows the perturbation temperature field. This field is calculated by subtracting the mean domain temperature at each level from the full temperature field. Finally, Figure A-1d shows a cross section of time-averaged relative humidity for the statistical equilibrium state.

As shown in Figure A-1a, a local maximum of large-scale rising motion occurs on the dry side of the dry land-wet land boundary. This maximum of rising motion may be a result of surface zonal wind convergence as air flows from the cooler ocean and wet land regions onto the dry land region. This feature is advected toward the easternmost boundary of the dry land region by the background zonal wind. Likewise, a local maximum of large-scale subsidence occurs on the ocean side of the ocean-dry land boundary. At higher levels (above 600 hPa), large-scale ascent is observed over the wet land columns, while large-scale subsidence is observed over the dry land.

Figure A-1b shows deep convection occurring across the entirety of the domain,

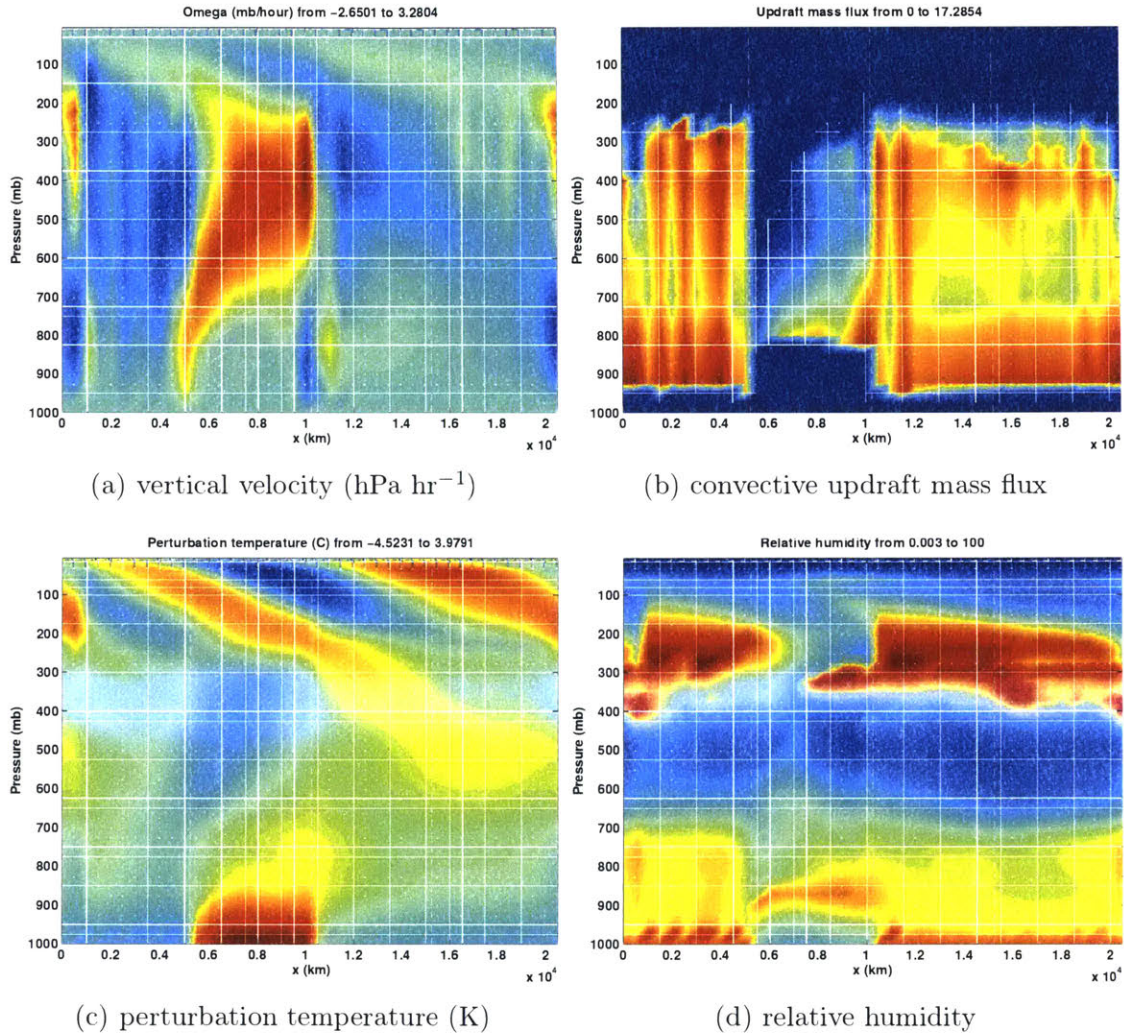


Figure A-1: Mean equilibrium cross sections of vertical velocity (a), parameterized convective updraft mass flux (b), temperature perturbation from the zonal mean (c), and relative humidity (d) for the case of diurnally averaged radiation. The dotted lines indicate the boundaries between the ocean, 'dry' land, and 'wet' land regions.

with the exception of the dry land columns. While the LFC is below 900 hPa for the rest of the domain, it appears to be just below 800 hPa in the dry land columns. Thus, the subcloud layer is much deeper over the surface with low evaporative fraction than over those with high EF. Furthermore, the vertical extent of convection is much lower in these columns, while convection nears the tropopause in the rest of the domain.

Figures A-1c and A-1d show that the subcloud layer of the dry land columns is anomalously warm and dry. Figure A-1c shows a large warm anomaly in the dry land columns between the surface and LFC, while Figure A-1d shows a region of relatively dry air in the same area. Contrastingly, in the remaining columns, the mean relative humidity is close to 1 near the surface. Additionally, while the greatest warm anomaly is confined to the subcloud layer of the dry land columns, as shown in Figure A-1c, a larger area of smaller warm anomaly extends vertically and to the east of that area, overlapping with the leftmost wet land columns below approximately 700 hPa. This eastward extent of the region of anomalous warmth is likely due to the zonal background shear flow, which allows warm air to be advected to the east above the surface level. The presence of anomalously warm air above the surface layer in the westernmost wet land column provides the possibility of a temperature inversion that could create a potential barrier to convection and allow large transient values of CAPE to build.

Appendix B

Derivation of long-time moist static energy limit in asymptotic regime

We begin with the nondimensional equation governing the flux of moist static energy from the surface into the boundary layer (4.29):

$$(1-\alpha)(\delta + \delta_s) + \alpha(\mu_s - \mu) - 1 = \Phi. \quad (\text{B.1})$$

In the limit of infinite time ($\tau \rightarrow \infty$), the dry static energy deficit, δ , goes to 0, while the surface dry static energy, δ_s , goes to 1 (as $T_{\text{sfc}} \rightarrow T_0$). Therefore, applying the infinite time limit to this equation yields

$$(1-\alpha) + \alpha \lim_{\tau \rightarrow \infty} (\mu_s - \mu) - 1 = \Phi. \quad (\text{B.2})$$

Rearranging and redimensionalizing gives

$$\lim_{t \rightarrow \infty} (M - D_0 - c_p T_{\text{sfc}} - L_v q^*(T_{\text{sfc}})) = -\frac{F_{\text{rad}}}{\alpha \rho C_T v_{\text{sfc}}} - D_0. \quad (\text{B.3})$$

We now substitute $\lim_{t \rightarrow \infty} T_{\text{sfc}} = T_0$ and $c_p T_0 = D_0$ to yield

$$\lim_{t \rightarrow \infty} M - D_0 = L_v q^*(T_0) - \frac{F_{\text{rad}}}{\alpha \rho C_T v_{\text{sfc}}}. \quad (\text{B.4})$$

Appendix C

Derivation of regime boundaries

The boundaries between the peak, intermediate, and asymptotic regimes are derived in terms of the long-time limits of model variables.

In the intermediate and asymptotic regimes, the long-time limit of moist static energy M is given by (4.33), as derived in Appendix A:

$$\lim_{t \rightarrow \infty} M - D_0 = L_v q^*(T_0) - \frac{F_{\text{rad}}}{\alpha \rho C_T v_{\text{sfc}}}. \quad (\text{C.1})$$

When the long-time limit of the moist static energy surplus is positive ($\lim_{t \rightarrow \infty} M - D_0 > 0$), the system is in either the intermediate or asymptotic regime. Therefore, when the limit is negative ($\lim_{t \rightarrow \infty} M - D_0 < 0$), the system must be in the peak regime. Substituting this inequality into the above equation and rearranging yields the condition

$$q^*(T_0) < \frac{F_{\text{rad}}}{\alpha \rho C_T v_{\text{sfc}} L_v} \quad (\text{C.2})$$

for the peak regime.

To distinguish between the intermediate and fully asymptotic regimes, we start from the nondimensional equation for the time rate of change of the moist static

energy surplus (4.23):

$$\frac{d\mu}{d\tau} = \frac{\Phi}{\eta} - \frac{\mu A_R}{\eta \delta} (\delta_s + \delta - 1). \quad (\text{C.3})$$

In the fully asymptotic regime, the moist static energy surplus, μ , increases asymptotically toward its long-time limit for all time, and does not exhibit a transient peak. Therefore, the time derivative of μ is positive-definite:

$$\frac{d\mu}{d\tau} = \frac{\Phi}{\eta} - \frac{\mu A_R}{\eta \delta} (\delta_s + \delta - 1) > 0. \quad (\text{C.4})$$

Simplifying and rearranging yields

$$\Phi > \mu A_R \left(\frac{\delta_s + \delta - 1}{\delta} \right). \quad (\text{C.5})$$

We now take the long-time limit of this inequality:

$$\Phi > \left[\lim_{\tau \rightarrow \infty} \mu \right] A_R \lim_{\tau \rightarrow \infty} \left(\frac{\delta_s + \delta - 1}{\delta} \right). \quad (\text{C.6})$$

Since $\lim_{\tau \rightarrow \infty} \delta_s = 1$, it can be shown that

$$\lim_{\tau \rightarrow \infty} \left(\frac{\delta_s + \delta - 1}{\delta} \right) = 1. \quad (\text{C.7})$$

Substituting this into (C.6) and redimensionalizing yields

$$\frac{F_{\text{rad}}}{\rho C_T v_{\text{sfc}}} > A_R \lim_{t \rightarrow \infty} M - D_0. \quad (\text{C.8})$$

We now substitute the long-time limit of moist static energy ($\lim_{t \rightarrow \infty} M$) from (4.33) into the above inequality, resulting in the condition

$$q^*(T_0) > \left(\frac{1}{A_R} + \frac{1}{\alpha} \right) \frac{F_{\text{rad}}}{\rho C_T v_{\text{sfc}} L_v} \quad (\text{C.9})$$

for the asymptotic regime.

The intermediate regime exists for the range of $q^*(T_0)$ between the peak and asymptotic regimes:

$$\frac{F_{\text{rad}}}{\alpha \rho C_T v_{\text{sf}} L_v} < q^*(T_0) < \left(\frac{1}{A_R} + \frac{1}{\alpha} \right) \frac{F_{\text{rad}}}{\rho C_T v_{\text{sf}} L_v}. \quad (\text{C.10})$$

Bibliography

- Agard, V., and K. Emanuel, 2017: Clausius-clapeyron scaling of peak CAPE in continental convective storm environments. *J. Atmos. Sci.*
- Banacos, P. C., and M. L. Ekster, 2010: The association of the elevated mixed layer with significant severe weather events in the northeastern United States. *Wea. Forecasting*, **25** (4), 1082–1102.
- Betts, A. K., 2000: Idealized model for equilibrium boundary layer over land. *J. Hydrometeor.*, **1** (6), 507–523.
- Bluestein, H. B., 2007: Advances in applications of the physics of fluids to severe weather systems. *Reports on Progress in Physics*, **70** (8), 1259–1323, doi:10.1088/0034-4885/70/8/R01.
- Bluestein, H. B., 2013: *Severe Convective Storms and Tornadoes*. Springer Berlin Heidelberg.
- Bony, S., and K. A. Emanuel, 2001: A parameterization of the cloudiness associated with cumulus convection; evaluation using TOGA COARE data. *J. Atmos. Sci.*, **58**, 3158–3183.
- Botzen, W. J. W., L. M. Bouwer, and J. C. J. M. van den Bergh, 2010: Climate change and hailstorm damage: Empirical evidence and implications for agriculture and insurance. *Resource and Energy Economics*, **32**, 341–362.
- Bouwer, L. M., 2011: Have disaster losses increased due to anthropogenic climate change? *Bull. Amer. Meteor. Soc.*, **92** (1).
- Brooks, H. E., 2009: Proximity soundings for severe convection for europe and the united states from reanalysis data. *Atmos. Res.*, **93** (1), 546–553.
- Brooks, H. E., 2013: Severe thunderstorms and climate change. *Atmos. Res.*, **123**, 129–138.
- Brooks, H. E., C. A. Doswell III, and J. Cooper, 1994: On the environments of tornadic and nontornadic mesocyclones. *Wea. Forecasting*, **9** (4), 606–618.
- Brooks, H. E., C. A. Doswell III, and M. P. Kay, 2003a: Climatological estimates of local daily tornado probability for the united states. *Wea. Forecasting*, **18** (4), 626–640.

- Brooks, H. E., J. W. Lee, and J. P. Craven, 2003b: The spatial distribution of severe thunderstorm and tornado environments from global reanalysis data. *Atmos. Res.*, **67**, 73–94, doi:10.1016/S0169-8095(03)00045-0.
- Cao, Z., 2008: Severe hail frequency over Ontario, Canada: Recent trend and variability. *Geophys. Res. Lett.*, **35** (14), L14 803.
- Carlson, T., and F. Ludlam, 1968: Conditions for the occurrence of severe local storms. *Tellus*, **20** (2), 203–226.
- Changnon, S. A., 2001: Damaging thunderstorm activity in the United States. *Bull. Amer. Meteor. Soc.*, **82** (4), 597–608.
- Changnon, S. A., 2009: Increasing major hail losses in the US. *Climatic Change*, **96** (1-2), 161–166.
- Cook, A. R., and J. Schaefer, 2008: The relation of El Nino-Southern Oscillation (ENSO) to winter tornado outbreaks. *Mon. Wea. Rev.*, **136** (8), 3121–3137.
- Del Genio, A. D., M.-S. Yao, and J. Jonas, 2007: Will moist convection be stronger in a warmer climate? *Geophys. Res. Lett.*, **34** (16).
- Dessens, J., 1995: Severe convective weather in the context of a nighttime global warming. *Geophys. Res. Lett.*, **22** (10), 1241–1244.
- Diffenbaugh, N. S., M. Scherer, and R. J. Trapp, 2013: Robust increases in severe thunderstorm environments in response to greenhouse forcing. *Proceedings of the National Academy of Sciences*, **110** (41), 16 361–16 366.
- Donner, L. J., and V. T. Phillips, 2003: Boundary layer control on convective available potential energy: Implications for cumulus parameterization. *J. Geophys. Res.*, **108** (D22), 4701.
- Doswell III, C. A., H. E. Brooks, and M. P. Kay, 2005: Climatological estimates of daily local nontornadic severe thunderstorm probability for the United States. *Wea. Forecasting*, **20** (4), 577–595.
- Doswell III, C. A., H. E. Brooks, and R. A. Maddox, 1996: Flash flood forecasting: An ingredients-based methodology. *Wea. Forecasting*, **11** (4), 560–581.
- Emanuel, K. A., 1994: *Atmospheric Convection*. Oxford University Press, 580 pp.
- Emanuel, K. A., and M. Živković-Rothman, 1999: Development and evaluation of a convection scheme for use in climate models. *J. Atmos. Sci.*, **56**, 1766–1782.
- Entekhabi, D., and Coauthors, 2010: The Soil Moisture Active Passive (SMAP) mission. *Proceedings of the IEEE*, **98** (5), 704–716.
- Gelaro, R., and Coauthors, 2017: The Modern-Era Retrospective Analysis for Research and Applications, Version 2 (MERRA-2). *J. Climate*, **30** (14), 5419–5454.

- Gensini, V. A., and T. L. Mote, 2015: Downscaled estimates of late 21st century severe weather from CCSM3. *Climatic Change*, **129** (1-2), 307–321.
- Grams, J. S., R. L. Thompson, D. V. Snively, J. A. Prentice, G. M. Hodges, and L. J. Reames, 2012: A climatology and comparison of parameters for significant tornado events in the united states. *Wea. Forecasting*, **27** (1), 106–123.
- Grumm, R. H., 2005: Examining severe weather events using reanalysis datasets. *Preprints, 21st Conference on Weather Analysis and Forecasting/17th Conference on Numerical Weather Prediction, Amer. Meteor. Soc.*
- Hoinka, K. P., 1999: Temperature, humidity, and wind at the global tropopause. *Mon. Wea. Rev.*, **127** (10), 2248–2265, doi:10.1175/1520-0493(1999)127<2248:THAWAT>2.0.CO;2.
- Holton, J. R., 2004: *An Introduction to Dynamic Meteorology*. 4th ed., Elsevier, 535 pp.
- Holton, J. R., P. H. Haynes, M. E. McIntyre, A. R. Douglass, R. B. Rood, and L. Pfister, 1995: Stratosphere-troposphere exchange. *Rev. Geophys.*, **33** (4), 403–439, doi:10.1029/95RG02097.
- Johnson, R. H., and B. E. Mapes, 2001: Mesoscale processes and severe convective weather. *Severe Convective Storms*, Springer, 71–122.
- Lanicci, J. M., and T. T. Warner, 1991: A synoptic climatology of the elevated mixed-layer inversion over the southern great plains in spring. Part I: Structure, dynamics, and seasonal evolution. *Wea. Forecasting*, **6** (2), 198–213.
- Lilly, D. K., 1968: Models of cloud-topped mixed layers under a strong inversion. *Quart. J. Roy. Meteor. Soc.*, **94** (401), 292–309, doi:10.1002/qj.49709440106.
- López, L., J. L. Marcos, J. L. Sánchez, A. Castro, and R. Fraile, 2001: CAPE values and hailstorms on northwestern Spain. *Atmos. Res.*, **56** (1), 147–160.
- McPherson, R. A., and Coauthors, 2007: Statewide monitoring of the mesoscale environment: A technical update on the Oklahoma Mesonet. *J. Atmos. Oceanic Technol.*, **24** (3), 301–321.
- Mesinger, F., and Coauthors, 2006: North American Regional Reanalysis. *Bull. Amer. Meteor. Soc.*, **87** (3), 343–360.
- Monin, A., and A. Obukhov, 1954: Basic laws of turbulent mixing in the surface layer of the atmosphere. *Contrib. Geophys. Inst. Acad. Sci. USSR*, **151** (163), e187.
- Morcrette, J.-J., 1991: Radiation and cloud radiative properties in the European Centre for Medium Range Weather Forecasts forecasting system. *J. Geophys. Res.*, **96** (D5), 9121–9132.

- Niall, S., and K. Walsh, 2005: The impact of climate change on hailstorms in south-eastern Australia. *Int. J. Climatol.*, **25** (14), 1933–1952.
- NOAA, NASA, and US Air Force, 1976: U.S. Standard Atmosphere, 1976. Tech. rep., U.S. Government Printing Office, Washington, D.C., 227 pp.
- Parodi, A., and K. Emanuel, 2009: A theory for buoyancy and velocity scales in deep moist convection. *J. Atmos. Sci.*, **66** (11), 3449–3463, doi:10.1175/2009JAS3103.1.
- Pielke, R. A., Sr., 2001: Influence of the spatial distribution of vegetation and soils on the prediction of cumulus convective rainfall. *Rev. Geophys.*, **39** (2), 151–177.
- Rasmussen, E. N., and D. O. Blanchard, 1998: A baseline climatology of sounding-derived supercell and tornado forecast parameters. *Wea. Forecasting*, **13** (4), 1148–1164, doi:10.1175/1520-0434(1998)013<1148:ABCOSD>2.0.CO;2.
- Rennó, N. O., and A. P. Ingersoll, 1996: Natural convection as a heat engine: A theory for CAPE. *J. Atmos. Sci.*, **53** (4), 572–585.
- Riemann-Campe, K., K. Fraedrich, and F. Lunkeit, 2009: Global climatology of Convective Available Potential Energy (CAPE) and Convective Inhibition (CIN) in ERA-40 reanalysis. *Atmos. Res.*, **93**, 534–545.
- Romps, D. M., 2011: Response of tropical precipitation to global warming. *J. Atmos. Sci.*, **68** (1), 123–138, doi:10.1175/2010JAS3542.1.
- Romps, D. M., 2016: Clausius–clapeyron scaling of CAPE from analytical solutions to rce. *Journal of the Atmospheric Sciences*, **73** (9), 3719–3737.
- Romps, D. M., J. T. Seeley, D. Vollaro, and J. Molinari, 2014: Projected increase in lightning strikes in the United States due to global warming. *Science*, **346** (6211), 851–854.
- Rosenzweig, C., F. N. Tubiello, R. Goldberg, E. Mills, and J. Bloomfield, 2002: Increased crop damage in the us from excess precipitation under climate change. *Global Environmental Change*, **12** (3), 197–202.
- Schär, C., D. Lüthi, U. Beyerle, and E. Heise, 1999: The soil-precipitation feedback: A process study with a regional climate model. *J. Climate*, **12**, 722–741.
- Schultz, D. M., Y. P. Richardson, P. M. Markowski, and C. A. Doswell III, 2014: Tornadoes in the central United States and the “Clash of Air Masses”. *Bull. Amer. Meteor. Soc.*, **95** (11), 1704–1712.
- Seeley, J. T., and D. M. Romps, 2015: The effect of global warming on severe thunderstorms in the United States. *J. Climate*, **28** (6), 2443–2458.
- Shaw, B. L., R. A. Pielke, and C. L. Ziegler, 1997: A three-dimensional numerical simulation of a Great Plains dryline. *Mon. Wea. Rev.*, **125**, 1489–1506.

- Singh, M. S., and P. A. O’Gorman, 2013: Influence of entrainment on the thermal stratification in simulations of radiative-convective equilibrium. *Geophys. Res. Lett.*, **40** (16), 4398–4403, doi:10.1002/grl.50796.
- Sobel, A. H., and S. J. Camargo, 2011: Projected future seasonal changes in tropical summer climate. *J. Climate*, **24** (2), 473–487, doi:10.1175/2010JCLI3748.1.
- Solomon, A., J. Lu, and J. Kinter III, 2013: Tornado risks will shift with a changing climate. *Nature Comm.*
- Storm Prediction Center, 2011: Annual severe weather report summary, http://www.spc.noaa.gov/climo/online/monthly/2011_annual_summary.html.
- Taylor, C. M., and R. J. Ellis, 2006: Satellite detection of soil moisture impacts on convection at the mesoscale. *Geophys. Res. Lett.*, **33** (3).
- Tippett, M. K., J. T. Allen, V. A. Gensini, and H. E. Brooks, 2015: Climate and hazardous convective weather. *Current Climate Change Reports*, **1** (2), 60–73.
- Trapp, R. J., N. S. Diffenbaugh, H. E. Brooks, M. E. Baldwin, E. D. Robinson, and J. S. Pal, 2007a: Changes in severe thunderstorm environment frequency during the 21st century caused by anthropogenically enhanced global radiative forcing. *Proceedings of the National Academy of Sciences*, **104** (50), 19 719–19 723.
- Trapp, R. J., B. A. Halvorson, and N. S. Diffenbaugh, 2007b: Telescoping, multi-model approaches to evaluate extreme convective weather under future climates. *J. Geophys. Res.: Atmospheres (1984–2012)*, **112** (D20).
- Trapp, R. J., and K. A. Hoogewind, 2016: The realization of extreme tornadic storm events under future anthropogenic climate change. *J. Climate*, **29** (14), 5251–5265.
- Weisman, M. L., and J. B. Klemp, 1982: The dependence of numerically simulated convective storms on vertical wind shear and buoyancy. *Mon. Wea. Rev.*, **110** (6), 504–520.
- Williams, E., and N. Rennó, 1993: An analysis of the conditional instability of the tropical atmosphere. *Mon. Wea. Rev.*, **121**, 21–21.
- Williams, E. R., S. Geotis, N. Renno, S. Rutledge, E. Rasmussen, and T. Rickenbach, 1992: A radar and electrical study of tropical hot towers. *J. Atmos. Sci.*, **49** (15), 1386–1395.
- Ye, B., A. D. Del Genio, and K. K.-W. Lo, 1998: CAPE variations in the current climate and in a climate change. *J. Climate*, **11**, 1997–2015.
- Zipser, E. J., D. J. Cecil, C. Liu, S. W. Nesbitt, and D. P. Yorty, 2006: Where are the most intense thunderstorms on earth? *Bull. Amer. Meteor. Soc.*, **87** (8), 1057–1071, doi:10.1175/BAMS-87-8-1057.